Bose-Einstein Condensation of Optically Trapped Cesium

Dissertation

zur Erlangung des Doktorgrades an der
naturwissenschaftlichen Fakultät
der Leopold-Franzens-Universität Innsbruck

vorgelegt von

Tino Weber

durchgeführt am Institut für Experimentalphysik
unter der Leitung von
Univ.-Prof. Dr. Rudolf Grimm

September 2003

Zusammenfassung

Im Rahmen dieser Arbeit wurde erstmals die Bose-Einstein-Kondensation (BEC) von ^{133}Cs erreicht. Durch evaporative Kühlung in einer optischen Falle wird ein Kondensat im absoluten Grundzustand ($F = 3, m_F = 3$) erzeugt.

Cäsium zeigt einzigartige Streueigenschaften, die die Erzeugung eines Bose-Einstein-Kondensates lange verhindert haben. In zahlreichen Experimenten weltweit wurde viel Wissen über diese Eigenschaften gesammelt. Im Entwurf des hier vorgestellten experimentellen Aufbaus wurden diese vorhandenen Ergebnisse genutzt, um die speziellen Probleme im Umgang mit Cäsium zu vermeiden und seine besonderen Eigenschaften zur Erreichung des BEC einzusetzen.

Zwei CO_2-Laser mit einer Leistung von je 100 W formen eine schwache quasi-elektrostatische optische Dipolfalle, die in Verbindung mit einem magnetischen Levitationsfeld ausschließlich den absoluten inneren Grundzustand der Cs-Atome fängt, wodurch eine vollständige Spinpolarisation sichergestellt ist. Die Unterdrückung inelastischer Zweikörper-Verluste in diesem System wurde in ersten Experimenten genutzt, um detaillierte Messungen zu Dreikörper-Rekombinationsraten bei großen Streulängen durchzuführen [Web03b]. Die Möglichkeit, durch ein magnetisches Feld die Streulänge a einzustellen, erlaubte erstmals die experimentelle Bestätigung der theoretisch vorhergesagten Skalierung der Rekombinationsrate mit a^4. Der in der Theorie enthaltene Skalierungsfaktor wurde zu $n_l C = 225$ bestimmt. Dieser Wert stimmt im Rahmen der Fehlergrenzen mit den Vorhersagen überein.

Ein entscheidendes Ergebnis aus den Messungen zur Dreikörper-Rekombination ist die Beobachtung von Rekombinationsheizen. In einer Erweiterung des experimentellen Aufbaus wurde eine optische Mikrofalle implementiert, in der die Auswirkungen des Rekombinationsheizens vermieden werden. Gleichzeitig erlaubt die Mikrofalle effiziente evaporative Kühlung durch Absenken des optischen Potentials. Nach Optimierung des Evaporationspfades durch Einstellung einer geeigneten Streulänge wurde bei einer kritischen Temperatur von 50 nK der Phasenübergang zum BEC mit bis zu 16000 Atomen im Kondensat beobachtet [Web03a].

In ersten Experimenten zeigt sich die starke Abhängigkeit der inneren Energie des Kondensates vom magnetischen Feld. Durch Einstellung verschiedener Streulängen werden implodierende, explodierende und nicht wechselwirkende “eingefrorene” Kondensate erzeugt. In Expansionsmessungen wurde eine mittlere kinetische Energie von bis hinunter zu $\frac{1}{2}k_B \cdot (220 \pm 100)$ pK gemessen.

Abstract

This thesis reports on the realization of the first Bose-Einstein condensate (BEC) of ^{133}Cs. Condensation is achieved in the lowest internal state ($F = 3, m_F = 3$) by evaporative cooling in an optical trap.

Cesium has unique scattering properties, which have prevented Bose-Einstein condensation for many years. Much knowledge has been collected on these properties in many experiments world-wide. The experimental setup constructed during this thesis was designed with that knowledge in mind to avoid the peculiar pitfalls cesium has to offer and to use its special properties on the path towards BEC.

A shallow quasi-electrostatic optical dipole trap formed by two 100-W CO_2 lasers in combination with a magnetic levitation field allows for selective trapping of the absolute internal ground state, ensuring perfect spin polarization. In first experiments, the complete suppression of inelastic two-body losses in this setup was used to perform detailed measurements of three-body recombination effects at large scattering length a [Web03b]. The magnetic tunability of a via Feshbach resonances was employed to experimentally confirm for the first time the theoretically predicted a^4 scaling of the three-body recombination rate coefficient and to determine the value of a universal scaling factor $n_l C$ included in the theory. The value of $n_l C = 225$ agrees with the predictions within its error limits.

A further result of the three-body recombination measurements, strong evidence for recombination heating, has been of crucial importance for identifying a suitable path towards condensation. An extension of the setup, an optical microtrap (“dimple”), avoids the detrimental effects of recombination heating and allows for efficient evaporative cooling by lowering the optical potential. Using the tunable scattering length to optimize the evaporation path, Bose-Einstein condensation was achieved at a critical temperature of 50 nK, with a maximum of 16000 atoms in the condensate phase [Web03a].

First experiments with the BEC demonstrate the strong dependence of the condensate mean-field energy on the magnetic field. By briefly switching to different scattering lengths just before releasing the sample from the trap, imploding, exploding, and non-interacting “frozen” condensates are realized. The lowest kinetic energy measured in the expansion of a condensate is $\frac{1}{2} k_B \cdot (220 \pm 100)$ pK.

Contents

Chapter 1

Introduction

Almost 80 years ago, the concept of Bose-Einstein statistics was derived for a certain class of particles[1] [Bos24, Ein25]. This theoretical frame implies phenomena that are far from self-evident, and, as Einstein wrote, "…express indirectly a certain hypothesis on a mutual influence of the molecules which for the time being is of a quite mysterious nature" (in: [Cor02]).

One of these phenomena is the increased probability for entering a quantum state which is already occupied; the most prominent application of this phenomenon is the laser. Another effect is already noted in Einstein's 1925 paper: "I maintain that, in this case, a number of molecules steadily growing with increasing density goes over in the first quantum state (which has zero kinetic energy) while the remaining molecules separate themselves according to the parameter value $A = 1$ […] A separation is effected; one part condenses, the rest remains a 'saturated ideal gas.' " (in: [Cor99]).

This effect, soon called Bose-Einstein condensation (BEC), was derived for a low-temperature ideal gas, a system not readily available for studies at that time. It is therefore not amazing that the idea was generally not taken too seriously, and early notions of linking superfluidity in liquid helium to BEC did not win much recognition. Today we know that both superfluidity and superconductivity are indeed closely connected to BEC, however these are special, strongly interacting systems in which the condensation process is not readily observable.

It was already noted in 1959 [Hec59] that spin polarized hydrogen might be a very good candidate for a more weakly interacting BEC, remaining in a metastable gaseous state down to zero temperature. This thought led to many low-temperature experiments starting in the late 1970s using refrigeration techniques with liquid helium dilution refrigerators to cool the sample. However, the experimental difficulties were great, and this line of research was overtaken by the field of laser cooling of heavier alkali atoms, which grew strongly in the 1980s and, finally, in 1995 led to the first realization of BEC with ^{87}Rb and ^{23}Na [And95, Dav95]. Not much later, condensation

---

[1] The first publication by Bose specifically refers to photon statistics [Bos24], Einstein extended the concept to systems with conserved particle number [Ein25]. Today we know the statistics applies to all particles with integer spin and call these bosons.

of the original first candidate for BEC in dilute ultracold atomic gases, hydrogen, was achieved [Fri98].

This creation of a dilute, experimentally accessible, weakly interacting macroscopic matter wave led to an explosion of research activity. A multitude of experiments employed the unique possibilities in these systems to study effects that previously had only been predicted theoretically or that elude observation in their "natural surroundings", like in "classical" condensed-matter physics. A Bose-Einstein condensate can serve as excellent model system for quantum effects, and BECs have helped to understand many phenomena of the quantum world. In the course of this world-wide research effort, only a few more atomic species, namely ^{7}Li [Bra95], ^{85}Rb [Cor00], ^{41}K [Mod01], ^{4}He [Rob01], and, lately, ^{174}Yb [Tak03], have been Bose condensed.

In the frame of this thesis, we have added a new and peculiar species to the "BEC zoo", cesium (^{133}Cs). This atom is of particular interest in physics. It features a large hyperfine splitting in the ground state, and the corresponding microwave transition has been the primary frequency standard since 1967. It is the heaviest stable alkali atom; indeed, cesium has more isotopes (32) than any other element, with mass numbers ranging from 114 to 145, and ^{133}Cs is the only stable one among them [Los03]. Its single valence electron is loosely bound, giving rise to a rich spectrum of electron-nucleus and atom-atom interactions. Of all elements, cesium is the most electropositive[2], has the largest polarizability, and features the strongest van der Waals interaction strength [Chi01a].

These unique properties make cesium relevant for many applications in fundamental metrology, like measurements of parity violation [Woo97], gravity [Sna98], the electron electric dipole moment [Chi01b], or variations of fundamental constants [Mar03a]. A Bose-Einstein condensate of cesium will constitute an ideal sample for future precision measurements.

Cesium has been studied extremely well over the years, and especially in the cold atom community has been found to show unexpected behavior in many experiments. Much knowledge on otherwise subtle effects has been gained in trying to understand these peculiarities. The following chapter will introduce this special atom and its role and history in the physics of ultracold quantum gases.

---

[2] Cesium reacts explosively with cold water, and reacts with ice at temperatures above -116 °C. Cesium hydroxide, the strongest base known, attacks glass [Los03].

Chapter 2

The cesium atom

From the beginning of research in dilute atomic Bose-Einstein condensation with alkali atoms, attempts have been made at condensation of ^{133}Cs. Its transition properties and high-energy scattering properties are well known, since it is the frequency standard, and many spectroscopy and laser cooling techniques have been developed in cesium.

However, the standard path towards BEC, capturing the atoms in a magneto-optical trap and then evaporatively cooling them in a magnetic trap [Ket99, Cor99], has up to now not been successful with this element. I will try to explain what makes it so difficult and at the same time interesting.

2.1 An alkali atom

All experiments described in this work operate on ^{133}Cs, the only stable isotope of cesium. The combination of its nuclear spin 7/2 with the spin 1/2 of the single valence electron makes it a boson. The energetically lowest electronic states of this heaviest stable alkali atom are shown in Fig. 2.1.

The transition from the $6^2S_{1/2}$ ground state to the $6^2P_{3/2}$ excited state (the D_2 line) is the closed transition employed in ^{133}Cs laser cooling. The natural line width of this transition is $\Gamma_2 = 2\pi \cdot 5.22$ MHz. The line width of the $6^2S_{1/2} \rightarrow 6^2P_{1/2}$ (D_1) transition is $\Gamma_1 = 2\pi \cdot 4.56$ MHz. The hyperfine splitting of the ground state is 9.2 GHz, the SI definition of the second is based on this microwave transition. The hyperfine splitting of the $6^2P_{3/2}$ excited state is much smaller, at 150-250 MHz.

Due to its large mass of 133 amu ($2.207 \cdot 10^{-25}$ kg), the energy imparted by the recoil from scattering of a single photon, expressed in temperature units as *recoil temperature*, is only 200 nK. This makes cesium very well suited for laser cooling applications. An excellent overview of all properties of cesium relevant in this context is given in [Ste02].

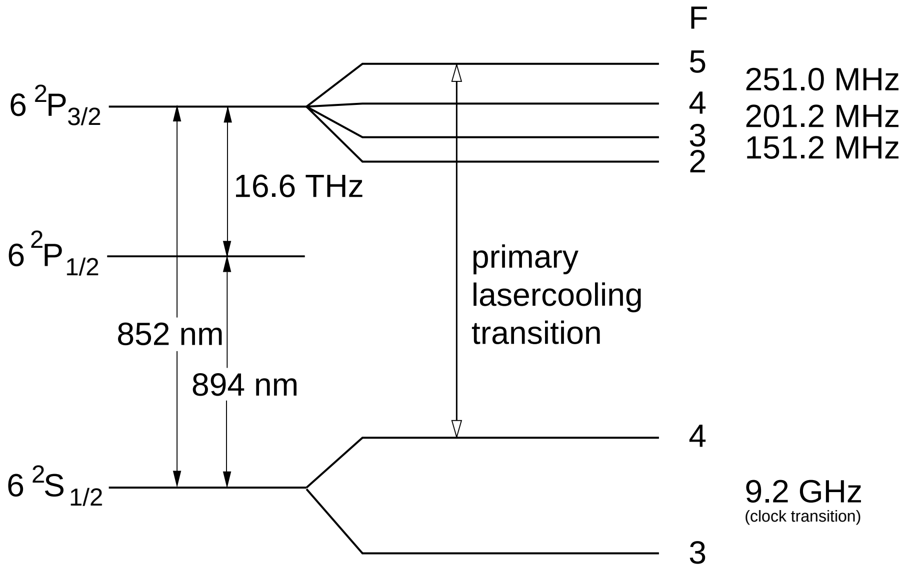

Figure 2.1: ^{133}Cs D lines

2.2 Inelastic scattering: Why cesium wasn't first

Due to its mass and its large hyperfine splitting, cesium is well suited to optical cooling techniques [Kas95, Boi96]. Since the wavelength band used in early optical telecommunications was centered at 850 nm[1], high-power semiconductor diode lasers for addressing the 852 nm D_2 line were readily available, making it relatively easy to set up efficient and robust laser cooling experiments. It is therefore no surprise that cesium was initially considered to be a prime candidate for Bose-Einstein condensation [Mon93].

In general, to achieve BEC atoms are captured and pre-cooled in a magneto-optical trap [Raa87] and then for evaporative cooling transferred into a (nearly) conservative trapping potential [Ket99]. Atom traps can be made conservative to a very high degree, causing almost no heating to a trapped sample. However, through collisions atoms can change their internal degrees of freedom. These inelastic collisions can be endothermic or exothermic, respectively converting kinetic energy into potential energy or vice versa. Endothermic collisions are usually excluded due to the low kinetic energy available at μK temperatures, however exothermic collisions release energy into the sample and cause heating and/or loss from the trap.

Inelastic collisions are characterized by the number of atoms involved in such a process. Because the density dependence increases with higher atom number, usually only two-body and three-body losses are considered. Two-body losses are dominant when they cannot be suppressed through careful choice of the internal state of the trapped atoms, while three-body losses in most cases only play a role at high density.

---

[1] Modern telecom applications focus on longer wavelengths around 1300 nm and 1550 nm.

Early experiments on cesium in magnetic traps focused on samples polarized in the upper hyperfine ground state $F = 4$, magnetic sublevel $m_F = 4$. In this doubly polarized state (*stretched* state, both nuclear and electronic spin are aligned with the applied magnetic field), spin-exchange collisions, which constitute the main inelastic two-body loss process, are forbidden. The next strongest contribution to inelastic collisions was then thought to be the much weaker direct magnetic dipolar interaction between the spins of the unpaired electrons of two atoms. However, the spin relaxation rates were measured to be three orders of magnitude higher than expected [Söd98, Arl98]. It was later understood that this is caused by a contribution to the the dipolar interaction from the second-order spin-orbit interaction (also called indirect spin-spin coupling) [Leo98]. This contribution can be very high for heavy atoms due to relativistic effects. Actually, in ^{87}Rb, the first atomic species to be condensed [And95], achieving BEC is greatly simplified because the terms for the direct and indirect contributions to the dipolar interaction partly cancel, giving very low relaxation rates [Mie96]. In cesium, however, the terms also have opposite signs but the second-order contribution is much larger, completely dominating the interaction [Mie96, Leo98]. For some more details on dipolar interactions see also [Tie93].

The next step in magnetic trapping experiments was to move to the $F = 3, m_F = -3$ lower hyperfine state. This avoids hyperfine-changing interactions, as these are now endothermic. The effect of dipolar relaxation could be somewhat suppressed by operating at very low magnetic bias fields around 1 G [GO98a]. However, the inelastic losses where still too high, and both the experiments in Paris [GO98b] and in Oxford [Hop00] did not reach quantum degeneracy. The maximum phase-space density reached in both experiments was a factor of about one hundred away from condensation.

Solving the problem of the strong inelastic two-body losses requires using the absolute ground state of cesium, $F = 3, m_F = 3$. In this state, all inelastic two-body processes are endothermic and are thus fully suppressed at sufficiently low temperature. The $F = 3, m_F = 3$ state cannot be captured in a magnetic trap, as it is a high-field seeker and would require a local maximum of the magnetic field, which is forbidden [Win84]. Therefore, several experiments turned to using optical dipole forces for trapping, which are independent of the magnetic substate. Experiments in Paris [Per98], Stanford [Vul99], Berkeley [Han00], and in our group [Ham02a] explored this path towards high phase-space densities of ^{133}Cs. However, optical traps by themselves do not allow for "cutting" into the potential for evaporative cooling, but can only effect evaporation by lowering the total potential depth. This weakens the confinement of the trapped sample und thus renders evaporation less effective. The Berkeley experiment, using a similar setup to the one developed in this thesis, successfully employed radio-frequency evaporation in a magnetically levitated optical trap [Han01] to reach a phase-space density within a factor of two from BEC, but was eventually limited by three-body recombination [Wei02][2].

---

[2] Three-body recombination in cesium will be treated extensively in Ch. 7.

2.3 Elastic scattering and more cesium specialties

In contrast to inelastic processes, elastic collisions, which only redistribute kinetic energy but leave the internal state of the involved particles unchanged, are necessary for evaporative cooling to ensure thermalization in the ensemble. The prospects for evaporative cooling in a certain setup are therefore often characterized by the ratio between those two types of collisions, which are appropriately named “bad” and “good” collisions.

In the many experiments carried out with ultracold cesium atoms, much knowledge on its elastic scattering properties has been collected. A short excursion into scattering theory will help to understand the results.

Scattering theory treats collisions between low-energy atoms by a partial-wave expansion of the scattering wave function [Sak94]. At the energy scales we are interested in within the scope of this thesis, with cesium atoms at a temperature around or below 1 μK, the centrifugal barrier prevents collisions with nonzero angular momentum[3]. The elastic scattering process now is fully isotropic, and the only parameter governing the scattering behavior is the phase shift δ_0 between incoming and outgoing s wave.

The phase shift in the zero-energy limit is usually parameterized by the s-wave *scattering length*

$$a = -\lim_{k\to 0} \frac{\tan \delta_0(k)}{k}, \tag{2.1}$$

where k denotes the collision wave vector of the relative motion of the atoms. The scattering length completely describes the scattering behavior, independent of short-range details of the potential. A quantum mechanical interpretation of the scattering length is the position of the last node of the scattering wave function outside the interaction region. If the scattering length is negative, it signifies a virtual node in the negative range region, and this is equivalent to a attractive net interaction. Positive scattering lengths correspond to repulsive interaction. Zero scattering length means the incoming and outgoing wave functions are indistinguishable and cancel, this destructive interference implies that there is effectively no interaction at all (*Ramsauer-Townsend* effect). The scattering *cross-section* σ is in the low-energy limit given by $\sigma = 4\pi a^2$. This relation is valid for nonidentical particles, which is the case for an unpolarized trapped sample. If the sample is fully polarized, as is the case in typical BEC experiments, we have identical particles. Then, for bosons all even partial wave contributions vanish for symmetry reasons[4], and the odd contributions double, making the s-wave collision cross-section *in the low-energy limit*

$$\sigma = 8\pi a^2. \tag{2.2}$$

---

[3] Even for the lowest (angular momentum quantum number $l = 1$) contribution, an incident p-wave, the centrifugal barrier in ^{133}Cs is $k_B \cdot 37$ μK [Chi01a].

[4] In contrast, for fermions the odd partial waves vanish, which effectively means that in the s-wave limit fermions do not collide at all. This renders evaporative cooling very ineffective at low energies, and makes cooling of fermions towards the BCS transition much more difficult than achieving BEC in bosons.

The scattering length depends very sensitively on the details of the short-range interaction potential. When the potential depth is slightly lower than the threshold for the appearance of a new bound state, the scattering length a is large and negative; if it is slightly larger, a is large and positive [Dal99b]. Right at the threshold, a diverges, this is called a *zero-energy resonance*. In a van der Waals r^{-6} potential, this means that the scattering length very sensitively depends on the C_6 coefficient of this potential.

Evidence for the existence of a zero-energy resonance in cesium has been found several years ago in Paris [Arn97]. In the experiment, the s-wave collision cross-sections were measured in a polarized sample of cesium atoms in the $F = 4, m_F = 4$ state at varying temperatures between 5 µK and 60 µK[5]. The cross-section varied strongly with temperature and was found to within the experimental uncertainty fulfill the relation

$$\sigma = \frac{8\pi}{k^2}. \tag{2.3}$$

This relation is the scattering cross-section in the *unitarity limit*, where the low-energy limit $k \to 0$, which is a prerequisite for the validity of Eq. 2.2, is no longer valid.

The more general expression covering both limits is[6]

$$\sigma = 8\pi \frac{a^2}{1 + k^2 a^2}, \tag{2.4}$$

and we see that the relation between k and a characterizes the crossover between the limiting cases. At $ka \ll 1$, Eq. 2.4 simplifies to the expression for the low-energy limit, while $ka \gg 1$ signifies the unitarity limit. The validity of the unitarity case down to a temperature of 5 µK in the experiment therefore gives a lower limit of the magnitude of the scattering length of $|a| > 260\ a_0$ [Arn97], where $a_0 = 0.53$ Å denotes Bohr's radius. This lower limit is already exceptionally high as compared to the values $|a| \lesssim 100\ a_0$ measured for other alkali atoms, signifying that in Cs a zero-energy resonance is very close.

It is important to note that there is not *one* Cs scattering length. The scattering length depends on the potential between two atoms, and this in general depends on the internal state of the atoms. In cesium atoms, with their single valence electron, two atoms can form a singlet or triplet state, depending on whether the electronic spins are antiparallel or parallel, respectively. In collisions, the free atom states are projected onto the singlet and triplet potentials and thus the scattering problem can be described by the solutions for these two potentials. Correspondingly, the singlet scattering length a_S and the triplet scattering length a_T are the important parameters describing ultracold collisions. The aforementioned experiment [Arn97] measured collisions between atoms polarized in the $F = 4, m_F = 4$ ground state. This stretched state is the single state governed only by the triplet potential, thus the experiment gives

---

[5] The limit of pure s-wave scattering is well fulfilled in this case since in the polarized sample p-wave collisions are fully suppressed. The centrifugal barrier for the next-order d-wave collisions is much higher at $k_B \cdot 191$ µK.

[6] We still neglect the range of the interaction potential, i.e. assume a contact interaction.

a direct indication for the value of a_T. Collisions between atoms in all other states have to be treated as mixtures, and in particular the singlet scattering length a_S cannot be observed directly.

Collecting the experimental data then present, a paper published in 1998 [Kok98] tried to summarize the "Prospects for Bose-Einstein Condensation in Cesium" (paper title). The authors calculate large negative singlet and triplet scattering lengths, and also a negative scattering length for the magnetically trappable $F = 3, m_F = -3$ state. This would severely limit the prospects for BEC, since a condensate with attractive interactions is only stable for a very small atom number[7]. At the predicted magnitudes of several hundred a_0, the size of a stable condensate would be restricted to typically less than 100 atoms [Rup95]. However, the conclusion of a negative scattering length was rather indirect, and all experiments on collision rates could only give lower bounds for the *magnitude* of the scattering rate, as the sign plays no role in the elastic collision cross-section.

2.4 Feshbach resonances and Cs questions answered

Comprehensive results on cesium ultracold scattering properties were finally attained in a collaboration between the group experimenting with cesium in an optical dipole trap at Stanford and the theory group at NIST, Gaithersburg. In two Physical Review Letters [Chi00, Leo00], they presented a series of experiments and their subsequent theoretical analysis that allowed to pin down accurately the values of the singlet and triplet scattering lengths and the van der Waals C_6 coefficient.

The measurements rely on the observation of Feshbach resonances in ultracold collisions. Feshbach resonances in atomic interactions arise from an unbound incident (scattering) state having an energy close to a bound state in a different molecular potential [Tie93, Tie92]. If there is some coupling between the states, a similar effect as in the aforementioned zero-energy resonance occurs: When the molecular state is degenerate with the incident state, the scattering length diverges. If the molecular state lies slightly higher, the scattering length is large and positive; if it is slightly lower, large and negative. The peculiarity about Feshbach resonances is that in general different molecular states have a different magnetic moment. The position of molecular states relative to each other and to the scattering state therefore varies with the magnetic field, and the dispersive behavior of the scattering length can be observed by varying the applied magnetic field.

Figure 2.2, taken from [Chi01a], nicely illustrates the principle of Feshbach resonances. At the crossing points of scattering state and bound states, the scattering length diverges, while the elastic cross-section is unitarity limited. We see that the width of

---

[7] A homogeneous condensate with negative scattering length would always collapse, however the spatial localization introduced by the trapping potential can dynamically stabilize small condensates (see Sec. 3.2.3).

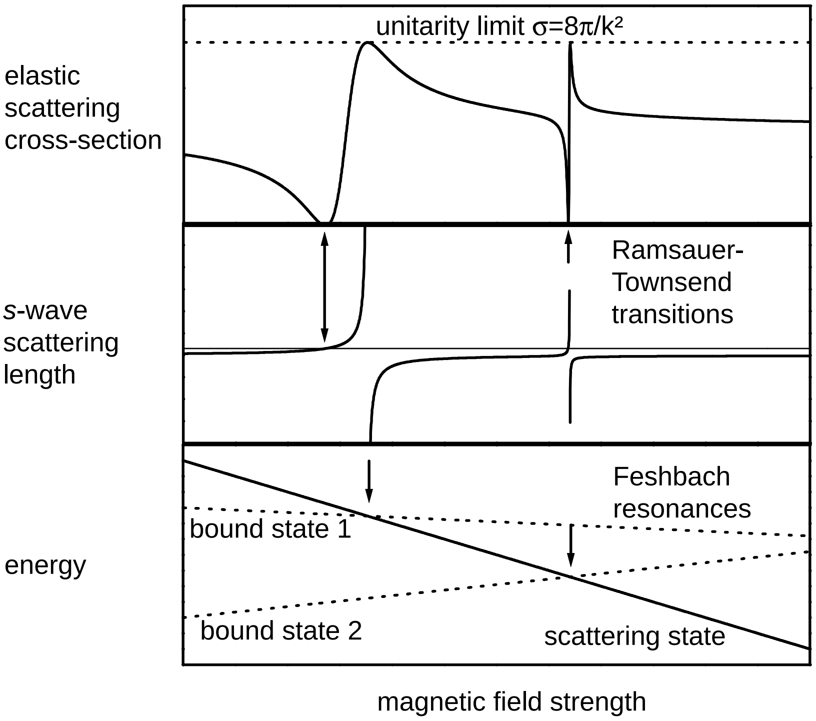

Figure 2.2: Feshbach resonances. The lowest graph shows the different magnetic field dependence of the potential energy of the scattering state and two bound states. The arrows indicate two Feshbach resonances at the level crossings. The middle graph displays the corresponding s-wave scattering length a, with zero-crossings of the scattering length (Ramsauer-Townsend effect) indicated by arrows. In the upper graph, we see the corresponding elastic scattering cross-section, which is unitarity limited to $8\pi/k^2$ for identical bosons. Figure taken from [Chi01a].

the resonances depends on the difference in magnetic moment between the scattering state and the bound states.

Feshbach resonances can only appear if there is an appreciable coupling between the different states. Here comes into play the infamous second-order spin-orbit interaction that prevented Bose-Einstein condensation in the magnetically trappable states of cesium (Sec. 2.2). This interaction couples incident s-wave states to higher angular momentum molecular states, and thus together with the relatively strong van der Waals interaction provides a rich spectrum of Feshbach resonances.

Indeed, more than 30 Feshbach resonances were found in the collision measurements presented in [Chi00], which were carried out with various mixtures of atomic states. Altogether, the Stanford experiment observed around 60 resonances in both elastic and inelastic processes [Chi01a]. All resonances could be explained by a complete model describing the Cs ground state interactions [Leo00], using only four fit parameters: the singlet scattering length a_S, the triplet scattering length a_T, the van der Waals coefficient C_6, and a general scaling factor for the indirect spin-spin cou-

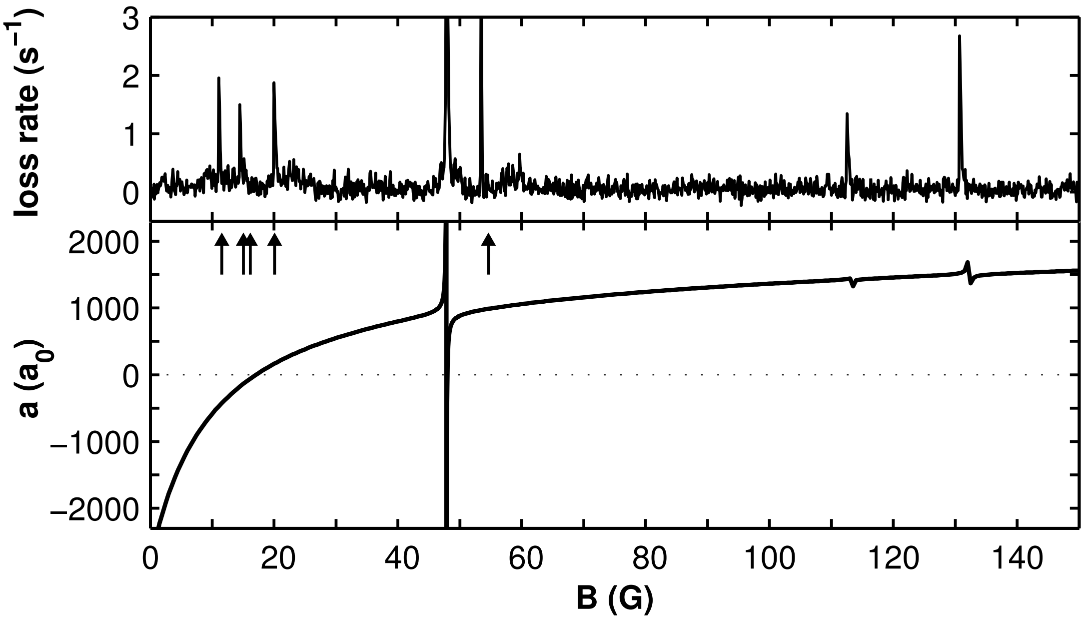

Figure 2.3: Lower graph: Calculated scattering length a [Jul03] against the magnetic field strength B for the ^{133}Cs $F = 3, m_F = 3$ absolute ground state. The calculated curve includes resonances with s and d angular momentum bound states, g-wave resonances are not visible in the scattering length but their calculated position is indicated by arrows. The upper graph shows a measurement of the radiative loss rate from the Stanford group [Chi03a], where Feshbach resonances appear as inelastic losses (cf. [Chi00, Chi03b]).

pling. The model predicts all observed resonance positions, with impressive quantitative agreement of the scattering rates.

This thorough analysis finally gave reliable values for the fundamental interaction parameters of cesium. The singlet and triplet scattering length obtained are $a_S = 280 \pm 10\ a_0$ and $a_T = 2400 \pm 100\ a_0$, respectively, the van der Waals coefficient was found to be 6890 ± 35 a.u. (1 a.u. $= 2R_\infty hca_0^6 = 0.0957345 \cdot 10^{-24}\ \mathrm{J\,nm}^6$). The model allows to calculate the scattering properties for any of the ^{133}Cs ground state substates. The calculated scattering length for the $F = 3, m_F = 3$ absolute ground state [Jul03, Ker01] at a range of magnetic fields is shown in Fig. 2.3.

We see that the scattering length varies very strongly with the applied magnetic bias field. The overall shape of the curve is dominated by an extremely broad resonance with an s-wave molecular state, with a zero crossing of the scattering length at 17 G. The other resonances visible in the scattering length curve are resonances with d-wave molecular states, while some extremely narrow g-wave resonances are not visible in the curve, but indicated by arrows.

The strong variability with the magnetic field is a very interesting feature of the Cs $F = 3, m_F = 3$ scattering length. The extremely broad variation around the 17 G zero crossing, with relatively weak dependence on the exact magnetic field strength, allows for very precise tuning of the scattering length. At the same time, the many narrow resonances, most notably the strong resonance at 48 G, allow for very quick variation over a broad scattering length range. Of great convenience is the fact that these resonances appear at magnetic field strength values very easily attainable experimentally.

In most alkali species, only very few resonances have been found, and these often appear only at very high field strengths. The first demonstration of a Feshbach resonance in a BEC was done with ^{23}Na at a bias field of 907 G [Ino98]. In the widely used ^{87}Rb, about 40 resonances have been found [Mar02], but only one, at a field of 1007 G, is wide enough to be used for tuning of the scattering length at typical experimental B-field precision. Notable exception is ^{85}Rb, where a resonance at 155 G could be exploited in a BEC [Cor00], however in this system the atoms are not in their absolute ground state and experience two-body decay.

2.5 New hope for magnetic traps

For the $F = 3, m_F = -3$ magnetically trappable state, [Leo00] predicts favorable conditions for BEC, i.e. a sufficiently high ratio of elastic to inelastic collisions, at certain magnetic field values. A recent experiment in Oxford [Tho03] tries to use that information and their previous experience to finally achieve BEC in a magnetic trap. The trapping potential is specially designed to minimize both inelastic two-body and three-body losses, and to enable evaporation at low density on extremely long time scales. Indeed, the predictions are fully confirmed, and by carefully optimizing the evaporation parameters a phase-space density of within a factor of four from the BEC transition was achieved. However, the evaporation efficiency falters in the last evaporation stages and limits the attainable phase-space density [Tho03, Ma03].

The reduced efficiency of evaporation is attributed to the *hydrodynamic regime*: At the extreme scattering lengths present in cesium, the scattering cross-sections at ultralow energy become so large that an atom collides many times during one trap oscillation period. This changes the nature of motion, rather than having single particles oscillating in the potential one now observes collective motion.

In terms of the speed of evaporative cooling, the hydrodynamic regime limits the thermalization rate. Usually, thermalization just depends on the elastic collision rate [Ket96]. However, in the hydrodynamic regime thermalization is mediated by collective rather than single-particle motion. The thermalization rate is then given by the transit time of these excitations across the sample, which is of the order of the trap oscillation period [Vul99]. Once in this regime, a further increase in density, which naturally happens in radio-frequency evaporation in a magnetic trap since the potential curvature stays constant and the temperature decreases, does not speed up the cooling process because thermalization has become density independent. However, inelastic processes happen locally and their rate continues to increase; thus, the budget of evaporation vs. inelastic losses can degrade significantly.

In the Oxford experiment, this problem is not easily solvable. Reducing the scattering length on a Feshbach resonance to avoid the hydrodynamic regime is expected to increase the rate of inelastic two-body losses [Leo00]. The group expects to improve the efficiency by implementing a novel evaporation scheme [Tho03].

2.6 Our approach to cesium BEC

The experimental setup presented in this thesis was designed to employ all previously available knowledge about the Cs scattering properties to finally achieve Bose-Einstein condensation of this elusive alkali atom.

Knowing about the many difficulties involved with magnetic trapping of ^{133}Cs, we targeted from the beginning optical trapping of the $F = 3, m_F = 3$ lowest-energy state, which is insensitive to any two-body inelastic processes. We use a very shallow optical trap formed by two CO_2 lasers. In the vertical direction, this trap is too weak to hold the Cs atoms against gravity, so a vertical magnetic field gradient enacts a counter-force of equal magnitude. The large, shallow trap was supposed to fulfill three functions:

- the large trapping volume allows for the transfer of many atoms into the trap,
- the low density minimizes higher-order inelastic loss processes, esp. three-body recombination, and
- spin-selective trapping enforces perfect spin polarization and allows for radio-frequency evaporation.

In the course of the experiments, actually none of these points was as well fulfilled as we had expected. The large volume really allows for a large ensemble to be captured in the trap, however we never optimized the mode matching to perfection and lose quite many atoms through initial plain evaporation. The low density does minimize three-body recombination losses, but on a level far higher than was initially expected. And radio-frequency evaporation works, but was not the tool that made Bose-Einstein condensation possible.

However, the basic design decisions made in setting up the experiment permitted everything necessary to succeed in the end:

- the use of a quasi-electrostatic trap and much effort to optimize the vacuum conditions keep technical heating at a minimum and allow for experiments on very long time scales,
- excellent optical access to the experiment region gives great flexibility in extending the experiment, and
- the magnetic field configuration allows to dynamically change the bias field over a large range without affecting the trap operation.

In the following chapters, the path towards our cesium BEC will be shown. Some basic thoughts on trapping forces, together with the knowledge about the peculiarities of cesium, influenced the basic experiment design done in the summer of 2000, while our group was still in Heidelberg. After our move to the University of Innsbruck in August of the same year, the experiment setup started to fill the lab. The MOT captured atoms for the first time on July 27, 2001, and for about one year the construction of further elements of the levitated trap and characterization of the system went in parallel. August 2002 saw our measurements on three-body recombination [Web03b]. We spent September with some preliminary analysis of that data and used the newly-found knowledge to modify the setup, and in the early morning hours of October 5, 2002, observed the first Bose-Einstein condensate of cesium [Web03a]. The Outlook will give a hint on what has happened since [Her03].

Chapter 3

BEC basics

The theory of Bose-Einstein condensation in dilute gases has been covered extensively in several review articles [Ket99, Dal99a, e.g.] and, recently, in a comprehensive textbook devoted exclusively to this topic [Pet02]. A very good introduction can also be found in [Bon02]. I will give an overview of the main concepts involved in the description of the phase transition and the properties of a BEC.

3.1 The phase transition

Figure 3.1 shows a commonly used illustration for the different regimes in a Bose gas. The key quantity in this picture is the thermal de Broglie wavelength

$$\lambda_{\mathrm{dB}} = \sqrt{\frac{2\pi\hbar^2}{mk_BT}}, \tag{3.1}$$

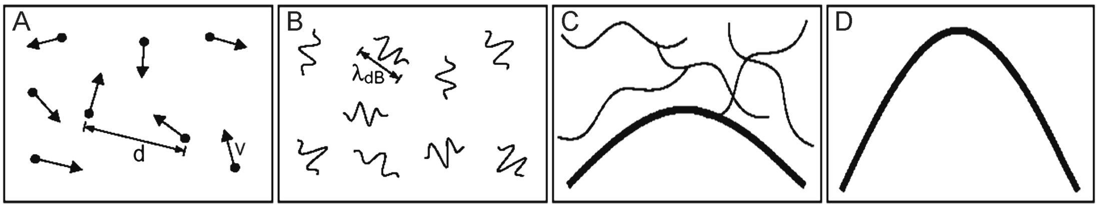

Figure 3.1: The transition from a classical gas to a Bose-Einstein condensate. (A) In the classical case at high temperature, the size of the atoms is much smaller than their average distance d, they behave as point-like particles. (B) At reduced temperatures, the thermal de Broglie wavelength λ_{dB} becomes noticeable, quantum effects start to play a role. (C) When the atomic wave functions start to overlap, the transition to Bose-Einstein condensation occurs. (D) At $T = 0$, a pure condensate remains, described by a single macroscopic wave function. Figure adapted from [Ket99].

which gives the size of the single-atom wave function at a temperature T. When a sample is cooled down, λ_{dB} increases, and if the density is kept constant or even increased during this process, at some point the wave functions of the individual atoms begin to "overlap" in space. In terms of the phase-space density

$$D = n\lambda_{\mathrm{dB}}^3, \tag{3.2}$$

which relates the number density n to the volume λ_{dB}^3 occupied in space by an atom, the start of this overlap is characterized by D approaching unity. Now, the quantum nature of the atoms comes into play, and a process akin to stimulated emission in optics leads to macroscopic population of a single state. This marks the phase transition to Bose-Einstein condensation.

To quantitatively understand this phenomenon, we take a look at quantum statistics. For non-interacting bosons in thermal equilibrium, the mean occupation number N_ν of a single-particle state ν with energy ε_ν in a trapping potential is given by the Bose distribution function [Man88]

$$N_\nu = \frac{1}{e^{(\varepsilon_\nu-\mu)/(k_B T)} - 1}. \tag{3.3}$$

The chemical potential μ that appears in Eq. 3.3 is fixed by the total particle number N via the condition $N = \sum_\nu N_\nu$, thus it can be calculated in a given external potential as a function of N and T. At high temperatures, the atoms are distributed among many energy levels, and the mean occupation number N_ν of any single state is much less than one. Consequently, the chemical potential must be much smaller than the energy ε_0 of the ground state ($\nu = 0$) of the system to keep $\exp((\varepsilon_\nu - \mu)/(k_B T)) \gg 1$ for all states. When the temperature is lowered at constant N, μ rises in order to conserve $\sum_\nu N_\nu$. However, the chemical potential can never reach or exceed ε_0 since this would imply diverging or negative occupation numbers in the ground state.

The criterion for Bose-Einstein condensation can now be obtained by considering the sum N_{ex} of the occupation numbers of the excited states ($\nu \geqslant 1$). This sum reaches its maximum for the limit of the chemical potential as $\mu \to \varepsilon_0$, yielding

$$N_{\mathrm{ex,max}} = \sum_{\nu=1}^{\infty} \frac{1}{e^{(\varepsilon_\nu-\varepsilon_0)/(k_B T)} - 1}. \tag{3.4}$$

When the temperature drops far enough that $N_{\mathrm{ex,max}} < N$, the "excess" atoms that cannot be accommodated in the excited states enter the ground state, whose occupation number N_0 can grow arbitrarily large when μ approaches ε_0. This marks the onset of Bose-Einstein condensation, and the temperature where $N_{\mathrm{ex,max}}$ drops below N is called the critical temperature T_c.

It is important to note that $k_B T_c$ is in general much higher than the energy difference $(\varepsilon_1 - \varepsilon_0)$ between the ground and first excited states. This means that the BEC forms at a temperature much above what would be necessary to just "freeze out" the motional degrees of freedom in the external potential. It also implies that above T_c the occupation number of the ground state is comparable to that of the other states, i.e. in general of order one, which is the reason why Bose-Einstein condensation appears as a distinct phase transition.

To derive a useful condition for the BEC transition, one applies some common tools of thermodynamics. It is convenient to replace the sum of states by an integral over the density of states $g(\varepsilon)$. In many contexts the density of states varies as a power law of the energy of the general form

$$g(\varepsilon) = C_\alpha \varepsilon^{\alpha-1}, \tag{3.5}$$

where α depends on the shape of the potential and C_α is a constant. Applying the integral form of Eq. 3.4 leads to a general condition for the critical temperature [Pet02]

$$k_B T_c = N^{1/\alpha} \left[C_\alpha \Gamma(\alpha)\zeta(\alpha)\right]^{-1/\alpha}, \tag{3.6}$$

where $\Gamma(\alpha)$ is the gamma function and $\zeta(\alpha) = \sum_{n=1}^{\infty} n^{-\alpha}$ is the Riemann zeta function.

For a three-dimensional harmonic oscillator potential, which is a good approximation for the kind of traps used in most experiments, the parameters are $\alpha = 3$ and $C_3 = (2\hbar^3\bar{\omega}^3)^{-1}$, where $\bar{\omega} = \sqrt[3]{\omega_x \omega_y \omega_z}$ is the geometrically averaged trap frequency. By entering these values into Eq. 3.6, we obtain a useful expression for the critical temperature,

$$T_c \approx 4.5 \left(\frac{\bar{\omega}/2\pi}{100\ \text{Hz}}\right) N^{1/3}\ \text{nK}. \tag{3.7}$$

Since the critical temperature depends on the particle number N and the trap frequency $\bar{\omega}$, it is not a convenient parameter for monitoring the progress towards condensation in an actual experiment where both N and $\bar{\omega}$ vary strongly over time. We now return to the phase-space density D introduced in the beginning of this section. For a thermal sample in a harmonic trap, the peak density $\hat{n}$ can be calculated from the Boltzmann distribution as

$$\hat{n} = N\bar{\omega}^3 \left(\frac{m}{2\pi k_B T}\right)^{3/2}. \tag{3.8}$$

Substituting Eq. 3.8 for n and Eq. 3.1 for λ_{dB} in the definition 3.2 yields an expression for the phase-space density[1] of a thermal gas in a harmonic trap,

$$D = N \left(\frac{\hbar\bar{\omega}}{k_B T}\right)^3. \tag{3.9}$$

Entering $T = T_c$ from Eq. 3.6, we find that all dependencies on the trap and sample parameters cancel out, and that in a harmonic potential the BEC transition occurs when the value calculated according to Eq. 3.9 reaches

$$D_c = \zeta(3) \approx 1.202. \tag{3.10}$$

---

[1] This is of course just the peak value at the region of highest density in the trap center. The phase-space density generally varies across a trapped sample, but usually the peak value is considered as "the" phase-space density, as it determines the crossover to BEC.

This result comes remarkably close to the naïve picture of overlapping wave functions. For other potential shapes, different values for D_c are obtained, e.g. in a 3D box potential we get $D_c = \zeta(3/2) \approx 2.612$, which is also the value in free space. Since the phase-space density can easily be calculated from the measurable quantities in a trapping experiment, it is a suitable and via the picture conveyed by Fig. 3.1 very intuitive parameter to monitor the approach to the phase transition.

The concepts developed here are suitable not only to understand the transition to the condensate, but also to calculate the number of atoms in the ground state at a certain temperature. In the typical case of a harmonic potential, the expression for the condensate fraction is fairly simple [Pet02],

$$N_0/N = 1 - \left(\frac{T}{T_c}\right)^3 . \tag{3.11}$$

We get the expected result that at $T = 0$ all atoms are in the ground state, which is true for any potential shape. The T^3 scaling, which is particular for the harmonic potential, results in a large condensate fraction at relatively high temperatures: at $T_c/2$ already 90% of the atoms are in the condensate, and at 0.2 T_c one observes an almost pure BEC with more than 99% of the atoms in the ground state.

It should be noted that all results shown here are exactly valid only in the thermodynamic limit $N \to \infty$ and for an ideal, non-interacting gas. Both finite-number and interaction effects can be treated theoretically and result in corrections of the order of a few percent [Bon02, Pet02].

3.2 Properties of a trapped Bose-Einstein condensate

The density-of-states approach is useful for describing thermal ensembles, but those standard methods are not applicable in a BEC. For this regime, a different set of theoretical tools has been developed, which I will discuss based on the treatment in [Bon02] and in [Dal99a].

The ideal gas

For an ideal gas in an external potential $U(\boldsymbol{r})$, we have the Hamiltonian $H = -\frac{\hbar^2}{2m}\nabla^2 + U(\boldsymbol{r})$, and the solution for the ground state wave function of a three-dimensional harmonic oscillator is

$$\Phi(\boldsymbol{r}) = \left(\frac{m\bar{\omega}}{\pi\hbar}\right)^{3/4} \exp\left(-\frac{m}{2\hbar}(\omega_x x^2 + \omega_y y^2 + \omega_z z^2)\right). \tag{3.12}$$

For a non-interacting gas, this is indeed exactly the condensate wave function, occupied by a large number of atoms. The shape of the wave function is a Gaussian, the width of which in each spatial direction is determined by the harmonic oscillator length

$$a_{\text{ho}} = \sqrt{\frac{\hbar}{m\omega}} \qquad \approx 8.72\,\mu\text{m} \Big/ \sqrt{\frac{\omega}{2\pi}/\text{Hz}} \;\text{ for } {}^{133}\text{Cs} \tag{3.13}$$

to $\sigma_i = a_{\text{ho},i} = \sqrt{\hbar/(m\omega_i)}$, where $i = x, y, z$. In the context of the following sections, a_{ho} without an additional index will refer to the geometric average of the oscillator length, $a_{\text{ho}} \equiv \sqrt{\hbar/(m\bar{\omega})}$.

Bogoliubov approximation

In a real gas, the wave function of the condensate is influenced by the interaction between the atoms. The general ansatz is to write down the many-body Hamiltonian in second quantization for interacting bosons in the external potential. In principle, one can directly calculate the ground state and the thermodynamic properties of the BEC from this Hamiltonian by solving the many-body Schrödinger equation, however this is very complicated. The solution is to use a mean-field approach, which allows to characterize the many-body system by a relatively small set of parameters describing quantitatively the behavior of the system. Based on an idea developed by Bogoliubov [Bog47], one decomposes the boson field operator[2] $\hat{\Psi}$ into two contributions,

$$\hat{\Psi}(\boldsymbol{r}, t) = \Phi(\boldsymbol{r}, t) + \hat{\Psi}'(\boldsymbol{r}, t), \tag{3.14}$$

where $\Phi(\boldsymbol{r}, t) \equiv <\hat{\Psi}(\boldsymbol{r}, t)>$ is the expectation value of the boson field operator and $\hat{\Psi}'$ a first-order perturbation term representing excitations. Φ is called the condensate wave function or “order parameter”, it is a complex function which via $n(\boldsymbol{r}, t) = |\Phi(\boldsymbol{r}, t)|^2$ relates to the condensate density.

3.2.1 The Gross-Pitaevskii equation

The term $\hat{\Psi}'$ in Eq. 3.14 can be neglected for temperatures $T \ll T_c$, for which the occupation of excited trap states is very small. In this case, we obtain a “zero-order” theory which describes the wave function of a pure condensate[3]. In the many-particle Schrödinger equation, $\hat{\Psi}$ is replaced by Φ, and the result is the very useful Gross-Pitaevskii (GP) equation [Gro61, Pit61]

$$i\hbar\frac{\partial}{\partial t}\Phi(\boldsymbol{r}, t) = \left(-\frac{\hbar^2\nabla^2}{2m} + U(\boldsymbol{r}) + g|\Phi(\boldsymbol{r}, t)|^2\right)\Phi(\boldsymbol{r}, t), \tag{3.15}$$

where

$$g = \frac{4\pi\hbar^2 a}{m} \tag{3.16}$$

---

[2] $\hat{\Psi}(\boldsymbol{r})$ and $\hat{\Psi}^\dagger(\boldsymbol{r})$ here denote the operators that in second quantization annihilate and create a particle at position $\boldsymbol{r}$, respectively.

[3] A discussion of finite-temperature effects can be found in [Dal99a].

is the coupling constant representing the inter-particle interactions (a denotes the scattering length).

One obtains a time-independent variant of the Gross-Pitaevskii equation by writing $\Phi(\boldsymbol{r}, t)$ as $\phi(\boldsymbol{r}, t)\exp(-i\mu t/\hbar)$, where μ is the chemical potential and ϕ is real and normalized to the total number of particles, $\int d\boldsymbol{r}\, \phi^2 = N$. Then, Eq. 3.15 becomes

$$\left(-\frac{\hbar^2\nabla^2}{2m} + U(\boldsymbol{r}) + g\phi^2(\boldsymbol{r})\right)\phi(\boldsymbol{r}) = \mu\phi(\boldsymbol{r}). \tag{3.17}$$

The total energy of the ensemble is in the stationary case a functional of the density distribution

$$E[n] = \int d\boldsymbol{r}\left[\frac{\hbar^2}{2m}|\nabla\sqrt{n}|^2 + nU(\boldsymbol{r}) + \frac{gn^2}{2}\right] = E_{\mathrm{kin}} + E_{\mathrm{ho}} + E_{\mathrm{int}}. \tag{3.18}$$

The energy terms can be assigned to different sources:

- E_{kin} is the kinetic energy, which is induced by the confinement of the condensate through the uncertainty relation,
- E_{ho} is the potential energy from the trapping potential,
- and E_{int} is the mean-field interaction energy.

The energy scale helps to understand the different regimes in a Bose gas. The derivation of the GP equation relies on the approximation that the ensemble is a dilute gas, which is defined by the relation between the density and the scattering length $n|a|^3 \ll 1$. This is also called the “weakly interacting” regime. This is true for a thermal gas, where in this case the kinetic energy is much larger than the interaction energy. However, in the condensate phase the kinetic energy of the trapped atoms is extremely small; the relation between the kinetic energy and the interaction energy can be derived from Eq. 3.18 to [Dal99a]

$$\frac{E_{\mathrm{int}}}{E_{\mathrm{kin}}} \propto \frac{N|a|}{a_{\mathrm{ho}}}, \tag{3.19}$$

and this can easily be larger than 1 even when $n|a|^3 \ll 1$. In the first BEC experiments in 1995, $N|a|/a_{\mathrm{ho}}$ was of the order 1 in a condensate of a few thousand ^{87}Rb atoms [And95] and about 10^3–10^4 in the first sodium condensate [Dav95]. In most BEC experiments, the energy scale in the condensate is dominated by the interaction term.

3.2.2 The Thomas-Fermi approximation

In the case of repulsive interactions ($a > 0$), a trapped condensate dominated by the interaction energy is stable. In this case, we can apply the Thomas-Fermi approximation, which consists in neglecting the kinetic energy term in the GP equation 3.17.

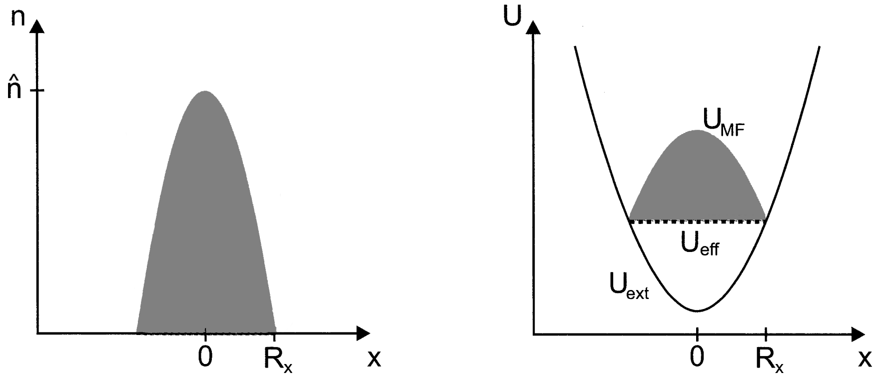

Figure 3.2: Left: Density distribution of a Bose-Einstein condensate in a harmonic trapping potential in the Thomas-Fermi limit. The shape of the condensate is an inverted parabola, reflecting the shape of the external potential. Right: The density distribution mirroring the shape of the external potential U_{ext} leads to a mean-field interaction potential U_{MF} that exactly cancels U_{ext}, resulting in a flat effective potential U_{eff}. Figure taken from [Bon02].

Solving for ϕ yields an expression for the density,

$$n(\boldsymbol{r}) = \begin{cases} \dfrac{\mu - U(\boldsymbol{r})}{g} & \text{for } \mu - U(\boldsymbol{r}) > 0, \\ 0 & \text{otherwise.} \end{cases} \tag{3.20}$$

Figure 3.2 shows the resulting density distribution. The balance of the mean-field interaction potential and the trapping potential results in a flat effective potential. The density distribution according to Eq. 3.20 differs qualitatively from the distribution of a thermal cloud or an ideal-gas condensate in that it does not have a Gaussian shape but mirrors the potential shape, resulting in the case of a harmonic potential in an inverted parabola.

Several parameters of the condensate are easily derived in the Thomas-Fermi approximation. The peak density can be directly read off Eq. 3.20,

$$\hat{n} = \frac{\mu}{g} = \frac{\mu m}{4\pi\hbar^2 a}. \tag{3.21}$$

Via the normalization condition for the density, $\int d\boldsymbol{r}\, n(\boldsymbol{r}) = N$, the chemical potential is related to the particle number as

$$\mu = \frac{\hbar\bar{\omega}}{2}\left(\frac{15Na}{a_{\mathrm{ho}}}\right)^{2/5}, \tag{3.22}$$

and the radius along one axis ($i = x, y, z$) is given by [Ket99]

$$R_i = \sqrt{\frac{2\mu}{m\omega_i^2}} = a_{\mathrm{ho}}\frac{\bar{\omega}}{\omega_i}\left(\frac{15Na}{a_{\mathrm{ho}}}\right)^{1/5}. \tag{3.23}$$

Another important parameter is the mean interaction energy per particle,

$$E_{\text{int}}/N = \frac{2}{7}\mu. \tag{3.24}$$

When the trapping potential is turned off, this energy is converted into kinetic energy and determines the expansion of the condensate. Since the interaction energy distribution follows the same inverted parabola shape as the density distribution, the expansion will also show a parabolic shape. This clearly distinguishes the condensate from a thermal cloud, and in time-of-flight expansion measurements of partially condensed samples one observes a two-component distribution with a small inverted BEC parabola sitting on top of a relatively large thermal Gaussian.

3.2.3 Attractive forces: Condensate collapse

When the force between the condensate atoms is attractive ($a < 0$), the gas tends to increase its density in the center in order to decrease the interaction energy (cf. Eq. 3.18), which is equivalent to a contraction of the BEC. A counter-acting force comes from the zero-point kinetic energy, which grows with decreasing spatial extension and can dynamically stabilize the BEC at a certain size. However, if the atom number is large, the kinetic-energy effect, which depends less strongly on n than the inter-particle interaction energy, is too weak to stop the collapse. This gives an upper limit N_{cr} to the particle number of a stable BEC, which can be calculated by numerically integrating the Gross-Pitaevskii equation to [Rup95]

$$N_{\text{cr}} = 0.575\frac{a_{\text{ho}}}{|a|}. \tag{3.25}$$

A variational calculation [Pet02] gives a slightly higher factor of 0.67. The calculations are strictly valid only for spherical traps, therefore one can expect deviations from the exact predictions in anisotropic traps. In typical experiments, the critical atom number is of the order of around a thousand.

A short discussion of the properties and dynamics of collapsing condensates is given in [Dal99a], including an overview of theoretical papers available at that time. One should note that the dynamic stabilization of the condensate is an effect of the quantum pressure induced by the spatial localization. An unconfined condensate with attractive interaction is always unstable. A comprehensive and fairly up-to-date treatment of the rich spectrum of condensate dynamics associated with different interactions and reactions to perturbations of the condensate wave function can be found in [Pet02].

Chapter 4

Trapping of ultracold atoms

The methods used in atom trapping experiments have now become a standard in hundreds of experiments around the world, and the first textbook on the matter of laser cooling [Met99] has been published several years ago now. Therefore, the discussion here will be kept short while introducing the most important terms. I will give a short explanation of the radiation pressure forces which are used to capture and precool the atoms first. The next section covers the main experimental tool in this experiment, the optical dipole force, which is used in different regimes at various steps of the cooling process towards BEC. An introduction to magnetic forces on atoms concludes the list of trapping mechanisms. Finally, I give a short treatment of loss and heating sources.

4.1 Radiation pressure forces

If an atom (treated as a two-level system) is exposed to light resonant on a closed dipole transition, it will absorb and spontaneously re-emit photons. If the light is directed, like from a collimated laser beam, the absorbed photons will impart a directional recoil momentum onto the atom. Spontaneous emission, however, occurs isotropically, therefore the recoil from the emitted photons will average to zero.

On average, each cycle of absorption and spontaneous emission will impart one photon recoil $\boldsymbol{p}_{\mathrm{sc}} = \hbar\boldsymbol{k}$. The radiation pressure force is determined by $\boldsymbol{F} = \dot{\boldsymbol{p}} = \Gamma_{\mathrm{sc}} \cdot \boldsymbol{p}_{\mathrm{sc}}$, with the spontaneous scattering rate

$$\Gamma_{\mathrm{sc}} = \frac{\Gamma}{2} \cdot \frac{S}{1 + S + (2\delta/\Gamma)^2}. \tag{4.1}$$

Here Γ denotes the natural line width of the transition, $\delta = \omega - \omega_0$ the detuning of the laser frequency ω from the transition frequency ω_0. $S = I/I_0$ is the *saturation parameter*, the relation of the laser intensity I to the saturation intensity $I_0 = \hbar\Gamma\omega_0^3/(12\pi c^2)$, at which the excitation probability in a two-level system is $1/4$.

The most important parameter in the scattering rate for many laser cooling applications is the detuning δ. It is evident that the smaller $|\delta|$, the higher the scattering rate and therefore the stronger the force. Trapping and cooling schemes rely on this relation: In an optical molasses [Chu85], six lasers detuned below the resonance point into the trap center. When an atom moves, the Doppler effect brings it into resonance with a laser beam propagating opposite to its direction of motion, and the spontaneous force slows it down. In a MOT [Raa87], the molasses is combined with a magnetic quadrupole field. The Zeeman effect, which brings the atoms closer to resonance when they are off-center, adds a centering force. A combination of these effects is also used to slow an atomic beam in a Zeeman slower (cf. Sec. 5.2). All of these laser cooling techniques are extensively covered in [Met99].

4.2 Optical dipole forces

Radiation-pressure traps limit the attainable temperatures because they rely on photon scattering to hold the atoms. The minimum energy in such a trap can be brought close to one photon recoil, equivalent to a temperature of 200 nK in the case of cesium, but not below. A handle to conservative trapping of atoms is their magnetic or electric dipole moment. Magnetic trapping will be covered in Sec. 4.3. The electric dipole forces are used in optical dipole traps, which are discussed here based on the comprehensive review in [Gri00].

Introducing an atom into an electric field $\boldsymbol{E}$ induces a dipole moment $\boldsymbol{p}$. The oscillating electric field of a laser drives an oscillation of the dipole moment, and we can view this quite analogously to a classical forced harmonic oscillator. If the driving laser frequency is below that of an atomic resonance (*red-detuned*), the dipole will oscillate in phase with the electric field, and the potential $U_{\mathrm{dip}} = -<\boldsymbol{pE}>/2$ is attractive. If the driving frequency is above the resonance frequency (*blue-detuned*), the potential is repulsive. All dipole traps employed in this work are red-detuned. Close to a resonance, the radiation pressure will dominate over the dipole force $-\nabla U_{\mathrm{dip}}$; optical dipole traps are operated in the far-detuned regime $|\delta| \gg \Gamma$, where the photon scattering rate is small.

In a complex notation, the dipole moment $\boldsymbol{p}(\boldsymbol{r}, t) = \hat{\boldsymbol{e}}\tilde{p}(\boldsymbol{r}) \exp(-i\omega t) + c.c.$ is related to the electric field $\boldsymbol{E}(\boldsymbol{r}, t) = \hat{\boldsymbol{e}}\tilde{E}(\boldsymbol{r}) \exp(-i\omega t) + c.c.$ via

$$\tilde{p} = \alpha(\omega)\tilde{E}, \tag{4.2}$$

where $\tilde{p}$, $\tilde{E}$ are the complex amplitudes. The real part of the complex polarizability $\alpha(\omega)$ gives the interaction potential $U_{\mathrm{dip}} = -<\boldsymbol{pE}>/2 = -\mathrm{Re}(\alpha)|\tilde{E}|^2$, while the imaginary part accounts for the energy P_{sc} dissipated via photon scattering, $P_{\mathrm{sc}} = \Gamma_{\mathrm{sc}} \cdot \hbar\omega = 2\pi\omega\mathrm{Im}(\alpha)|\tilde{E}|^2/c$.

In a classical Lorentz model, which considers the atom harmonically bound to its electron, the polarizability $\alpha(\omega)$ can be calculated in a straightforward way [Gri00].

The result for the dipole potential and the photon scattering rate is

$$U_{\text{dip}}(\boldsymbol{r}) = -\frac{3\pi c^2}{2\omega_0^3}\left(\frac{\Gamma}{\omega_0-\omega}+\frac{\Gamma}{\omega_0+\omega}\right)I(\boldsymbol{r}), \tag{4.3}$$

$$\Gamma_{\text{sc}}(\boldsymbol{r}) = \frac{3\pi c^2}{2\hbar\omega_0^3}\left(\frac{\omega}{\omega_0}\right)^3\left(\frac{\Gamma}{\omega_0-\omega}+\frac{\Gamma}{\omega_0+\omega}\right)^2 I(\boldsymbol{r}), \tag{4.4}$$

where $I = 2\pi\epsilon_0|\tilde{E}|^2$ denotes the intensity of the laser. As a semi-classical extension, we can insert for the damping rate Γ the quantum mechanical transition rate

$$\Gamma = \frac{\omega_0^3}{3\pi\epsilon_0\hbar c^3}\,|{<}e|\mu|g{>}|^2\,, \tag{4.5}$$

where ${<}e|\mu|g{>}$ is the dipole matrix element for the transition. Now, Eqs. 4.3,4.4 are an excellent approximation in the case of large detuning and low saturation, where the photon scattering rate is very low ($\Gamma_{\text{sc}} \ll \Gamma$).

There are different regimes in which to operate an optical dipole trap. I will discuss three cases, all of which are relevant in different stages of our experiment.

4.2.1 Near-resonant dipole traps

This kind of trap operates with laser frequencies relatively near to an atomic resonance. They are far-detuned in the sense of the relation $|\delta| \gg \Gamma$ (e.g., in the first optical dipole trap [Chu86], $|\delta| \approx 10^4\Gamma$). However, the absolute value of the detuning $\delta = \omega - \omega_0$ is much smaller than ω_0, and in Eq. 4.3 the *rotating-wave approximation* $\Gamma/(\omega_0+\omega) \ll \Gamma/(\omega_0-\omega)$ can be applied, giving

$$U_{\text{dip}}(\boldsymbol{r}) = -\frac{3\pi c^2}{2\omega_0^3}\frac{\Gamma}{\delta}I(\boldsymbol{r}). \tag{4.6}$$

Up to now, we have considered a two-level atom. In real atoms, there are more energy levels to be taken into account; in the case of the alkalis, a proper treatment of the fine structure and hyperfine structure of the D line suffices. If we are working with linearly polarized light at a detuning larger than the hyperfine splitting of the excited state (~200 MHz for Cs, see Fig. 2.1), but smaller than the fine structure splitting between the D_1 and D_2 lines (16.6 THz), the correction can be explained in simple terms. We expand Eq. 4.6 by splitting the term $\Gamma/(\omega_0^3\delta)$ into $1\Gamma_1/(3\omega_1^3\delta_1)+2\Gamma_2/(3\omega_2^3\delta_2)$, where the indices $_1$ and $_2$ denote the D_1 and D_2 lines, respectively. The factors 1/3 and 2/3 account for the relative line strengths. Since Γ scales with ω^3 (cf. Eq. 4.5), we can approximate $\Gamma_1/\omega_1^3 \approx \Gamma_2/\omega_2^3$. With the further assumption that we are working close to the D_2 line, $\delta_2 \ll \delta_1$, the result is

$$U_{\text{dip,near res.}} = -\frac{\pi c^2}{\omega_2^3}\frac{\Gamma_2}{\delta_2} \cdot I, \tag{4.7}$$

$$\Gamma_{\text{sc,near res.}} = \frac{\pi c^2}{\hbar\omega_2^3}\left(\frac{\Gamma_2}{\delta_2}\right)^2 \cdot I. \tag{4.8}$$

The assumptions made here are good for dipole traps operated at low power levels close to resonance (typically in the GHz range), which is in our experiment valid for the 3D optical lattice used in the Raman sideband cooling scheme (see Sec. 6.2). The laser used there is a diode laser detuned from resonance by 9 GHz at a power of 70 mW.

4.2.2 Far off-resonance traps (FORT)

In near-resonant red-detuned dipole traps, resonant scattering is typically strong enough to always have a small fraction of atoms in the excited state. This makes them unsuitable for the study of ground state dynamics (most prominently, for the attainment of BEC) and provides a strong loss and heating mechanism through excited-state collisions and photon scattering. Looking at Eqs. 4.7 and 4.8, we find the relation

$$\Gamma_{\text{sc}} = \frac{1}{\hbar}\frac{\Gamma}{\delta}U_{\text{dip}}. \tag{4.9}$$

Thus, the larger the detuning δ, the smaller the photon scattering rate at the same trap depth. This is used in the FORT [Mil93] by operating at very large detuning, typically in the range of several tens of nanometers or more, which in frequency units is in the THz range.

In this regime, the assumptions made in the derivation of Eqs. 4.7,4.8 are no longer valid. Instead, we start again with the more general equations 4.3,4.4. Assuming the detuning is larger than the fine structure splitting between the D_1 and D_2 lines of Cs of 42 nm, we model the system as a two-level atom with an effective transition defined by the weighted average of both D lines,

$$\omega_{\text{eff}} = \frac{1}{3}\omega_1 + \frac{2}{3}\omega_2 \quad \Rightarrow \quad \lambda_{\text{eff}} = 866 \text{ nm}. \tag{4.10}$$

In the same way we obtain an average line width

$$\Gamma_{\text{eff}} = \frac{1}{3}\Gamma_1 + \frac{2}{3}\Gamma_2 = 2\pi \cdot 5.00 \text{ MHz}, \tag{4.11}$$

and putting these into Eqs. 4.3,4.4 we get an expression for the potential and the scattering rate in the FORT:

$$U_{\text{dip,FORT}} = -\frac{3\pi c^2}{2\omega_{\text{eff}}^3}\left(\frac{\Gamma}{\omega_{\text{eff}} - \omega} + \frac{\Gamma}{\omega_{\text{eff}} + \omega}\right) \cdot I, \tag{4.12}$$

$$\Gamma_{\text{sc,FORT}} = \frac{3\pi c^2}{2\hbar\omega_{\text{eff}}^3}\left(\frac{\omega}{\omega_{\text{eff}}}\right)^3\left(\frac{\Gamma}{\omega_{\text{eff}} - \omega} + \frac{\Gamma}{\omega_{\text{eff}} + \omega}\right)^2 \cdot I. \tag{4.13}$$

Note that in this case neither the rotating wave approximation is valid (the contribution is 10.3% for a laser at 1064 nm), nor can the term $(\omega/\omega_{\text{eff}})^3$ in Γ_{sc} be omitted (gives about a factor of two at 1064 nm).

A FORT is implemented in this experiment by the “dimple” (see Sec. 8.2), which is formed by a focused beam from an Yb fiber laser at 1064 nm with a maximum power of 150 mW.

4.2.3 Quasi-electrostatic traps (QUEST)

Lasers at Nd:YAG wavelength (1064 nm) are available at high powers at moderate cost and are frequently used in optical trapping experiments. However, in in the center of a 1064 nm FORT with a trap depth of $k_B \cdot 20$ μK, the photon scattering rate for cesium atoms calculated by Eq. 4.13 is approximately $(8\ \text{s})^{-1}$. Thus, in a 1 minute experimental cycle, each atom would scatter about seven photons. If we assume that the cooling towards BEC in a temperature range around or below one hundred nanokelvin might take that long, seven photon recoils of ~200 nK each would effectively make condensation impossible. Since in the initial planning stages of the experiment the time scale for the attainment of BEC was not clear, conservative thinking suggested looking for a better solution.

The solution was found in a concept that takes the advantages of the far off-resonance trap to the extreme. The QUEST [Tak95] operates at a laser wavelength of 10.6 μm. The frequency of this laser is so small that the *quasi-electrostatic* approximation $\omega \ll \omega_0$ is valid. In this approximation, equations 4.12 and 4.13 simplify further to

$$U_{\text{dip,QUEST}} = -\frac{3\pi c^2}{\omega_{\text{eff}}^4}\Gamma_{\text{eff}} \cdot I, \tag{4.14}$$

$$\Gamma_{\text{sc,QUEST}} = \frac{6\pi c^2}{\hbar\omega_{\text{eff}}^5}\left(\frac{\omega}{\omega_{\text{eff}}}\right)^3 \Gamma_{\text{eff}}^2 \cdot I. \tag{4.15}$$

Here we use the effective line width and transition frequency of the weighted average of the D_1 and D_2 lines as defined in the previous section. A different treatment uses the measured *static polarizability* of the ground state of the cesium atom of $\alpha_{\text{stat}} = 6.63 \cdot 10^{-39}\ \text{Cm}^2/\text{V}$ [Lid97]. The relation between potential U and light intensity I is then given by the simple expression

$$U_{\text{dip,QUEST}} = -\frac{\alpha_{\text{stat}}}{2\epsilon_0 c} \cdot I, \tag{4.16}$$

which results in values about 5% higher than obtained from Eq. 4.14. I will use this relation in further trap potential calculations. In general, since the laser is far red-detuned from any atomic dipole resonance, the potential of a QUEST is attractive for all atomic species and can be calculated by the static polarizability. Even trapping of molecules has been demonstrated [Tak98].

The relation between the photon scattering rate and the trap depth in the QUEST can be obtained from a comparison of Eqs. 4.14 and 4.15:

$$\Gamma_{\mathrm{sc}} = \frac{2}{\hbar}\left(\frac{\omega}{\omega_{\mathrm{eff}}}\right)^3\left(\frac{\Gamma_{\mathrm{eff}}}{\omega_{\mathrm{eff}}}\right)U_{\mathrm{dip}}. \tag{4.17}$$

In the center of a 20 μK trap, the scattering rate results to $4.1 \cdot 10^{-5}$ s^{-1}. This corresponds to 3.6 photons per day and can be safely ignored for experimental purposes. The power necessary to create the same potential as with a FORT at 1064 nm is higher by a factor of 2.96; this is no problem, however, as CO_2 lasers are readily available with cw powers in the kilowatt range at relatively low cost. In our experiment, the "working horse" main trap is a QUEST created by the crossed foci of two 85 W CO_2-laser beams.

4.3 Magnetic forces

As opposed to the electric dipole moment, which is induced by the electric field, any atom with total spin ≠0 has a permanent magnetic dipole moment $\boldsymbol{\mu}$, which in a magnetic field $\boldsymbol{B}$ leads to a potential $U_{\mathrm{mag}} = -\boldsymbol{\mu} \cdot \boldsymbol{B}$.

Quantum mechanically, the energy $\boldsymbol{\mu} \cdot \boldsymbol{B}$ is quantized according to the projection of the spin operator onto the magnetic field axis. Due to Larmor precession, the atomic spin follows the magnetic field vector $\boldsymbol{B}$ adiabatically as long as the Larmor frequency ω_L is large compared to the rotation frequency of the magnetic field axis in the frame of reference of the atom. This is typically true for ultracold atoms moving in magnetic fields generated by macroscopic coils, as long as there is no zero crossing of the magnetic field, which can abruptly reverse the $\boldsymbol{B}$ field axis.

Because of this adiabatic following, the potential energy of an atom in a magnetic field is dependent on just the field strength B, and the quantized energy sublevels of the potential are given by $U_{\mathrm{mag}} = m_F g_F \mu_B B$, where g_F denotes the Landé factor, $\mu_B \simeq -9.3 \cdot 10^{-24}$ J/T Bohr's magneton, and the quantum number m_F can take the values $-F, -F+1, \ldots, F$. For cesium in the $F = 3$ ground state, the Landé factor can be calculated to $g_F = -1/4$ [Hak00, Ste02]. The result for the potential energy of an atom in the $F = 3, m_F = 3$ absolute ground state in a magnetic field B is

$$U_{\mathrm{mag}}(F = 3, m_F = 3) = -\frac{3}{4}\mu_B B = -k_B \cdot 50.4\,\mu\mathrm{K} \cdot B/\mathrm{G}. \tag{4.18}$$

It should be noted that this state cannot be captured in a magnetic trap, since creating a potential energy minimum for this "strong-field seeker" would require a local maximum of the magnetic field, which is forbidden [Win84]. In our experiment, we want to cancel the gravitational force. The gravitational potential is $U_{\mathrm{grav}} = m_{\mathrm{Cs}} g z$, where $g = 9.81$ m/s^2 denotes the gravitational constant, z the vertical position. In temperature units, we get

$$U_{\mathrm{grav}} = 1568\,\mu\mathrm{K} \cdot z/\mathrm{cm}, \tag{4.19}$$

and together with Eq. 4.18 the required vertical magnetic field gradient for levitating ^{133}Cs in the desired state is

$$\frac{\partial B}{\partial z} = \frac{4}{3}\frac{m_{\mathrm{Cs}} g}{\mu_B} = 31.3 \text{ G/cm}. \tag{4.20}$$

A more precise treatment has to include the quadratic Zeeman effect, which expands Eq. 4.18 to

$$U_{\mathrm{mag}}(F = 3, m_F = 3) = -\frac{3}{4}\mu_B B + \frac{15}{16}\frac{\mu_B^2}{\Delta E_0} B^2, \tag{4.21}$$

where $\Delta E_0 = h \cdot 9.193$ GHz denotes the Cs ground state hyperfine splitting. The correction as compared to the linear Zeeman effect is typically a few percent.

4.4 Loss & heating

Every real-world atom trapping setup includes some mechanisms which lead to loss of atoms from the trap or heating of the ensemble. In the following sections, I will try to evaluate the most important loss and heating mechanisms that are applicable to our setup. The treatment here includes only single-particle losses as an effect of the trapping setup. Loss and heating arising from interactions in the trapped sample are treated in Ch. 7.

Photon scattering

The topic of photon scattering in the optical dipole traps has been treated in Sec. 4.2. In conclusion, in a CO_2-laser trap photon scattering is negligible. In a FORT, one has to take care of the time scale the experiment takes. In a near-resonant optical lattice, the photon scattering rate is considerable. We actually use this for cooling (see Sec. 6.2), but spontaneous emission limits the maximum time we keep the atoms trapped in the lattice to about ten milliseconds.

Background gas collisions

The typical background gas pressure attainable in a room temperature environment is at or a little below $p = 10^{-11}$ mbar. In a stainless steel chamber like the one used in our experiment, the main components from outgassing of the chamber walls is hydrogen. In between large glass surfaces, diffusion of He also plays an important role.

Background gas molecules are in thermal contact to the laboratory environment at 300 K, while the trapping potentials in our experiment have a depth of only a few µK. Thus, a collision with background gas atoms typically leads to immediate loss from the trap. This process results in exponential loss of atoms from the trap, a calculation of the $1/e$ lifetime based on [Bjo88] gives at $p = 10^{-11}$ mbar a result in the range above one hundred seconds [Web00]. The precise number depends on the exact composition of the background gas, which we cannot determine in our apparatus.

Heating arises from diffractive collisions [Bal99], which impart only a very small part of the background gas molecule's energy onto the trapped atom. The probability for such an event, however, is extremely small in our shallow trap, and as such can be neglected [Eng00a].

Trapping potential fluctuations

Intensity fluctuations and beam pointing instabilities of the trapping laser modulate the potential shape of the optical dipole trap and can induce parametric heating [Sav97, Geh98]. Motivated by these theoretical considerations, O'Hara et al. [O'H99] in their first experimental demonstration of long-time storage of atoms in a quasi-electrostatic trap employed an extremely stable, self-built CO_2-laser system. However, a look at the calculations shows that the relevant figure for intensity noise of their laser is two orders of magnitude lower than required in experiments on the timescale of several hundred seconds [Web00]. Experiments conducted in our group [Eng00b] have proven the stability of a standard industrial CO_2 laser to be sufficient for long-time, low-heating measurements with ultracold atoms.

Position instabilities are more difficulty to analyze quantitatively. Typical CO_2-laser resonator design, however, ensures a high pointing stability of the output beam, and the optical path to the experiment can be set up with stable optics mounts to avoid any mechanical vibrations. The positive experience in our group supports the conclusion that laser fluctuations are not a major source of heating in a QUEST.

Similar considerations apply to magnetic forces. Here, the long-standing experience in many magnetic trapping experiments, which were the first to lead to a BEC, shows that with moderate effort the field stability can be maintained at a high level. In our experiment, the magnetic field plays only a minor role as a trapping force, and the field stability has proven not to be critical as a heating source.

Chapter 5

Technical setup

Many requirements have to be met to laser cool and manipulate dilute gases of ultracold atoms. To isolate the atoms from the laboratory environment, they are kept under ultrahigh vacuum (UHV) conditions. The Zeeman slowing technique requires careful magnetic field design to slow the atoms from their initial speed of several hundred meters per second to a velocity within the capture range of a magneto-optical trap. The atoms are captured and pre-cooled via optical forces that are supplied by diode lasers. Precise control of the magnetic fields is essential for our trapping scheme in every stage of the experiment, and the CO_2 lasers require some particular effort to operate. The last part of this chapter is dedicated to the computer system that controls the experiment timing.

5.1 The vacuum system

The vacuum system is basically an airtight stainless steel compartment with several integrated pumps and a cesium source. The setup comprises four parts: The *cesium oven* is the source of a cesium atomic beam. The *differential pumping section* keeps the pressure difference of several orders of magnitude between the oven and the experiment region. It also provides a shutter for the cesium beam. The *central experimental chamber* provides the space and optical access for the atom trap. All experiments are carried out in the center of this chamber. Finally, the *main pumping section* creates the ultrahigh vacuum conditions necessary for precision experiments.

The four sections are connected in a linear setup with a total length of 1.66 m. The components are aligned along a single optical axis at a height of 250 mm above the optical table which the vacuum system is fixed to. A complete cross-section through the central axis is shown in Fig. 5.1.

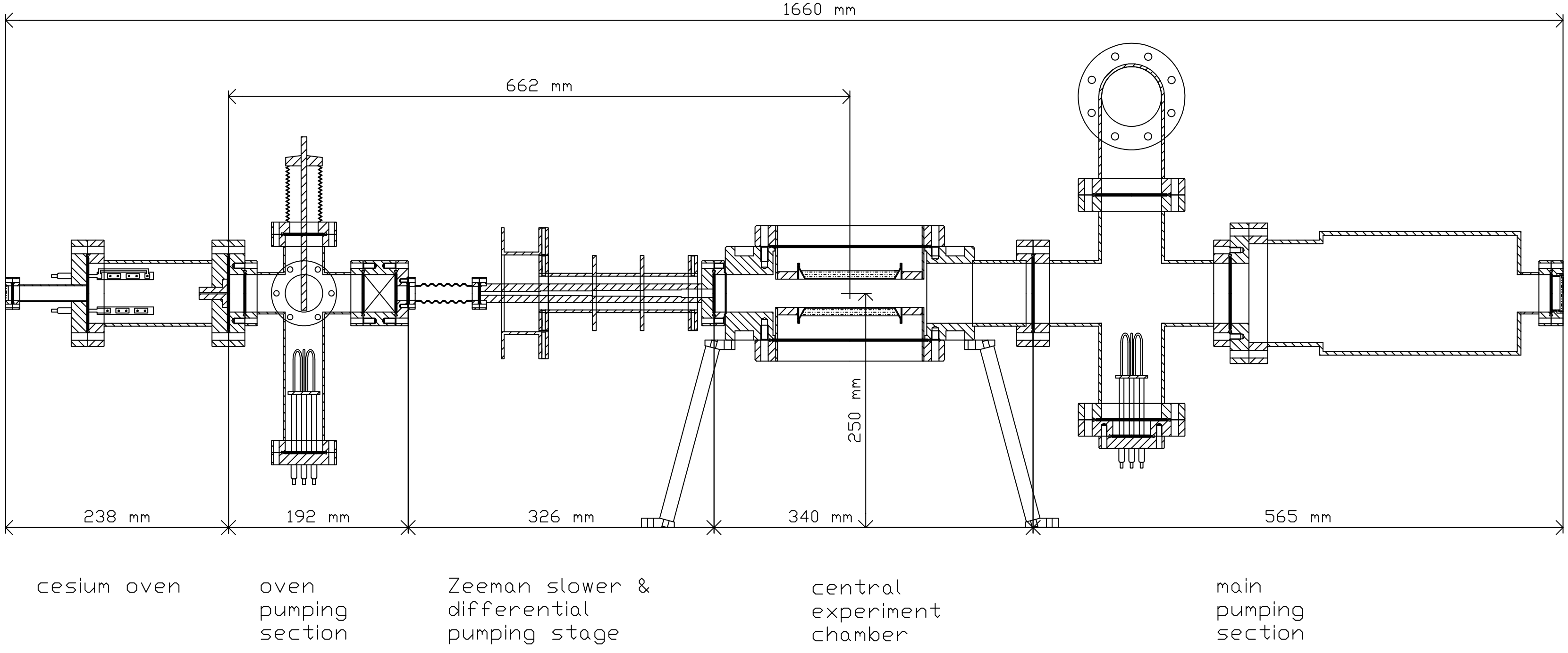

Figure 5.1: Overview of the vacuum system (side view). From left to right: (1) cesium oven with the electrical feedthroughs for the dispenser current, (2) pumping section with the beam shutter and titanium sublimation pump; in front and back: Varian UHV-24p ionization gauge and VAT series 54 all-metal angle valve, Varian Vacion Plus 20 StarCell 20 l/s ion getter pump, (3) VAT series 01 viton sealed gate valve, (4) differential pumping tube with Zeeman slowing coils, (5) experiment chamber, (6) main pumping section with titanium sublimation pump; in front and back on upper T-piece: Varian UHV-24p ionization gauge and VAT Series 57 all-metal angle valve, (7) 60 l/s Varian triode ion getter pump.

5.1.1 Cesium oven

The cesium oven is basically a 64 mm diameter stainless steel tube with a 30 mm long, 1.5 mm diameter copper nozzle on one end. The nozzle collimates the cesium atoms leaving the oven into an effusive beam with an opening angle of 6°. Four stainless steel current feedthroughs (Vacuum Generators ZEFT1AN) hold ten cesium dispenser sticks (SAES Getters CS/NF/8/25 FT10+10) (cf. Fig 5.2) to provide the cesium vapor. The ten dispensers together contain a total of 108 mg of cesium. They are activated for the first time by sending a current of 5-7 A through them, the typical operating current is between 2 A and 4 A. The dispensers provide an almost pure cesium vapor.

The oven is heated by a wrapping of heating tape to 100 °C. At this temperature, the most probable thermal velocity of cesium is 215 m/s [O'H89], the vapor pressure is $7 \cdot 10^{-4}$ mbar [Ste02]. At the typical 3.5 A operating current the dispensers probably do not set free enough cesium to saturate the vapor, but we cannot measure the pressure in the oven directly and therefore will assume $p_{\text{oven}} = 7 \cdot 10^{-4}$ mbar.

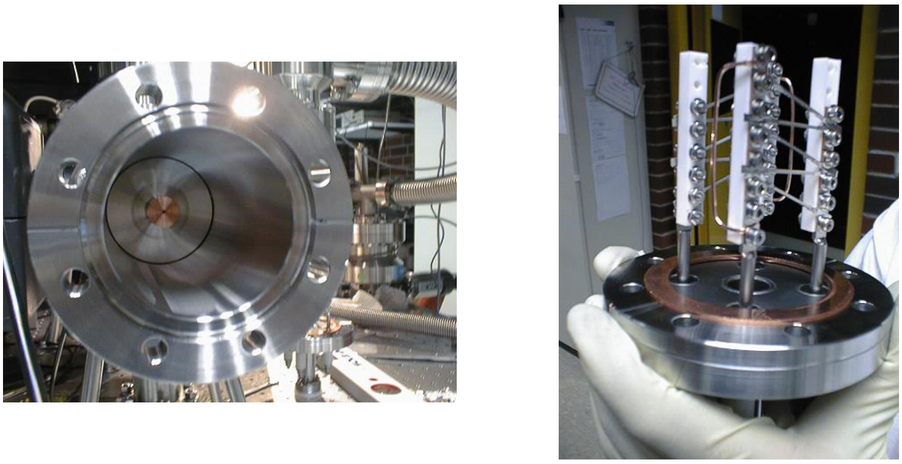

Figure 5.2: A look into the cesium oven tube (left) and the dispensers mounted to the current feedthroughs (right) before assembly of the oven setup.

5.1.2 Differential pumping

Differential pumping maintains the pressure difference between the oven and the experiment region. It is provided by two measures: good pumping and a low conductance between the regions. In the following paragraphs, the pumping geometry is explained, with the formulas and typical numbers taken from [O'H89].

The first differential pumping stage is implemented by the oven nozzle and the pumps mounted onto the 6-way cross the oven is connected to. From below, a titanium sublimation pump (Vacuum Generators SBST110) is mounted into the crosspiece. The titanium sublimation pump consists of three 2 mm diameter rods of an alloy of 85% Ti and 15% Mo. Sending a current of 60 A through one of these rods for about 1 minute heats it enough to sublimate Ti and sputter the surrounding walls with a thin film. Titanium is a surface getter for almost all active gases, with an average pumping speed per area of ~5 $\mathrm{ls^{-1}cm^{-2}}$. In our geometry, the Ti coating is applied to a surface of approx. 180 $\mathrm{cm^3}$, giving a pumping speed of ~900 l/s for air. As we do not know the pumping efficiency for the Cs vapor, the pumping speed per area may vary by a factor of 2-3 up or down (typical values are between ~3 $\mathrm{ls^{-1}cm^{-2}}$ and ~20 $\mathrm{ls^{-1}cm^{-2}}$). An additional uncertainty is the geometry of the deposition of Ti on the surfaces; if this is not isotropic from the sublimation rods, the effective pumping surface may be much smaller than calculated. We have no way of observing the area covered with titanium. As a rule of thumb, the pumping speed of the titanium sublimation pumps can be considered an estimation to within a factor of about five.

The sublimation pump does not absorb inert molecules like the noble gases and methane; to pump those, a 20 l/s ion getter pump (Varian Vacion Plus 20 StarCell) is attached next to the sublimation pump.

Under ultrahigh vacuum conditions, the mean free path Λ of a gas atom or molecule is much larger than the dimensions of a typical vacuum system. For air at room temperature, $\Lambda \simeq 60$ m at $p = 10^{-6}$ mbar, increasing linearly at lower pressure. For the cesium gas in the oven at 100 °C, $\Lambda \simeq 170$ m if we assume the pressure to be equal to the cesium vapor pressure of $7 \cdot 10^{-4}$ mbar. Therefore, the condition of the mean free path being much larger than the dimensions of the system is well fulfilled in every part of our setup. This regime, in which gas molecules do not interact with each other and the viscosity is not defined, is called the *molecular flow* regime. It is well understood and allows to calculate the gas flow and conductance of various tube geometries easily.

A characteristic quantity of the gas for which flow and conductance are to be calculated is its average thermal velocity v given by

$$v = \sqrt{\frac{8k_B T}{\pi m}}, \tag{5.1}$$

where m is the mass of a gas molecule, T the temperature. The main gas load in our vacuum chamber, as far as maintaining the pressure difference between the oven and the experiment chamber is concerned, is the hot cesium gas at 100 °C. The average thermal velocity results as $v = 244$ m/s.

The conductance C of a long round tube with diameter d and length l is given by the relation

$$C_{\text{tube}} = \frac{\pi}{12} v \frac{d^3}{l}. \tag{5.2}$$

To calculate the pressure maintained in the pumping region, one compares the vacuum setup to an electrical circuit. Tubes with finite conductance C are equivalent to resistors with resistance $1/C$, while the equivalent of the electrical potential is the pressure p. A pump with a given pumping speed X can be treated as a conductance $C = X$ towards open space ($p = 0$). Therefore, if volume no. 1 with a pressure p_1 is connected via a conductance C_{tube} to volume no. 2 which is pumped with a pumping speed C_{pump}, the pressure p_2 results as

$$p_2 = \frac{C_{\text{tube}}}{C_{\text{tube}} + C_{\text{pump}}} p_1 \approx \frac{C_{\text{tube}}}{C_{\text{pump}}} p_1. \tag{5.3}$$

The approximation is valid if the pumping speed C_{pump} is much larger than the conductance of the connection C_{tube}, which is true for both differential pumping stages in our apparatus.

Following Eq. 5.2, the nozzle of the cesium oven, at $l = 30$ mm and $d = 1.5$ mm, has a conductance for the hot cesium gas of $C_{\text{nozzle}} = 7.18 \cdot 10^{-3}$ l/s. With the pumping speed of the titanium sublimation pump $C_{\text{pump}} \approx 900$ l/s, the improvement in pressure between the oven and the pumping section is calculated to $C_{\text{pump}}/C_{\text{nozzle}} = 1.25 \cdot 10^5$. Assuming $p_{\text{oven}} = 7{\cdot}10^{-4}$ mbar, the pressure in the pumping section p_{pump} is expected to value $4{\cdot}10^{-9}$ mbar. Indeed, when the oven dispensers are turned on, an ionization gauge (Varian UHV-24p) mounted opposite the ion getter pump measures $p_{\text{pump}} \approx 10^{-8}$ mbar. The difference of a factor of two is well within the accuracy of the pumping speed estimation.

The second differential pumping stage consists of the Zeeman slower tube (cf. Sec. 5.2) in conjunction with the main pumping section (Sec. 5.1.4). The tube is composed of five consecutive sections of a stepwise larger diameter. Length l and diameter d of the sections given as $l \times d$ (each in mm) are: 65×4, 55×5, 55×6, 40×7, 35×9. The total conductance C_{Zeeman} is given by [O'H89]

$$\frac{1}{C_{\text{Zeeman}}} = \frac{1}{C_1} + \frac{1}{C_2} + \frac{1}{C_3} + \frac{1}{C_4} + \frac{1}{C_5}, \tag{5.4}$$

where C_1 to C_5 are the conductances of the five sections of different diameters as calculated by Eq. 5.2. The resulting conductance for cesium is $C_{\text{Zeeman}} = 3.40 \cdot 10^{-2}$ l/s. Together with the pumping speed of the main pumping section of 200 l/s (Sec. 5.1.4), the differential pumping across this tube should support a pressure difference of a factor of 6000. We observe that the pressure in the main vacuum chamber stays always about three orders of magnitude lower than in the first pumping section if the pressure there is varied, which is in good agreement with the calculation, considering the inaccuracy of the pumping speed and conductance determinations.

Both the ion getter and the titanium sublimation pumps operate efficiently only under high vacuum conditions. Next to the ionization gauge, an all-metal angle valve (VAT series 54) allows to connect a turbomolecular pump, which in conjunction with a roughing pump can bring the vacuum vessel from atmospheric pressure into the 10^{-8} mbar range.

Mounted on the upper flange of the 6-way pumping crosspiece, a wobble stick with a 6 mm diameter circular rod acts as an atomic beam shutter. The wobble stick is moved via an externally mounted hinge by an electric servo drive. Activated by a TTL signal from the control computer, the rod can be moved into the atomic beam path, completely blocking the line-of-sight between the oven nozzle and the Zeeman slower tube. This shuts off the atomic beam going to the experiment region after loading the atom trap, otherwise the beam would locally increase the pressure to unacceptable values. A viton sealed gate valve (VAT series 01) allows to completely separate the oven section from the main vacuum chamber, which makes it possible to replenish the cesium dispensers if necessary without breaking the vacuum in the main chamber.

5.1.3 Experiment chamber

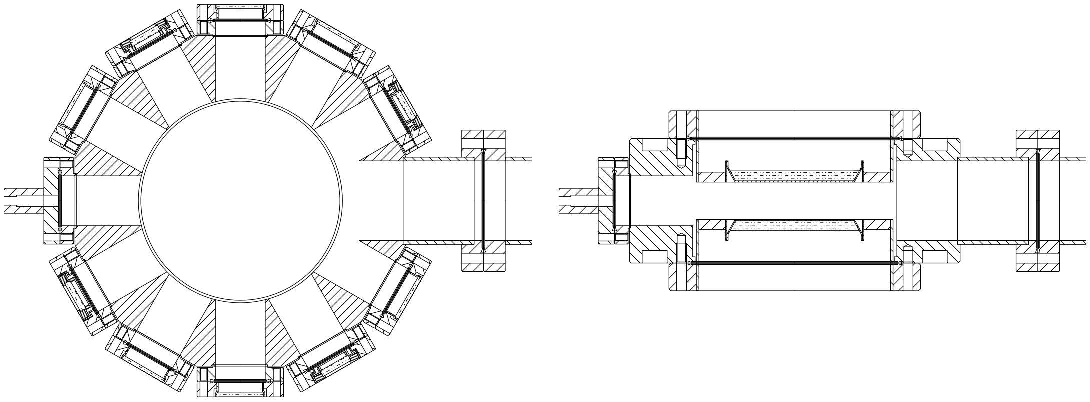

Figure 5.3: Central vacuum chamber. Top (left) and side view (right) of the heart of our experimental setup. 4 ZnSe- and 6 Quartz viewports are distinguishable in the top view.

The main experimental chamber is shown in Fig. 5.3. It was produced in the institute workshop from non-magnetic stainless steel of grades AISI 316LN (DIN W.-Nr. 1.4429) and AISI 316L (1.4435). Both materials are virtually ferrite-free and specified with a magnetic permeability of $\mu \leqslant 1.005$. All weldable flanges directly connected to the main chamber body are 316LN material, which has the higher hardness (all flanges from Vacuum Generators, various types). The tubings are made from 316L, which is easier to process. The chamber body has been milled from a massive block of stainless steel grade 316LN (Höverstahl 1.4429 ESU). The basic shape is a cylinder of 275 mm diameter and a height of 100 mm. It was milled to a 12-sided footprint with an edge length of 70mm. A central bore of 164 mm diameter along the cylinder axis provides the experimental space. From 11 of the side faces, 40 mm bores give optical access. To each of these, a CF40 flange is welded with the outer flange face at a distance of 145 mm from the trap center. The 12th face is opened up to a diameter of 64 mm for better pumping speed and welded to a 316L tube of 64 mm diameter and 62 mm length with a final CF63 flange at a distance of 195mm from the trap center. On the top and bottom faces of the main cylindrical shape, CF150 flanges have been milled into the chamber body.

To the CF40 flange opposite to the main pumping section, the Zeeman slower tube is connected. The remaining ten CF40 flanges are occupied by viewports, six quartz viewports with 35 mm clear view (Larson Electronic Glass VQZ-150-F2-AR with anti-reflection (AR) coating 850-1050 nm) and four ZnSe viewports with 22 mm clear view (Larson, AR coating 10.6 μm). The four ZnSe viewports are placed at 90° angles to accommodate the crossed-beam CO_2-laser trap (Sec. 5.5), they are distinguishable from the six quartz viewports in the top view in Fig. 5.3 by their different construction.

On the top and bottom faces of the chamber body, the CF150 flanges hold two large custom-made re-entrant viewports (United Kingdom Atomic Energy Authority, Special Techniques Group; AR coating 852-1064 nm by Laseroptik Garbsen). Their construction includes a 158 mm diameter stainless steel tube ranging 35 mm into the vacuum chamber, closed off by a stainless steel plate of 8 mm thickness. In the center of this plate, a 95 mm diameter quartz window is enclosed. The inner faces of the two viewports have a distance of 30 mm from each other, giving excellent optical access and the opportunity to mount magnetic field coils close to the trap center.

To minimize magnetic field distortion, all viewports are made from 316LN stainless steel with non-magnetic seals. The connections to the vacuum chamber are made with titanium bolts (Grade 2 titanium, Gustoc-Titanbau GmbH) because stainless steel bolts were not available in non-magnetic grades.

5.1.4 Main pumping section

The main pumping section provides the UHV base pressure for the experiment chamber and supports differential pumping against the Cs oven pressure (Sec. 5.1.2). The titanium sublimation pump (Vacuum Generators SBST110) mounted here coats a surface of approx. 700 cm^3, which is good for a pumping speed of 3500 l/s (cf. Sec. 5.1.2). This pump, however, is connected to the main chamber through an aperture of 64 mm diameter, which limits the pumping speed at the experimental region to ~200 l/s for the hot Cs gas from the oven, ~400 l/s for air at room temperature [O'H89]. A 60 l/s ion getter pump (Varian VacIon 911-5034) provides noble gas pumping.

The pressure in the vacuum chamber is measured by an ionization gauge (Varian UHV-24p) mounted onto a T-cross above the titanium sublimation pump. Thus, the sublimation pump sits between the gauge and the experimental region, causing a systematic error in the pressure measurement. The gauge reads typically between $5 \cdot 10^{-12}$ mbar and $1 \cdot 10^{-11}$ mbar. The lifetime measurements in our atom trap give very long time scales consistent with a pressure in the low 10^{-11} mbar range or below in the experiment region.

Opposite to the ionization gauge, an all-metal angle valve (VAT series 57) provides access for roughing the vacuum system.

5.1.5 Preparation

The pressure attainable in a vacuum system is determined by an equilibrium between the flux of gases into the chamber and the pumping rate. In our case, where good optical access is required, we cannot install arbitrarily large pumps close to the experiment region. Therefore, to reach UHV conditions, we have to minimize the gas load.

In a stainless steel chamber with CF flanges and UHV grade viewports, the leak rate from the outside environment is negligible except for a small flux of Helium through large glass surfaces. The main source of vacuum pollution is outgassing of impurities (in stainless steel mainly hydrogen) from the chamber walls. It is therefore imperative to remove these impurities.

Simple cleaning with acetone is the first step but only removes surface contamination. The speed of outgassing of impurities which sit deeper inside the walls increases exponentially with temperature. Therefore, exposing the apparatus to an elevated temperature under vacuum for some amount of time will clean the system.

The baking procedure was executed in two steps. In a first step, the main vacuum chamber and pumping section were closed off with blank flanges instead of the viewports. This setup was then heated at 350 °C for five days while pumping with a turbomolecular pump, which kept the pressure at $\sim 10^{-6}$ mbar. After cooling down, the base pressure was measured to be below 10^{-10} mbar. This baking procedure was used to pre-clean the stainless steel components of the vacuum system to a high degree. This cannot be done with viewports installed since those are not designed for baking temperatures this high.

The second baking step was then implemented with the vacuum system fully assembled. The starting pressure with two turbomolecular pumps working was $\sim 10^{-8}$ mbar. The temperature was slowly raised to 195 °C at a speed of 2 °C per hour, since especially the large inverted viewports are sensitive to temperature gradients and the ZnSe viewports are specified to a maximum baking temperature of 200 °C. Through careful insulation, the temperature varied by no more than five degrees centigrade across the whole structure. The temperature was held for ten days; in this time, the pressure at the elevated temperature sank from initially $\sim 10^{-6}$ mbar to $\sim 10^{-7}$ mbar. After lowering the temperature slowly to room temperature again and turning on the ion getter pumps, the pressure was below 10^{-10} mbar. Flashing the titanium sublimation pumps lowered the pressure to the final value of $\sim 10^{-11}$ mbar. The vacuum apparatus has been closed off and untouched (with the exception of occasionally flashing the titanium sublimation pumps) since then, which at the time of this writing covers a time period from June 2001 till July 2003.

5.2 The Zeeman slower

One primary design goal for an atom trap is to maintain excellent vacuum in the experiment region. How this goal is achieved is described in the previous section. A second important goal is a high loading rate, which is necessary for short experiment cycle times. The most probable velocity for atoms leaving the Cs oven is 215 m/s. As the capture velocity of the magneto-optical trap is a few 10 m/s, below 0.1% of the atoms from the unslowed atomic beam could be captured by the MOT.

A proven method for slowing down an atomic beam is the Zeeman slowing technique [Phi82, Pro85]. The atoms are decelerated by resonant photon scattering from a counter-propagating laser beam, where the Doppler shift of the quickly moving atoms is compensated by a DC magnetic field via the Zeeman effect. As the atoms are slowed down, the magnetic field needs to be adjusted for the Zeeman effect to match the Doppler effect. This is achieved by the magnetic field spatially decreasing along the beam axis, so that atoms of decreasing velocity classes are addressed by the slowing laser along the beam path. If the magnetic field decreases slowly enough, all atoms slower than a maximum velocity determined by the highest magnetic field are decelerated to below the MOT capture velocity.

The Zeeman slower used in this experiment is a carbon copy of the design employed in the GOST experiment in our group [Man99, Mos99]. It uses four coils of 180, 135, 115, and 92 turns, respectively. The first coil has a mean diameter of 11 cm, the others 6 cm each. The aluminum carrier for the slowing coils is visible in Fig. 5.1. With the first (large) coil operated at 4 A and the following three at 2 A, the slower is designed to decelerate atoms from a 160 m/s maximum velocity [Mos99]. However, experimental optimization in our setup gave optimum loading at 3.5 A and 1.75 A, respectively. A calculation of the resulting field geometry is shown in Fig. 5.4.

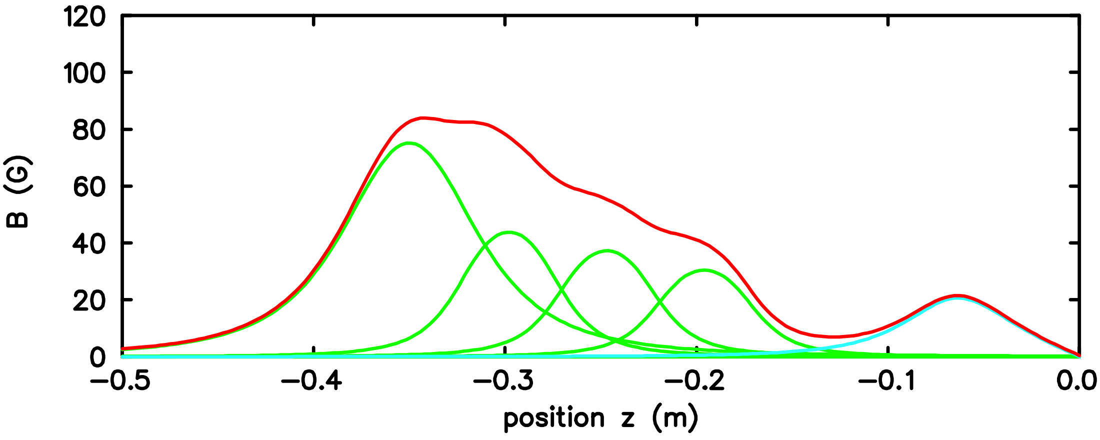

Figure 5.4: Magnetic field of the Zeeman slower vs. position on the beam axis (distance measured from the trap center)

The B-field calculation includes the field from the MOT coils at their 8 A operating current (see Sec. 5.4). This gradient field provides both confinement in the MOT and the last field gradient for Zeeman slowing. From the magnetic field and the detuning of the slowing laser of 50 MHZ from the cooling transition, it is possible to calculate the slowing forces and the corresponding velocity profile. For a detailed discussion of

Zeeman slowing and the calculations see [Eng97]; the result for our case is shown in Fig. 5.5. The figure displays a calculation of the slowing effect on the fastest atoms that can be captured, at a starting velocity of 140 m/s. It shows the slowing along the beam axis and the transversal spreading of the atom beam assuming zero initial transversal velocity. We see that the slowing force varies strongly along the beam path, which is a sign for mismatched magnetic fields. The original design currents for the Zeeman slowing coils give a better force profile and a higher maximum starting velocity [Mos99]; nevertheless, in our experiments the displayed configuration works best and gives, if the cesium dispensers are operated at 4 A, a MOT loading rate close to 10^8 atoms/s. In typical experiments, we turn down the dispenser current and load at only $\sim 10^7$ atoms/s, since the MOT atom number is not the limitation for experiments in the dipole trap.

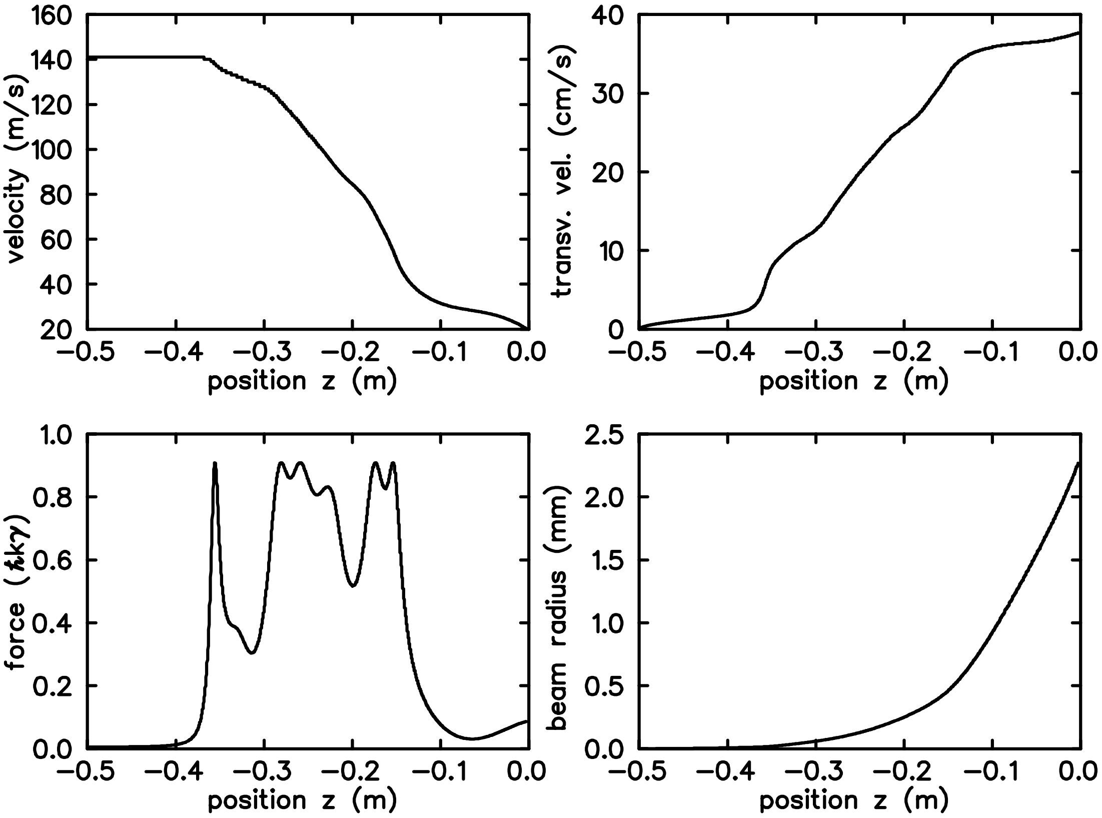

Figure 5.5: Simulation of the Zeeman slower's effect for an atom starting at 140 m/s. The x-axes display the distance from the trap center. From left to right, top to bottom: velocity along the beam axis, transversal velocity, slowing force (photon recoil × scattering rate), and beam radius.

5.3 Diode lasers

Several near-infrared laser wavelengths must be supplied to the experiment for implementation of the various loading and cooling steps. These are all resonant with the cesium D_2 line, operating on different hyperfine substates of the $6^2S_{1/2}$ and $6^2P_{3/2}$ levels (see Sec.2.1). The typical notation is ($F_1 \rightarrow F_2$), which signifies a laser resonant to the transition from the $6^2S_{1/2}, F = F_1$ state to $6^2P_{3/2}, F' = F_2$.

Six different near-resonant laser beams are necessary for operation of the experiment:

- MOT cooling laser, slightly red detuned from (4→5),
- Zeeman slowing beam, 50 MHz red detuned from (4→5),
- MOT repumper, on (3→3),
- pumping beam for Raman cooling, slightly blue detuned from (3→2),
- lattice laser for Raman cooling, on (4→4),
- absorption imaging beam, on (4→5).

The complete laser setup is described in [Mar03b] and is similar to the setup in the GOST experiment [Ham02a]. A frequency reference is obtained by the so-called "master laser", powered by a 852nm laser diode (SDL-5420) which is stabilized via a Littrow-type extended-cavity setup [Tha01]. It is frequency stabilized 160 MHz below the cesium (4→5) transition by modulation transfer spectroscopy [Raj79, Ber01] on a beam that passes through a double-pass 80 MHz acousto-optic modulator (AOM). The frequency width of the master laser is about 100 kHz with no significant long-term drift of its absolute frequency.

The MOT cooler, repumper and Zeeman slower beams are obtained from DBR (distributed Bragg reflector) laser diodes (SDL-5712-H1). These 100 mW laser diodes feature periodic layers of spatially varying index of refraction on the back side of the active laser area, which work as a wavelength-selective reflector and keep a line width of about 1 MHz without an external cavity.

The MOT cooler and Zeeman slower lasers are frequency stabilized by beat locks [Sch99] with the master laser. The beating signal between the each of these lasers and the master laser is detected on a fast photodiode. This signal is mixed down and compared to the frequency from a voltage-controlled oscillator (VCO) to obtain a dispersive error signal [Ham02a]. Changing the frequency of the VCO from 160 MHz allows to detune the laser from the (4→5) resonance with radio frequency precision. The tuning range is in the present setup limited by the VCO frequency range to between −90 MHz and +60 MHz. The MOT and the Zeeman slower laser are coupled into polarization maintaining single-mode optical fibers (OZ Optics PMJ-3A3-850-5 and Thorlabs FS-PM-4621, respectively) to transport the light to the experiment and provide 31 mW and 31.5 mW of optical power, respectively, at the fiber outputs.

The laser providing the repumper and optical pumping beams, which address transitions from the lower $F = 3$ hyperfine state, cannot be referenced to the master laser easily, as the frequency difference is ~9 GHz. It is frequency stabilized to a Cs absorption cell via a technique (published under the acronym DAVLL by the JILA group [Cor98]) that employs the Zeeman effect: In a magnetic field of ~130 G, the $\sigma+$ and $\sigma-$ components of a linearly polarized laser beam are shifted in opposite directions (circular dichroism). By detecting these components separately and subtracting the signals, a dispersion-like signal useful for locking is obtained. This scheme works on the Doppler broadened absorption line, thus having a very large capture range but also a small slope in the error signal, making it unsuitable for narrow-band looking. Also, it is sensitive to temperature variations in the spectroscopy cell, which has to be temperature stabilized to avoid frequency drifts of the laser. However, for the repumper we do not need RF precision frequency control, and it is fairly simple to set up and very robust once working properly. The laser is frequency locked in the middle between the (3→2) and (3→3) transitions, detuned 75 MHz from both.

From this laser, the resonant (3→3) repumping light is obtained by shifting the frequency by +75 MHz in an AOM. The light coming from the AOM is split into two parts which are combined with the MOT and repumper lasers by coupling into their respective optical fibers with orthogonal polarization. The repumper powers available at the fiber outputs are 2.1 mW for the MOT and 5 mW for the Zeeman slower. The optical pumping light for the Raman cooling scheme (see Sec. 6.2) is split off from the same laser beam but shifted in the opposite direction, by -66.5 MHz, to be 8.5 MHz blue detuned from the (3→2) transition. It is coupled into a separate optical fiber (OZ Optics PMJ-3A3-850-5) and delivers 130 µW at the output.

The optical lattice for Raman cooling is formed by the light from a separate diode laser. The laser diode (SDL-5420) is operated at 120 mW and frequency stabilized by injection locking [Sie86, Ger99]. A laser beam picked off from the master laser, which runs 160 MHz red-detuned from the (4→5) transition, is shifted by another -170 MHz through an AOM, which results in a frequency 80 MHz below the (4→4) transition. This beam is used to seed the lattice laser. By using an 80 MHz AOM to switch the lattice laser, the light arriving at the experiment is right on the (4→4) transition. After the AOM and a 30 µm pinhole to improve the beam quality, the power available at the experiment is 70 mW.

For imaging purposes, two probe laser beams are split off from the master laser. Each passes through a double-pass AOM at 80 MHZ used to shift their frequencies onto the (4→5) transition. The light is delivered to the experiment via optical fibers (Thorlabs FS-PM-4621). The power is very small and has not been measured exactly, it is adjusted to get proper exposure on the CCD cameras.

For turning on and off the lights by computer control, each laser beam except the Zeeman slower incorporates an AOM in its beam path. It is thus possible to switch the light and adjust the intensities with microsecond precision. Except for the two imaging lasers, additional mechanical shutters, which close a few milliseconds after the AOMs are powered down, prevent stray light from disturbing the experiments.

5.4 Magnetic fields

Magnetic fields are needed for several purposes: the magneto-optical trap needs a quadrupole field to operate, we want to tune the interaction between the Cs atoms via a homogeneous bias field, and we use a combination of both fields to magnetically levitate the atoms. The fields are supplied by two pairs of coils mounted on the outside of the vacuum chamber, as shown in Fig. 5.6.

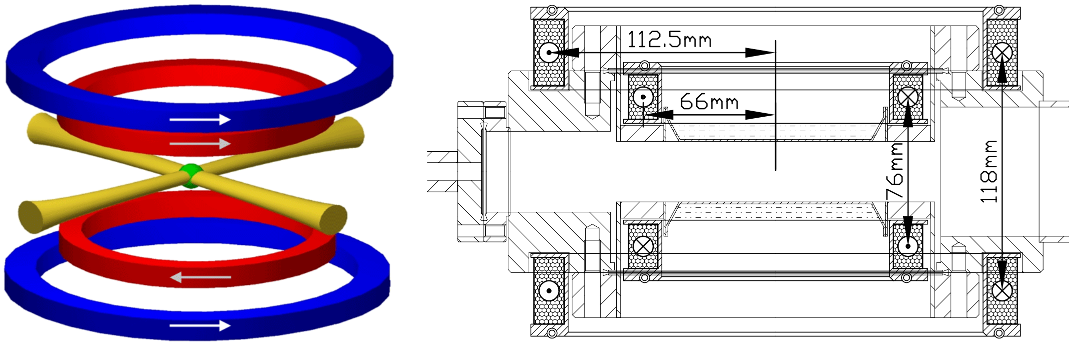

Figure 5.6: Magnetic field coil setup. Left: Schematic figure including the optical dipole trap. Right: Construction drawing with coil positioning on the vacuum chamber. The outer coils are set up in a Helmholtz configuration and provide a homogeneous bias field in the trap center. The inner coils, in Anti-Helmholtz configuration, generate the MOT quadrupole field and the levitation field gradient.

The outer pair of coils (bias coils) is connected in a way that the current flows in the same direction in both coils. The distance between the coils is nearly identical to the radius of one coil, therefore the configuration is very close to a pair of Helmholtz coils and gives a very homogeneous field in the center. The copper wire used has a rectangular cross-section of 1.25×2.75 mm^2, and each of the coils has a total of 143 windings. Every 24 windings (two layers of wire) have their own connector, so that we can individually address five sets of 24 windings each and one of 23 windings. The five 24-winding sets are connected in parallel to make a low inductance ($L \simeq 315$ μH) coil. A programmable power supply (Delta SM 30-100D) provides up to 100 A, generating a homogeneous bias field of up to 190 G. The power supply is operated in constant current mode, the current noise has an amplitude of approx. 6 mA (equiv. ~11 mG). This noise can be reduced by a factor of twenty by operating the supply in constant voltage mode; in the present experiments, however, the noise is no limitation and for technical reasons it is more convenient to use the constant current mode. The field is switched by a circuit [Win02] that sinks the induction current of the coils to allow for short switching times; in practice, the current can be turned off in 5 μs, but the magnetic field takes about 7 ms to drop to zero due to eddy currents in the vacuum chamber body. The time scale for switching on the current is limited by the voltage reserve of the power supply to 360 μs, the magnetic field is stable after 1.5 ms.

The inner pair of coils (gradient coils) is connected in an Anti-Helmholtz configuration. The current flows in opposite directions in the upper and lower coils, thus the field strength is zero in the trap center, growing linearly in each direction. The current directions are matched to the bias coils so that when both coil pairs are operated at the same time, they create a positive field gradient along the vertical z axis (field strength grows when going upwards). The coils are wound with the same wire as the bias coils, with a total 110 windings each organized two sets of 31, one of 48 windings. The two sets of 31 windings are connected in parallel and form the actual gradient coil used in the experiment (inductance $L \simeq 170\ \mu\text{H}$), the 48-winding set is free for future use. The gradient coils are powered by a similar power supply as the bias coils (Delta SM 45-70), and the same noise considerations apply. The currents are switched by an identical circuit as in the case of the bias coils, with on/off switching times of 120 µs/4 µs. The magnetic field total rise/fall times are 0.6 ms/1 ms. At a current of 37.7 A, the coils provide a vertical B field gradient of 31.3 G/cm as is necessary to compensate gravity for ground state cesium atoms (see Sec. 4.3). The maximum gradient possible with the present power supply, at a current of 70 A, is 58 G/cm.

Both coil pairs are mounted on aluminum supports that are slitted on one side to prevent eddy currents in the supports themselves. They are electrically insulated from the stainless steel vacuum chamber by plastics spacers. The heat produced by the coils is a total of 250 W at typical operating currents (40 A in the bias coils, 38 A in the gradient coils) or 1.1 kW at maximum currents. The heat is dissipated by water cooled 5 mm copper tubes integrated into the support structure (visible in the cross-section on the right side of Fig. 5.6). The cooling keeps the coil temperatures always below 50 °C at the standard operating currents. When the bias coils are operated above 80 A for extended periods of time, the temperature rises close to 100 °C, and tests have shown increased losses from the atom trap. The loss mechanism has not been further investigated, direct heating of the vacuum chamber can be excluded since the aluminum supports do not show an increase in temperature. Without further study, the maximum safe operating current for the bias coils is limited to 80 A, giving a maximum bias field of 150 G. The gradient coils are always operated at 38 A or below and have not been tested thoroughly at higher currents, but probably similar considerations apply.

Environmental B-field compensation

A laboratory environment features many devices that produce magnetic fields, both static and dynamic. The dynamic B-field noise, predominantly 50 Hz noise from power line transformers, would need some effort to compensate, as it requires dynamic B-field control. We have measured the noise to have an amplitude up to 15 mG close to the trap center depending on the equipment operated nearby. The single most notable noise source are the AC line cooling fans we use too cool electronics equipment. Repositioning of the fans reduced the noise amplitude to 3 mG. At this level, it is below the noise generated by current ripple in our power supplies and thus tolerable in current experiments.

The static magnetic fields at the trap center, however, are much larger. The largest sources of static fields, the earth's magnetic field and the stray field from our large 60 l/s ion getter pump, both have a strength of the order of 0.5 G. To countervail these fields, we have installed a set of compensation coils, shown in Fig. 5.7.

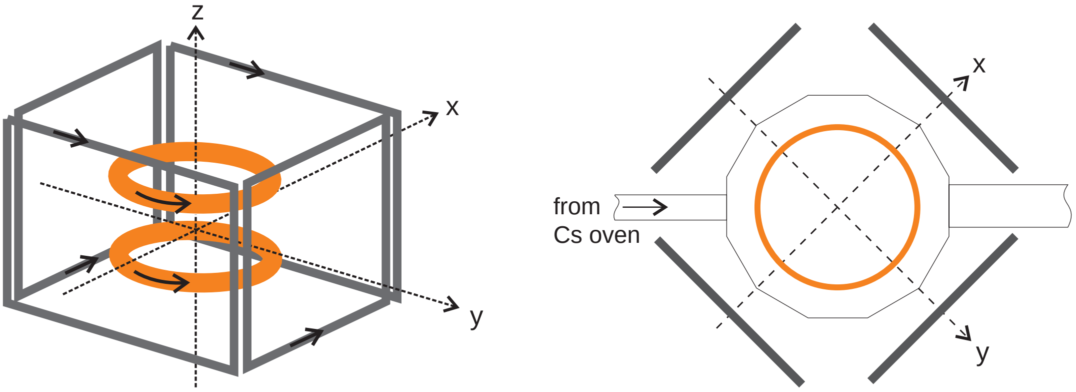

Figure 5.7: B-field compensation setup. Left: 3D view of the coil configuration. Right: Top view with vacuum chamber.

To be able to compensate magnetic fields in all spatial directions, three orthogonal sets of coils have been mounted around the trap. In the vertical direction, the spare 23-winding set of the bias coils is employed. For the horizontal axes (the orientation of the x and y axes relative to the vacuum chamber can be seen on the right in Fig. 5.7), two pairs of extra compensation coils were constructed. They are wound onto square supports of 50 cm side length, which are mounted directly onto the optical table at a distance of 40 cm from the trap center. At 70 windings for each single coil, a current of 2 A sent through a coil pair produces a field strength of 1 G in the trap center. The current for the horizontal compensation coils is provided by two highly precise power supplies (HighFinesse BCS 2/20) that are specified with a ripple below 10^{-4} and can be computer controlled to supply a current from -2 A to +2 A. In the vertical direction, a similar power supply (HighFinesse BCS 3/15) allows to send ±3 A through the 23-winding coil, giving a maximum field strength of 5.5 G. Altogether, the complete set of coils allows to apply a homogeneous field of up to 1 G at the trap center pointing into an arbitrary spatial direction.

5.5 CO$_2$ lasers

The workhorse of the experiment is the optical potential of two crossed CO$_2$-laser beams.

The 10.6 μm laser light is produced by two independent lasers (Coherent-DEOS GEM-100L), which are specified for an output power of 100 W cw each. The power level they typically deliver is 120-130 W. The laser heads are pumped by 1 kW of 100 MHz radio frequency power each. To minimize laser intensity noise, the RF drivers have been modified to receive their power from separate, highly stable DC power supplies (Agilent 6573A).

The laser head geometry and the active medium gas mixture are designed to allow laser operation only on one specified CO_2 emission line, with a total gain profile width of ~60 MHz. They run on a single longitudinal line and are fitted with a piezoelectrically mounted end mirror to allow for precise tuning of the laser frequency. This makes it possible to use the lasers for optical lattice formation, however in the present application we want no interference to occur between the lasers and actually employ frequency shifting AOMs to ensure that this is not the case (see below).

The laser heads are very sensitive to temperature fluctuations. A variation of the cooling water temperature by more than 0.15 °C invariantly leads to mode hopping, which is accompanied by strong laser intensity fluctuations and leads to almost complete loss of atoms from the dipole trap. As our cooling water supply shows peak-to-peak temperature fluctuations of 0.3 °C, this initially proved to be a problem. One solution would be to stabilize the lasers with the piezoelectric mirrors, which requires setting up a spectroscopy system to derive an error signal. This is possible and was tried in a test setup with an SF_6 spectroscopy cell, but is not necessary for our current purposes and requires some effort due to the special optics and detectors required for the far-infrared light.

The simpler solution we went for was to actively temperature stabilize the cooling water. For this purpose, we mounted a temperature sensor (Farnell 25 kΩ NTC resistor) into the water flow at each laser head's cooling water input. Immediately before the water flows into the laser, it is sent through a 150 mm long, 16.5 mm outer diameter aluminum tube that is wrapped in a flexible heating pad (Minco HK5172R220L12B Kapton heater). Connected to the 230 V AC power line, this pad supplies a maximum of 240 W of heating power, which is sufficient to heat the water by ~0.3 °C at a flow of 10 l/min. This is just enough to compensate the cooling water temperature fluctuations. The heater is regulated by a microprocessor temperature controller (Eurotherm 2500E/S/4LOOP/MODBUS) through a solid state relay. The time scale of the temperature control is approx. 1 s, we achieve in this way a short-term stability of ±0.01 °C. Residual long-term drifts over many hours are compensated by occasionally re-adjusting the offset voltage on the piezo mirrors to ensure the laser is running in the center of its gain profile.

For the CO_2 lasers to operate stably with minimum noise, they need to run continuously. Fast switching of the light is accomplished by inserting acousto-optic modulators into the beam path. Each of the laser heads includes an integrated output telescope providing a beam waist ($1/e^2$ radius) of 3 mm. This waist is optimized to match the aperture of the AOMs (IntraAction AGM-408BB1M) used to switch the laser light. The AOM aperture has a diameter of 8 mm; at a $1/e^2$ radius of 3 mm, 97.1% of the laser power is contained within this aperture. To focus the laser more strongly would exceed the laser power density the AOMs are specified for.

The AOM material is germanium, which has some small absorption at the 10.6 μm wavelength of the lasers. Additionally, the anti-reflective coating is not perfect, and together with some geometric cut-off the transmission through our AOMs is 88%. This measured optimum is the same for both AOMs and in perfect agreement with the specified total insertion loss of 12%. The driving electronics (IntraAction GE-4050) delivers up to 50 W of radio-frequency power at 40 MHz into the AOM. At maximum power, 90-92% of the transmitted laser power are deflected into the first order of diffraction. In total, about 80% of the power incident onto the AOM is delivered into the first order. The diffraction angle is 78 mrad, which at a distance of 30 cm gives a distance of 23 mm between 0th and 1st order and allows for easy separation of the beams. The 0th order light is dumped into a water-cooled beam trap.

We use the diffracted beam for the optical dipole trap. The AOMs allow fast on and off switching of this light, the total optical rise time is ~1 μs (manufacturer specification). They are adjusted to frequency shift one laser beam by +40 MHz, the other by -40 MHz; since the laser frequencies are within $<$ 60 MHz of each other, the light frequencies arriving at the trap are different by 20-140 MHz. This ensures that any interference patterns are modulated fast enough compared to the atom dynamics in the trap to be of no consequence. Therefore, we can simply add the potentials formed by the laser beams to calculate the total trap potential.

Even though they are water cooled, the 50 W of radio frequency power and several Watts of absorbed CO_2-laser power lead to strong thermal effects in the AOMs. The diffracted beam is astigmatic and moves with varying RF power. For this reason, the modulators are always operated at zero or full power; this ensures that the beams, when turned on, have a fixed position.

The CO_2-laser light coming from each of the AOMs is directed to the experiment chamber via three 50 mm diameter gold coated copper mirrors (Laser Beam Products SNICU50-10-00). It is then sent through a meniscus lens of 190.5 mm focal length (Laser Beam Products LZ38-7-190) to form a focus in the trap center. The strong astigmatism of the laser beams caused by the acousto-optic modulators leads to the focal point distance from the lens to differ by up to 85 mm when measured in the horizontal or vertical plane.

Figure 5.8 shows the measured beam waists of the two lasers after the focusing lenses. The lenses are both mounted at the optimum distance from the trap center to minimize the focus ellipticity, i.e. where the fit curves cross. This distance is 231 mm for Laser 1 (at this point, the beam waist in both horizontal and vertical directions is w_0 = 590 μm) and 230 mm for Laser 2 (w_0 = 640 μm). The lenses are mounted on 3D translation stages to allow for fine adjustment of the focus positions.

The power of the laser beams after passing through all optical elements is estimated to 85 ± 5 W at the trap center. Because of space limitations, we cannot measure the power after passing through the vacuum chamber. The test setup used to obtain the beam waist data, however, was composed of the same number of optical elements at roughly the same beam path length. From the power measured there we subtract the previously measured transmission loss of one ZnSe UHV viewport, which amounts to

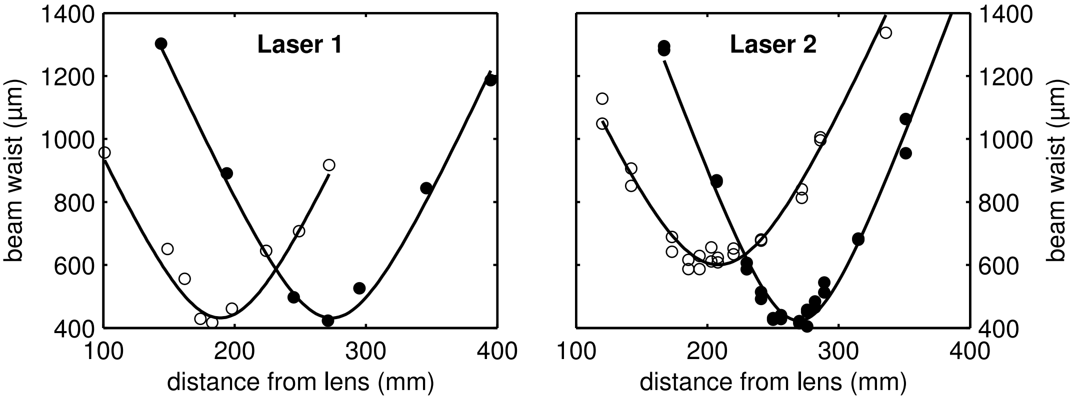

Figure 5.8: Beam waists of the CO_2-laser beams after the $f = 190.5$ mm focusing lenses measured in the horizontal (open symbols) and vertical (solid symbols) directions. The lines show least-squares fits of Gaussian beam propagation.

$\lesssim 2\%$. The CO_2 lasers display a slow output power drift of a few percent, which is included in the ±5 W error estimate.

5.6 Experiment control

Many processes on the atomic scale happen in a matter of microseconds or milliseconds. In an ultracold, low density ensemble, however, interaction dynamics can become extremely slow, taking place in a time scale of minutes. All of these processes have to be precisely controlled and, in measurements, the time scales need to be well-known to obtain exact data.

Combining the wide range of time scales from microsecond to minutes requires some effort. Quite commonly, slow control is handled by one device, such as software timing on a personal computer, which then triggers extremely precise timing boards to control fast processes. These fast timing boards are often “dumb” buffered devices, which, if operating on microsecond timing cycles, are limited by on-board memory to a burst of pulses that cannot last longer than on the order of a second. This combination of techniques is not very flexible and often lacking in ultimate real-time performance.

We have chosen an integrated solution that allows microsecond precision control of the experiment while at the same time working self-sufficiently for many minutes. The central element is a real-time control and measurement system (Keithley ADwin-Gold with option ADwin-Gold-DA) which incorporates a dedicated digital signal processor (Analog Devices SHARC ADSP21062, 40 MHz) with 4 MB of on-board memory. The system is running a real-time operating system and features integrated timers which can be programmed at a resolution down to 25 ns. Our version of the ADwin system includes 32 TTL-compatible digital I/O channels, 2×8 multiplexed 100 kHz (10 µs settling time) 16-bit analog inputs, and 8 independent 16-bit analog outputs with a

±10 V output range and 10 μs full-range settling time.

Custom automation programs written in a proprietary BASIC dialect with real-time extensions (ADbasic) can be downloaded onto the system. The event-driven programs are triggered by the system timers, but although these can be set to fire as quickly as every 25 ns, even short program sequences take several microseconds to execute. Therefore, we have set the timing interval to 10 μs, which allows to reliably and reproducibly program I/O operations and is matched to the settling time of the analog channels. The program used to control the experiment is a simple self-written scheduler that takes a timing table as input and sets the outputs accordingly. It is downloaded, fed with data and started from a personal computer and then runs for a full experiment cycle completely independent on the ADwin system. The significant advantage over a simple buffered I/O card is that the timing table is organized in a flexible way so that the program can output a burst of fast timing pulses and then wait for minutes without wasting memory. The advantage over doing the control directly from a personal computer is that the timing is always precise down to below 1 μs, independent of the load of the host computer.

As mentioned above, the timing interval, which is the shortest time between two separate output changing operations, is set to 10 μs. However, the precision is higher than that: The timer event is generated with a jitter of below 100 ns. Upon event generation, the scheduler program looks up all output operations planned for this time step. Operations scheduled for the digital output channels 0-15 are then performed simultaneously. About 0.5 μs later, operations on channels 16-31 become effective. The time differences between event generation, the setting of channels 0-15 and of channels 16-31 are well-defined, so that a 90 μs pulse on one digital output channel will last exactly 90.0 ±0.1 μs, with all pulse edges on the first 16 channels completely simultaneous, the edges on channels 15-31 consistently delayed by ~0.5 μs. The analog channel timings are a little less well-defined, they are set individually after the digital outputs in ~1 μs time intervals and then need up to 10 μs to settle on their intended value. Currently, none of the analog inputs are in use, therefore data acquisition is not implemented in the program.

The front end to the scheduling program is a graphical user interface designed in LabVIEW (National Instruments LabVIEW 6.1). It integrates analog and digital output channels in a single tabular front panel. Standard delay times for digital outputs, e.g. shutter lag times, can be set in a separate table and are applied to the times entered. Scaling of analog outputs is also handled from a central conversion table, for example the magnetic bias field can be entered as a field strength value in Gauss and is automatically converted into the proper voltage to control the power supply. A set of variables can be used instead of fixed values for timings and analog values. The program allows to change these variables systematically from one experimental cycle to the next. A nested loop logic enables complex procedures to be carried out automatically, for example a lifetime measurement in the trap with time-of-flight temperature measurements at each trap holding time. The variable values for each experiment run are saved to disk.

Imaging system

We use four CCD cameras to observe the atoms in the experiment. Two small video ”finger cameras“ (Conrad Elektronik) show fluorescence images of the MOT on video screens and are used for monitoring and adjustment purposes. One triggerable slow-scan frame transfer CCD camera system (Theta System SIS-99/PH, 1024×1024 pixels, 14 bit resolution) offers low-noise imaging at high resolution, and a triggerable progressive-scan frame transfer video camera (Hitachi KP-F2A) allows to take precisely timed pictures from a second perspective. The slow-scan camera system includes a proprietary frame grabber and a separate computer system, while the triggerable video camera is connected to the control computer via a standard monochrome frame grabber board (MATRIX Vision MVtitan-G1). Both are controlled by self-written LabVIEW programs.

The exposure is timed for both cameras by trigger signals from the ADwin board. The electronic shutters allow for very short exposure timings. In the slow-scan camera, the frame transfer takes about 0.5 ms both at the beginning and the end of the exposure. Light hitting the CCD active area during this time will be smeared out over the image, which has to be taken into account for the timing and limits the minimum exposure time depending on the lighting situation. The read-out into the computer needs about 600 ms. Including some image analysis, the typical minimum period between individual pictures is not much less than about one second. A framing mode, where the charge on the chip is only moved for a partial frame to allow multiple exposures onto the active area within a short time, is currently not supported.

In the triggered video camera, the frame transfer is much faster and takes less than 100 μs, easily allowing for sub-ms exposures. Image readout is done in about 30 ms, the camera is able to take moving images at 30 fps. The CCD chip is actually a bit more sensitive to 852 nm light than the slow-scan camera, but due to the large readout noise the signal-to-noise ratio is much worse.

After exposure, the LabVIEW program automatically reads the image into the computer memory and displays it. In absorption imaging mode, two consecutive pictures are divided by each other and the result is shown instead of the individual images. The pictures are immediately processed by a MATLAB (The MathWorks MATLAB 6.5 R13) procedure that uses Gaussian fits to the atom cloud to calculate position, size and atom number. The operator can set up the program to save for each image only the data obtained from the fit or also the image itself. The saved data are logically connected to the experiment settings stored by the control program to enable automated data analysis, e.g. calculation of the sample temperature from a time-of-flight measurement series.

Usually, only one camera is used at the same time since the absorption imaging we employ in most measurements is destructive. The slow-scan camera, which we use most of the time, looks into the vacuum chamber from the side, at a 90° angle to the atomic beam (top viewport on the left side of Fig. 5.3). The focusing optics consists of a 40 mm diameter, $f = 200$ mm achromatic doublet (Linos Photonics 322293 NIR-

ARB2) shortly behind the UHV viewport at a distance of 200 mm from the trap center and a 50 mm diameter, $f = 250$ mm achromat (Thorlabs LAC376-B) that focuses the light onto the CCD chip. The diffraction limited resolution of this lens setup is calculated to 5 μm, the pixel size is 6 μm (cf. Sec. 6.6). Correspondingly, the full field of view covers about 6 mm in each direction. The triggered video camera looks into the vacuum chamber from above at a slight angle from the vertical direction. The imaging lenses are not permanently fixed, currently a 2/3 reducing optics of two achromatic lenses delivers a field of view of about 6 mm at a pixel size of 11.1 μm. Both CCD cameras together give full spatial information on the atom distribution in the trap at any given time.

Chapter 6

Trap properties and experimental procedures

In this chapter, I will explain the properties of the various potentials we use to trap ultracold cesium atoms and give some details on how the experiment is performed. Various steps lead us towards our goal of achieving quantum degeneracy in ^{133}Cs. The last section explains the imaging and temperature measurement procedure.

6.1 The MOT

The basic technical setup of the magneto-optical trap and the Zeeman slower has been described in Ch. 5. For Zeeman slowing, 31.5 mW of light detuned typically 50 MHz below the cooling transition is available, together with about 5 mW of repumping power. At the output of the optical fiber, the light is first circularly polarized by a quarter wave plate and then expanded via a telescope to a beam of a diameter of roughly 5 cm. The beam enters the vacuum system through a viewport on the far end of the large ion getter pump (on the very right in Fig. 5.1), at a distance of 142 cm from the cesium oven. It is focused onto the nozzle of the oven. In the MOT region, at a distance of 76 cm from the viewport, the beam waist is approximately 1.2 cm and the central intensity about 14 mW/cm^2.

The MOT light, at a total power of 31 mW slightly red-detuned by a computer-controlled amount from the cooling transition plus 2.1 mW of repumping light, is split into five single beams. Four of those enter the vacuum chamber horizontally, the fifth enters from below at an angle slightly deviating from the vertical direction and is retro-reflected. The beams are expanded to a beam waist of about 1 cm, resulting in an intensity of about 4 mW/cm^2. The configuration of the MOT beams is shown in Fig. 6.1.

The MOT is operated at a detuning of 4.5 MHz for loading, with a quadrupole field gradient of 7.8 G/cm. The loading rate from the Zeeman-slowed beam is up to $5 \cdot 10^7$ s^{-1}, with maximum observed atom numbers in the MOT of $3 \cdot 10^8$. Typically, the

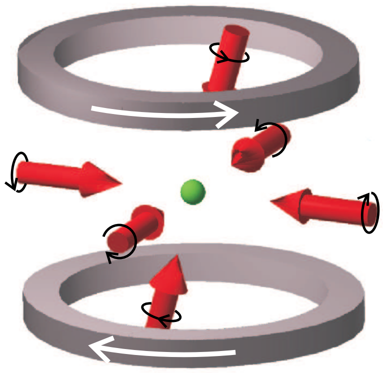

Figure 6.1: Configuration of the MOT light beams. The black circular arrows indicate the circular polarization orientation of the individual MOT beams, the white arrows the current direction the quadrupole coils.

MOT is operated at a lower atom flux to minimize the consumption of cesium from the dispensers, and the atom number after 4 s of loading is around $3 \cdot 10^7$. The measured $1/e$ lifetime of the trapped atoms in the MOT is 200 s. After a molasses phase of 5 ms with the cooling laser detuned 90 MHz below resonance, the temperature is 10 μK.

6.2 Raman sideband cooling

In the levitated optical dipole potential, we trap ^{133}Cs in its lowest internal state, $6^2\mathrm{S}_{1/2}, F = 3, m_F = 3$. When the cesium atoms are captured in the MOT and precooled in a molasses, they end up in a mixture of states and have to be spin polarized. This can typically be done by optical pumping, however this process induces some heating due to the scattering of several photons in the pumping process. A better alternative is Raman sideband cooling, which can be utilized to simultaneously cool and polarize the atoms.

A schematic overview of the principle of degenerate Raman sideband cooling is shown in Fig. 6.2. In our experiment, we follow the scheme described in [Ker00, Tre01]. The atoms are captured in a 3D optical lattice formed by four laser beams resonant with the $6^2\mathrm{S}_{1/2}, F = 4 \rightarrow 6^2\mathrm{P}_{3/2}, F' = 4$ transition, which is detuned by 9.2 GHz from resonance for atoms in the $F = 3$ lower hyperfine state. Besides generating the trapping potential, the laser light provides Raman coupling of degenerate energy levels. A magnetic offset field is applied and its strength adjusted so that the Zeeman splitting between levels with $\Delta m_F = 1$ exactly matches the spacing of the vibrational energy levels in the lattice potential. Thus, a state with vibrational quantum number ν in the external potential and magnetic quantum number m_F is coupled to a state $\nu - 1$ with magnetic quantum number $m_F - 1$. A mainly σ^+ polarized laser beam, 8.5 MHz blue detuned from the $6^2\mathrm{S}_{1/2}, F = 3 \rightarrow 6^2\mathrm{P}_{3/2}, F' = 2$ transition, provides optical pumping from a state $F = 3, m_F = m_{F,0}$ to $F = 3, m_F = m_{F,0} + 1$. In the Lamb-

Dicke regime, the optical pumping process normally preserves ν, so eventually the atoms will end up in the state $\nu = 0, m_F = 2$, which is a dark state for the σ^+ polarized light. From this state they are pumped into the $\nu = 0, m_F = 3$ absolute ground state by a weak π polarization component of the pumping light. The slow pumping in the last cooling stage suppresses reabsorption heating [Cas98]. After the optical cooling in the lattice, the potential is ramped down within several ten microseconds to adiabatically release the ensemble and thus minimize the free-space temperature [Kas95].

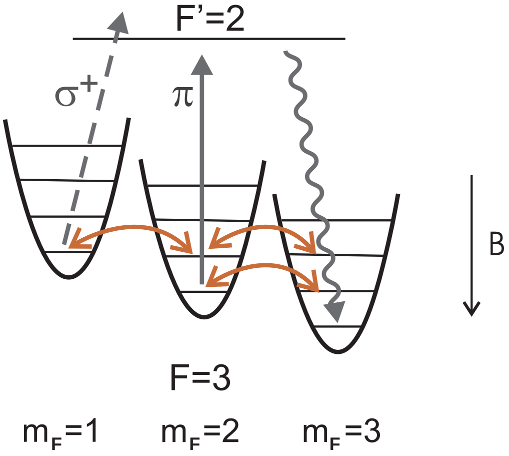

Figure 6.2: Raman sideband cooling scheme (see text).

The geometry of our Raman cooling setup is derived from [Tre01]. Four linearly polarized laser beams at a total power of 70 mW and $1/e^2$ beam diameters of 1 mm form the optical lattice, the four-beam geometry ensures the stability of the lattice potential under phase fluctuations of the laser light [Gry93]. A rough estimate of the lattice potential strength, not taking into account the exact polarizations of the individual beams, gives an estimation for the vibration frequency of the order of 140 kHz. This frequency is equivalent to a spacing of the vibrational levels of $\hbar\omega \approx k_B \cdot 6$ µK. The matching magnetic field strength to provide a Zeeman splitting of the same amount between neighboring m_F sublevels results to 400 mG.

Experimentally, we optimize the cooling process by adjusting the magnetic field strength and direction while monitoring the number of atoms captured in the lattice and their temperature. When the cooling is inefficient, i.e. the atoms are not rapidly pumped into a dark state, photon scattering will heat the atoms and lead to strong loss from the lattice. Thus, maximizing the number of captured atoms will optimize the cooling cycle. Not only the magnetic field strength, but also the direction of the field is varied via the compensation coils. This compensates for imperfections in the σ^+ pumping laser polarization and at the same time provides the weak π component necessary to depopulate the $\nu = 0, F = 3, m_F = 2$ state. The magnetic field strength where the cooling process works optimally is found to be about 220 mG. This value is in good agreement with the calculation of 400 mG within the systematic uncertainty of both values, each of which we cannot determine to better than within a factor of two.

The result of the Raman sideband cooling process is quite satisfactory for our purposes. Within 8 ms, about 95% of the atoms are polarized into the desired $F = 3, m_F = 3$ state at a temperature of around 1 μK. We have cooled and polarized up to $3 \cdot 10^7$ atoms in our setup; higher atom numbers are not collected in the relatively small lattice for geometric reasons. The original publication [Tre01] cites temperatures down to 200 nK, which we have not achieved. The reasons for this are not clear, but may have to do with the much stronger lattice potential in our case (140 kHz vibration frequency as compared to 21 kHz). However, the Raman cooling process is only one step in loading our levitated optical dipole trap, and the temperature is not a limiting factor here due to the strong heating in the transfer into the LevT (Sec. 6.4).

6.3 The LevT

The LevT (*Lev*itated *T*rap) is the main trap around which the various experiments are carried out. It consists of a quasi-electrostatic optical dipole trap combined with magnetic levitation to cancel the influence of the gravitational forces.

6.3.1 Optical potential

The CO_2-laser setup provides two crossed beams at a power of 85 W each at a wavelength of 10.6 μm. The optical dipole potential is proportional to the light intensity, which in the laser beams has a Gaussian profile

$$I(r, a) = \frac{2P}{\pi w^2(a)} e^{-2r^2/w^2(a)}, \tag{6.1}$$

where P is the total laser power, a the axial coordinate along the beam axis, and r the radial coordinate. The position-dependent beam waist $w(a)$ follows the relation

$$w(a) = w_0 \sqrt{1 + \left(\frac{a}{z_R}\right)^2}. \tag{6.2}$$

Here, w_0 denotes the minimum beam waist in the focus, the *Rayleigh range* $z_R = \pi w_0^2/\lambda$ is a measure of the axial extension of the focal region.

The CO_2-laser beams are weakly focused to a minimum beam waist of $w_0 \simeq 400$ μm, with a corresponding Rayleigh range of $z_R \simeq 5$ cm (cf. Sec. 5.5, esp. Fig. 5.8). The laser beams cross a little below 1 z_R off-focus, where the slope $\partial w/\partial a \lesssim w'(z_R) = w_0/(z_R\sqrt{2}) \approx 5.6 \cdot 10^{-3}$. Since this variation is weak, we do not include it explicitly into the potential shape calculations and assume $w(a) = const$; however, through the uncertainty of the beam crossing position of ~3 mm, it leads to an error estimate of ~15 μm in the beam waists. The values for Laser 1 and Laser 2 are $w_1 \equiv w_y = 590 \pm 15$ μm and $w_2 \equiv w_x = 640 \pm 15$ μm, respectively. The laser beams both run in the horizontal plane and cross at right angles. We define a coordinate system where Laser 2 propagates along the x-axis, Laser 1 along the y-axis, and the z-axis is oriented vertically pointing upwards. The axis orientations relative to the experiment chamber are consistent with the compensation coil setup (Sec. 5.4, Fig. 5.7), see also Fig. 8.2. Note that this (for historical reasons) is a left-handed coordinate system; when we do calculations of the potential shapes, the orientiation of the y-axis is reversed, with the axis pointing in the opposite direction of the propagation of Laser 1.

As we have taken care to avoid interference effects between the CO_2 lasers by maintaining a large frequency difference (see Sec. 5.5), the total optical potential is just the sum of the potentials of the single lasers,

$$U_{\mathrm{CO_2}}(x,y,z) = -\hat{U}_1 e^{-2(x^2+z^2)/w_1^2} - \hat{U}_2 e^{-2(y^2+z^2)/w_2^2}, \tag{6.3}$$

with the individual trap depths (Eqs. 6.1, 4.16)

$$\hat{U}_{1,2} = \frac{\alpha_{\mathrm{stat}}}{\pi\epsilon_0 c}\frac{P_{1,2}}{w_{1,2}^2} = k_B \cdot 5.76 \cdot 10^4\ \mu\mathrm{K} \cdot \frac{P_{1,2}/\mathrm{W}}{w_{1,2}^2/\mu\mathrm{m}^2}. \tag{6.4}$$

The resulting trap depths are $\hat{U}_1 = k_B \cdot (14.1 \pm 1.1)\ \mu\mathrm{K}$ and $\hat{U}_2 = k_B \cdot (11.9 \pm 0.9)\ \mu\mathrm{K}$. The sum $\hat{U}_1 + \hat{U}_2 = k_B \cdot 26\ \mu\mathrm{K}$ is the potential in the trap center. However, the effective trap depth is the lower of the two individual potential depths, since if the atoms escape into a single beam, they experience no restoring force to the trap center and are lost.

If the thermal energy of the trapped ensemble is much smaller than the potential depth, the Gaussian potential shape $U(r) = \hat{U}\exp(-2r^2/w^2)$ can be approximated as a radially symmetric harmonic oscillator,

$$U(r) \approx -\hat{U}\left(1 - 2\frac{r^2}{w^2}\right). \tag{6.5}$$

For the combined potential of the two lasers, the three-dimensional harmonic potential is

$$U_{\mathrm{harm}}(x,y,z) \;=\; -\left(\hat{U}_1 + \hat{U}_2\right) + 2\frac{\hat{U}_1}{w_1^2}x^2 + 2\frac{\hat{U}_2}{w_2^2}y^2 + 2\left(\frac{\hat{U}_1}{w_1^2} + \frac{\hat{U}_2}{w_2^2}\right)z^2, \tag{6.6}$$

and the trap oscillation frequencies result as $\omega_x/2\pi = 16.0 \pm 0.9\ \mathrm{Hz}, \omega_y/2\pi = 13.6 \pm 0.8\ \mathrm{Hz}, \omega_z/2\pi = 21.0 \pm 1.2\ \mathrm{Hz}$. We have performed measurements of the actual trap frequencies in the trap by exciting oscillations of the atomic ensemble and monitoring its movement [Mar03b]. The results are $\omega_x/2\pi = 14.9 \pm 0.8\ \mathrm{Hz}, \omega_y/2\pi = 11.6 \pm 0.6\ \mathrm{Hz}, \omega_z/2\pi = 17.7 \pm 0.3\ \mathrm{Hz}$, which is systematically lower than the result of the calculation. Since the measurement is quite direct and thus should expose no significant systematic error, we assume a deviation of the real potential shape from the measured CO_2-laser beam profiles, maybe caused by some distortion of the beam by the UHV viewports. For calculations of average ensemble properties, like the density or phase-space density, we use the geometric average $\bar{\omega}$ of the trap frequencies

$\bar{\omega} = \sqrt[3]{\omega_x \omega_y \omega_z}$. The result from the calculated parameters is $\bar{\omega}/2\pi = 16.6 \pm 0.6$ Hz, from the measurements we get $\bar{\omega}/2\pi = 14.5 \pm 0.5$ Hz, which is the value used in further calculations.

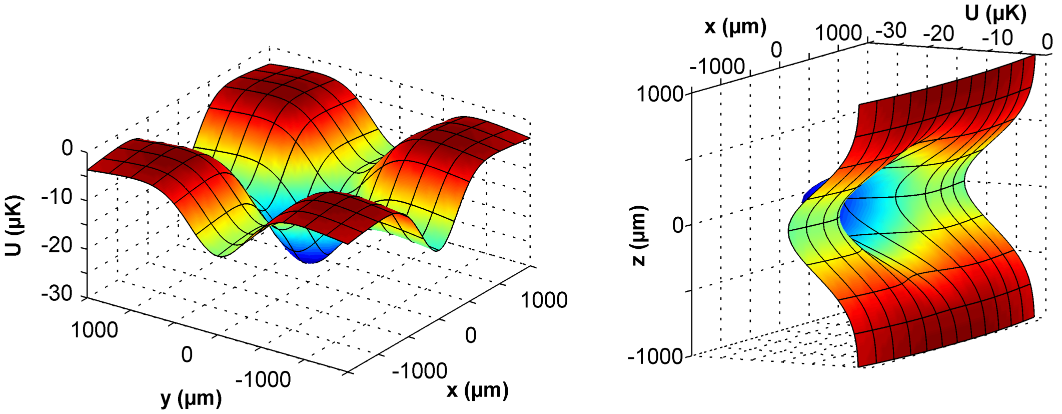

Figure 6.3: Potential of the CO_2-laser trap in the horizontal x-y plane at $z = 0$ (left) and in the vertical x-z plane at $y = 0$ (right). The calculation includes the transversal magnetic forces of the levitation field at a bias field of $B_{\text{bias}} = 75$ G (see text).

6.3.2 Magnetic levitation

Up to now, we have not considered the gravitational force mg, which causes a vertical potential gradient of 157 μK/mm. This is much stronger than the maximum gradient of the optical potential, and would lead to immediate loss from the trap. We use a magnetic force to compensate gravity. The required vertical field strength gradient for levitation of cesium $F = 3, m_F = 3$ ground state atoms is $\partial B/\partial z = (4/3)mg/\mu_B = 31.3$ G/cm (Sec. 4.3). Because of Maxwell's equation div$\boldsymbol{B} = 0$, the vertical field gradient leads to horizontal gradients $\partial B_x/\partial x = \partial B_y/\partial y = (2/3)mg/\mu_B$ in the case of cylindrical symmetry. These cause an outward pointing force acting on the trapped atoms.

We create the gradient field by combining a quadrupole field $\boldsymbol{B}_{\text{grad}}$ and a homogeneous bias field $\boldsymbol{B}_{\text{bias}}$ (Sec. 5.4). For symmetry reasons, at $z = 0$ the quadrupole field vector lies in the x-y plane and points radially outward from the trap center. The field strength is $B_{\text{grad}}(\rho) = (2/3)mg\rho/\mu_B$, with ρ being the radial coordinate. Since $\boldsymbol{B}_{\text{grad}}$ is in that plane perpendicular to the vertical bias field $\boldsymbol{B}_{\text{bias}}$, the strength of the combined field can be calculated as

$$\begin{aligned} B(\rho) &= \sqrt{B_{\text{bias}}^2 + \left(\frac{2mg\rho}{3\mu_B}\right)^2} \\ &\approx B_{\text{bias}}\left[1 + \frac{1}{2}\left(\frac{2mg\rho}{3\mu_B B_{\text{bias}}}\right)^2\right] \\ &= B_{\text{bias}} + \frac{2}{9}\frac{m^2g^2\rho^2}{\mu_B^2 B_{\text{bias}}}, \end{aligned} \tag{6.7}$$

with a corresponding potential

$$\begin{aligned} U_B(\rho) &= -\frac{3}{4}\mu_B B(\rho) = -\frac{3}{4}\mu_B B_{\text{bias}} - \frac{1}{6}\frac{m^2g^2}{\mu_B B_{\text{bias}}}\rho^2 \\ &= U_{B_{\text{bias}}} - \frac{1}{2}m\alpha^2\rho^2, \qquad \alpha = g\sqrt{\frac{m}{3\mu_B B_{\text{bias}}}} \end{aligned} \tag{6.8}$$

which is the inverse of a harmonic potential with trapping frequency α.

When the levitation field is turned on, in the vertical direction gravity and the magnetic force cancel exactly for the $F = 3, m_F = 3$ state, leaving only the optical potential. In the horizontal directions, the field gradients create an outward, anti-trapping potential with a slight curvature which depends on the bias field. The effect is shown in Fig. 6.4 for two different bias fields. The horizontal potential cross-sections are taken along the y-axis, and show the strong perturbation of the optical potential by the magnetic forces at low bias fields.

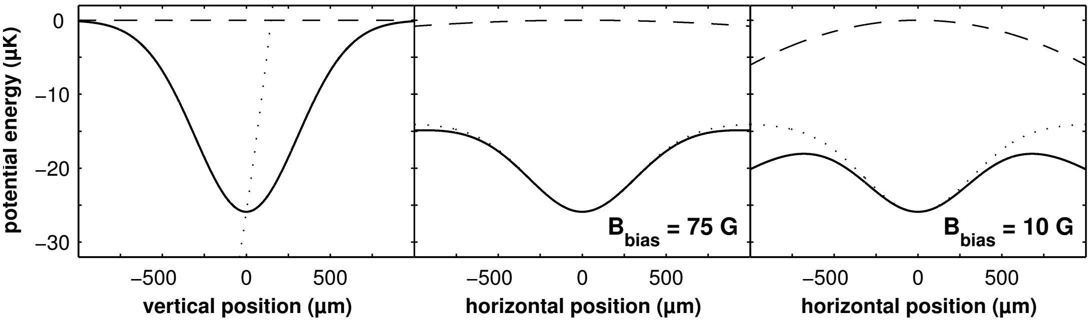

Figure 6.4: LevT potential (solid lines) in the vertical direction (left) and along one of the CO_2-laser beams (center,right) at different bias fields. The dashed lines represent the potential of the magnetic levitation field alone, the dotted lines the optical potential alone. At the 10 G bias field, the trap depth in the horizontal direction is reduced by 35% through the transversal magnetic forces.

Quantitatively, the potential depth of the combined trap can be calculated numerically for a range of bias fields by evaluating the potential profile along the weakest

(y) trap axis and calculating the difference between potential minimum and maximum. For the trap frequencies, one simply adds the optical and magnetic potential, e.g. in the x-axis we get

$$U_x = 2\frac{\hat{U}_1}{w_1^2}x^2 - \frac{1}{2}m\alpha^2x^2 = \frac{1}{2}m\left(\omega_x^2 - \alpha^2\right), \tag{6.9}$$

which immediately gives an expression for the trap frequencies in the horizontal axes

$$\omega'_{x,y} = \sqrt{\omega_{x,y}{}^2 - \alpha^2}. \tag{6.10}$$

The vertical trap frequency is unchanged by the levitation field.

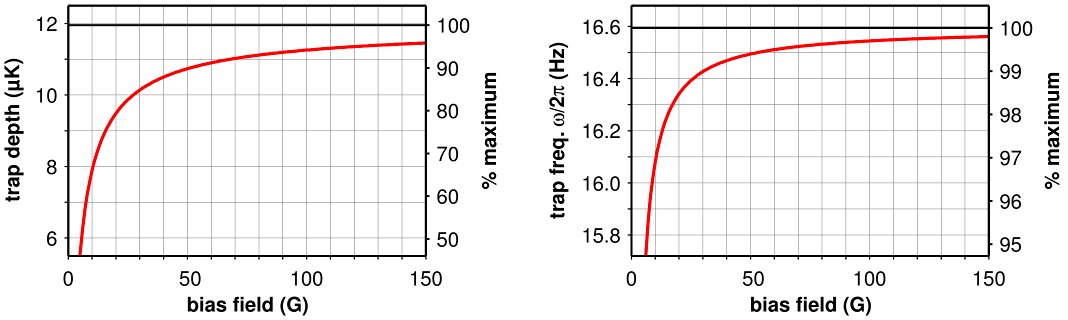

Figure 6.5: Calculated LevT trap depth and average trap frequency as a function of the bias field. The percentage scales differ by a factor of 10. At 75 G, the trap depth is 11.1 μK (93% of the maximum), the average trap frequency $\bar{\omega}/2\pi = 16.5$ Hz (>99%).

In Fig. 6.5, both the trap depth and the geometrically averaged trap frequency are plotted as a function of the bias field. The trap depth is reduced appreciably by the magnetic forces, even at the maximum field of 150 G the trap depth reduction values around 5%. However, the average trap frequency, which is the more important parameter since it enters to the third power into calculations of the particle density, is affected weakly, staying above 97% of the maximum down to 10 G. The graph does not take into account the deviation of the measured from the calculated trap frequencies, however the relative changes will be equivalent.

6.4 Loading the LevT & plain evaporation

To load the levitated trap, we simply turn on the CO_2-laser potential and simultaneously ramp up the magnetic levitation field within about 500 μs immediately after Raman cooling. The procedure is optimized by geometrically overlapping the positions of the two CO_2-laser beams with the cloud released from the optical lattice. This is done by imaging the positions on CCD cameras, which is possible because once the CO_2-laser beams are close to the atom cloud, they lead to a local increase in density

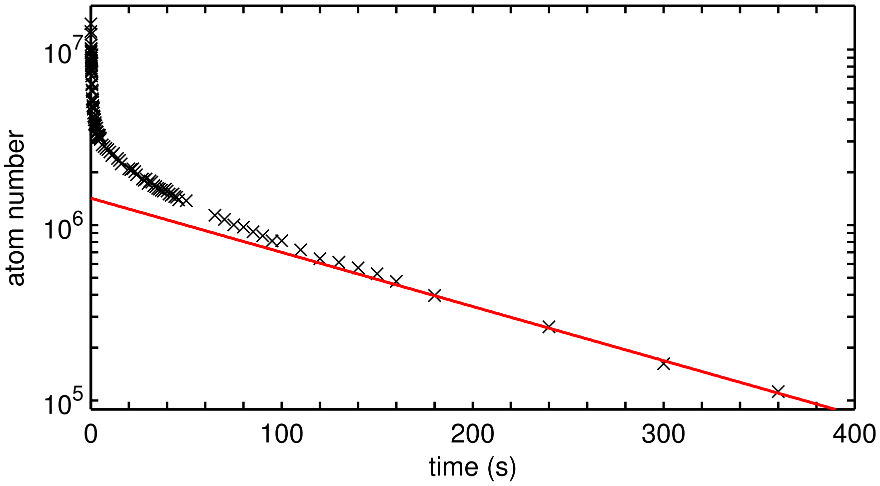

Figure 6.6: Evolution of the number of atoms of a trapped sample in the LevT at 75 G bias field. The solid line shows a simple exponential fit to the atom number taking into account only the data points taken after more than three minutes, which gives a $1/e$ lifetime of 140 s. Later measurements (Sec. 7.3) result in a more accurate value of the background gas limited $1/e$ lifetime of 180 s.

which shows up in absorption images. With one camera looking from the side and one looking from above, we have full spatial information and can adjust by sight. Since the length scales in our weakly focused trapping potential are on the order of hundreds of microns and can be easily resolved by the imaging system, this procedure is very precise. When the geometric optimization is done carefully, a subsequent optimization for the number of atoms captured in the trap results in no further improvement.

Figure 6.6 shows the evolution of the number of atoms in the levitated trap. About $2 \cdot 10^7$ polarized atoms at a temperature of 1 μK are provided by Raman cooling. Since in the levitation field atoms that are not captured in the trap do not fall out of the field of view, it takes about 100 ms for the trapped atoms to become clearly distinct from the expanding non-trapped fraction. At this time, $1.4 \cdot 10^7$ trapped atoms are visible. The atom number drops very steeply in the beginning, with only $1.0 \cdot 10^7$ atoms visible after 200 ms. In the figure we see this extremely steep drop within the first ten seconds, a somewhat slower decay up to 150 s, and after that a decay curve that within the resolution of this data looks like a simple exponential.

The simple exponential decay on a long time scale is what we expect from losses through background gas collisions at a vacuum system pressure in the 10^{-11} mbar range. The non-exponential decay between 10 s and 150 s can be explained by three-body recombination, which will be treated in Chapter 7. However, the very quick initial loss of almost one order of magnitude in atom number needs a closer look.

The temperature evolution helps to understand the process. In Fig. 6.7, we see in the left diagram an expanded view of the first 20 s of the atom number measurement.

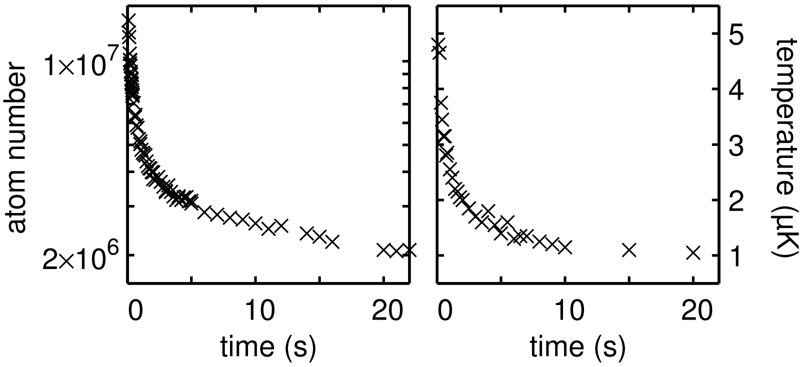

Figure 6.7: The first 20 s in the life of the LevT.

On the right, the corresponding temperatures as measured by time-of-flight imaging are shown. We see that corresponding to the strongest atom loss, the temperature drops from 5 µK at $t = 100$ ms to about 1 µK at 10 s. Later, the temperature stays roughly constant, measurements even after 180 s show no significant drop below 1 µK.

Obviously, within the first 100 ms the atoms are strongly heated from the initial 1 µK to around or above 5 µK. The reason is clear when we look at the spatial extension of the raman-cooled cloud, which has a $1/e$ radius of approximately 500 µm (in the vertical axis). An equilibrium distribution in our trap would at 1 µK only have a vertical $1/e$ radius of 100 µm. In the horizontal axes the relations are similar. Due to this mismatch, when the CO_2-laser trap is turned on nonadiabatically, the ensemble gains much potential energy which is in turn converted into kinetic energy and through collisions into temperature. Subsequently, the hot atoms evaporate out of the trap. This plain evaporation out of an optical dipole trap has been thoroughly studied [Eng00b], and the temperature drop to about $1/10$ of the trap depth meets the expectations. Thus, the initial fast drop in atom number from $2 \cdot 10^7$ to about $3 \cdot 10^6$ within 10 s can be attributed to plain evaporation. In all further experiments in the trap, the end of these initial 10 s of plain evaporation has been taken as a starting point. Depending on the loading time in the MOT and the fine adjustment of the trap, about $2 \cdot 10^6$ to $4 \cdot 10^6$ atoms at a constant temperature of 1 µK are provided at this time.

The high losses in this initial stage are clearly not desirable. Turning on the optical potential adiabatically is not an option, since the CO_2-laser beams move and change shape when the power is varied strongly. A solution might be to load the atoms into the trap, wait $1/4$ trap oscillation period until all atoms have moved into the trap center and the ensemble is effectively compressed, and then reapply Raman cooling. However, without some technical modifications the magnetic field cannot be switched back to the Raman cooling values quickly enough. It would also help to focus the trapping light more weakly, which would improve the phase-space matching between the Raman-cooled cloud and the trap. Up to now, the experimental conditions have been sufficient for achieving the scientific goals (see later chapters) of the experiment, so the improvements have been postponed.

6.5 Radio-frequency evaporation

The combined magnetic and optical trap allows for the use of a cooling mechanism that has proven very valuable in magnetic trapping experiments. Radio-frequency (RF) evaporative cooling has been the key tool in the first BEC experiments and remains the method of choice in magnetic trapping setups. In general, all Bose-Einstein condensates so far have been achieved by evaporative cooling, most of them via RF evaporation in a magnetic trap. For an introduction to evaporative cooling of trapped atoms see [Ket96].

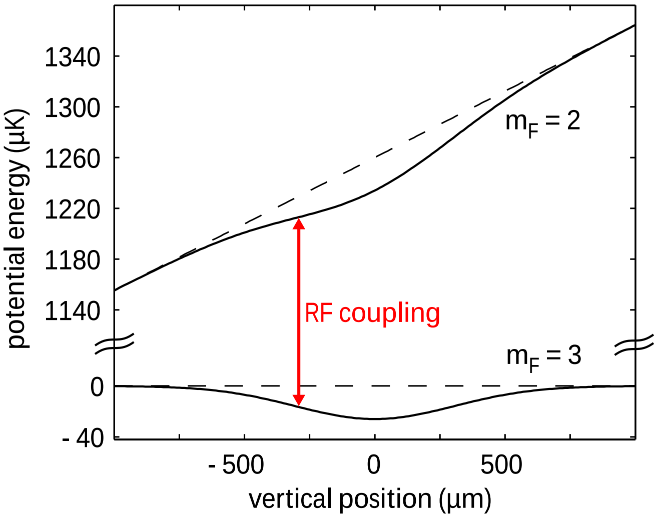

Figure 6.8: Radio-frequency evaporation out of the levitated trap. Shown are the potential energies of the $F = 3, m_F = 3$ and $F = 3, m_F = 2$ ground states (solid lines) along the vertical axis for a bias field of 75 G. The double arrow indicates the radio frequency transition between the states, which at a frequency of 26.2 MHz cuts into the trap about 300 µm below the trap center. The dashed lines represent the gravitational plus magnetic potential alone. Note the discontinuous energy scale.

Figure 6.8 shows the LevT potential for the two lowest-lying states of ^{133}Cs, the $F = 3, m_F = 3$ absolute ground state the trap is designed for and the untrapped state $F = 3, m_F = 2$. The levitation gradient field causes a spatial variation of the Zeeman splitting in vertical direction. Sending in a radio frequency resonant with the energy splitting at a certain altitude transfers the trapped atoms at this position into the untrapped state, and they fall out of the trap. If we tune the frequency to the trap center position, all atoms are lost; we have used this to calibrate the magnetic field generated by the bias coils [Mar03b]. When we start at a low radio frequency and slowly increase the value, we will begin throwing out the atoms at the trap edge, which are hottest. Through elastic collisions, the ensemble rethermalizes, lowering the temperature. Slowly moving this “radio-frequency knife” towards the trap center will then continuously cool the sample.

At a 75 G bias field, the scattering length is tuned to 1200 a_0, which at the low initial peak density of $3 \cdot 10^{11}$ cm^{-3} keeps the elastic scattering rate at ~200 s^{-1}, high enough for efficient cooling. The Zeeman splitting between the states at this bias field is of the order of $h \cdot 25$ MHz, a frequency that is easily supplied by standard programmable function generators (we use a Stanford Research Systems DS345 30 MHz arbitrary waveform generator). The signal from the waveform generator is amplified and then emitted by an antenna which is a simple coil with 5.5 cm diameter and six windings.

We have optimized the RF evaporation process in several steps. First, the RF knife is moved from a frequency $\nu = 25.5$ MHz which does not affect the trap at all to the point where it just barely starts to remove atoms ($\nu = 25.62$ MHz). This sweep takes two seconds and serves to define the starting point for the evaporation. From there on, the ramp is optimized in 5 s segments for evaporation efficiency: We vary the end frequency of the ramp down to the point where no atoms remain in the trap. For each end frequency, temperature T and atom number N are measured, from which we can derive the density n and the phase-space density D. The optimization is targeted at maximizing for each ramp segment the *evaporation efficiency*

$$\epsilon = \frac{\ln \frac{D}{D_0}}{\ln \frac{N_0}{N}}, \tag{6.11}$$

where N_0, D_0 are the atom number and the phase-space density at the beginning of the evaporation ramp, N, D the values after the ramp. The parameter ϵ simply states the orders of magnitude gain in phase-space density per order of magnitude loss in atoms. At the same time, the elastic collision rate, which can be calculated from the density and temperature at known scattering length, has to be monitored to not to drop too strongly, since evaporative cooling critically depends on elastic collisions for thermalization. Under good conditions, forced evaporation experiments in magnetic traps have efficiencies ϵ between 2 and 3, and the collision rate and density increase during evaporation (*runaway evaporation*).

Figure 6.9 gives an overview of the evaporation results. The rightmost data point shows the starting conditions, which in this experiment were $4 \cdot 10^6$ atoms at a temperature of 1 μK. The next, overlapping point is taken after the first 2 s ramp, which throws away some very few atoms and slightly lowers the temperature. Then, we have the first 5 s evaporation ramp, ending at an RF frequency of $\nu = 25.7$ MHz with $1.6 \cdot 10^6$ atoms at 450 nK. The efficiency of this ramp is $\epsilon = 1.6$. The next ramp segment goes to $\nu = 25.76$ MHz at $\epsilon \approx 1$, leaving $4.5 \cdot 10^5$ atoms at 200 nK. The final segment, in this case ended at $\nu = 25.81$ MHz, has a very low efficiency around 0.4. About 25000 atoms are left at around 60 nK. The collision rate stays in the range 100-200 s^{-1} during the first two evaporation ramps, during the last ramp it drops sharply to around 20 s^{-1}.

The results of the first two ramp segments are not very efficient, but quite reproducible and were used in the measurements on three-body recombination presented in

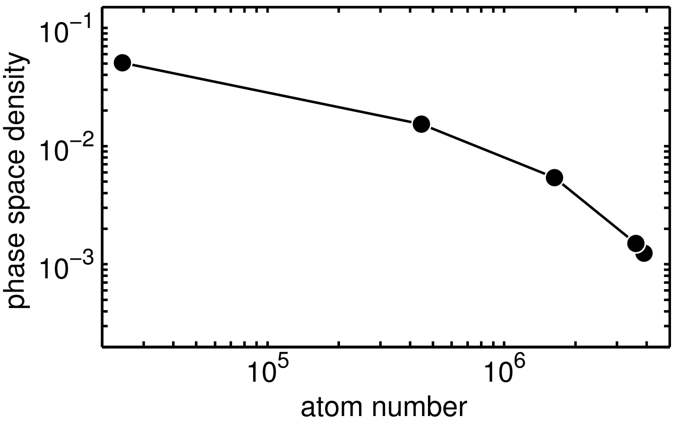

Figure 6.9: Results of radio-frequency evaporation in the LevT. The plot shows the increase in phase-space density in relation to the loss of atoms. Each connecting line between the measured atom number/phase-space density pairs corresponds to a segment of the evaporation ramp; the slope corresponds to the evaporation efficiency ϵ, the maximum value of which is 1.6 in the first segment (rightmost line).

Chapter 7. The last evaporation segment, however, is not only extremely inefficient but also varies strongly in its results. The reason is probably the noise in the magnetic bias field, which is of the order of 15 mG (see Sec. 5.4). This corresponds in the RF scale to 5 kHz, which in the last sweep of only 50 kHz very close to the trap center results in a large uncertainty.

The bias field noise, however, is not sufficient to explain the generally low efficiency of each step of the evaporation process. We have varied the time scales for evaporation by a factor of ten, tried to optimize the RF power and optimized the evaporation ramps for keeping up the collision rate and/or density. No significant improvement was found, the maximum phase-space density reached in a few single shots with very few atoms ranged around 0.1. The reason lies in the inherent one-dimensionality of our evaporation process: hot atoms can only leave the trap if their path leads them through the single vertical layer of the trap where the RF knife is effective. This is known to somewhat reduce the effectiveness of evaporation, but in our experiment has much more severe consequences. We found the reason for this to be recombination heating in three-body recombination, which will be discussed in the next chapter.

In view of the Oxford experiment (see Sec. 2.5) and their recent thorough study of evaporative cooling in cesium [Ma03], one should note that we are also operating in the hydrodynamic regime. However, in contrast to their magnetic trapping setup we do not suffer from inelastic two-body losses. A comparative quantitative analysis of the evaporation dynamics is planned and will further clarify the picture.

6.6 Observation and thermometry

We use an absorption imaging technique to measure the number of atoms and observe their spatial distribution. A resonant laser beam is used to cast a "shadow" of the atom cloud onto a CCD camera. This method is a standard technique quite commonly used in cold atom experiments [Ket99].

We use linearly polarized light resonant on the $F = 4 \rightarrow F' = 5$ transition. We turn on the MOT repumper 500 µs before the imaging cycle to pump all atoms into the $F = 4$ hyperfine state and then keep it on during the typically 200 µs absorption pulse. The magnetic field is always turned off for imaging. In this situation, the absorption cross-section σ is calculated by averaging the Clebsch-Gordan coefficients over all m_F substates and yields $\sigma = 0.1945\lambda^2$ at zero detuning and if the laser intensity is below saturation. We have verified that there is no broadening of the line and the laser is sitting exactly on resonance by systematically detuning the imaging laser and measuring absorption. The line width measured by this method is 5.3(1) MHz, in very good agreement with the 5.22 MHz natural line width of the transition.

Our main camera looks at the cloud horizontally, and in the camera frame we call the horizontal direction x, the vertical direction y. If the absorption coefficient of the atoms for resonant light is given by σn, where n denotes the number density of atoms, integrating the atomic cloud along the optical axis z of the imaging system yields the transmission function

$$T(x, y) = e^{-\sigma\eta(x,y)}, \tag{6.12}$$

with $\eta(x, y) = \int n\, dz$ being the column density along z.

An image is generated in two steps. First, we capture the shadow of the atom cloud. Then, all light fields and magnetic fields are turned off for typically 900 ms to let all atoms fall out of the trapping region, and we subsequently take a reference image of the imaging light field. We divide the first image by the second and thereby obtain $T(x, y)$ in pixel units and $\eta(x, y) = -\ln(T(x, y))/\sigma$. If a pixel has dimensions $l \times l$ in the image plane, the atom number N_{count} can simply be calculated by

$$N_{\text{count}} = \int \eta(x, y)\, dx\, dy = \sum_{x,y} l^2 \eta(x, y). \tag{6.13}$$

The result of this simple summation is at very low signal dominated by noise, mainly given by the Poisson statistics of charge carriers on the CCD chip. The noise is averaged out by a Gaussian fit to the distribution

$$\eta(x, y) = \hat{\eta} e^{-(x/w_x)^2} e^{-(y/w_y)^2}, \tag{6.14}$$

with $w_{x,y}$ denoting the $1/e$ radii of the cloud. The particle number N_{fit} is then given by

$$N_{\text{fit}} = \pi l^2 w_x w_y \hat{\eta}, \tag{6.15}$$

when w_x, w_y are expressed in pixel units. At atom numbers above 10^5, and with a suitably defined region of interest for the summation, N_{count} and N_{fit} usually agree quite well. With the fit, down to about two- to three thousand atoms can be clearly distinguished from the background.

We can determine the pixel dimension l, which enters into the particle number calculations quadratically, quite precisely by letting an atom cloud fall down and fitting the time-dependence of the position of the Gaussian distribution with a gravitational parabola. The accuracy of this calibration is determined from the fit to be better than 1% and agrees with the calculated imaging magnification to within 0.5%. For our main CCD camera with 7.5 µm square pixels and a factor 1.25 magnification in the imaging setup, the calculated pixel size is 6.0 µm. The pixel size obtained from the fit to the falling atom cloud is 6.02 µm, which is the value we use in further calculations.

The main source of a systematical error of our atom number determination lies in the calculated absorption cross-section σ. The assumptions used in calculating the absorption cross-section can be broken by very weak magnetic stray fields. Generally, the method is prone to rather under- than overestimate the number of atoms. We estimate the typical systematic error depending on the experimental situation to up to 30%, which is confirmed by our experience in the experiments carried out so far.

It should be noted that absorption imaging is a destructive technique, which means that for each individual picture a full experiment run is required.

Temperature measurement

We measure temperatures by a time-of-flight technique. Assuming Maxwell-Boltzmann statistics in a thermal cloud, the velocity distribution in a trapped sample follows a Gaussian function with standard deviation

$$\sigma_v = \sqrt{\frac{k_B T}{m}}, \tag{6.16}$$

while the spatial density distribution in a harmonic trap is also Gaussian and can be written as

$$n = \hat{n} \exp\left(-\frac{x^2}{2\sigma_x^2} - \frac{y^2}{2\sigma_y^2} - \frac{z^2}{2\sigma_z^2}\right). \tag{6.17}$$

If we turn off the trapping potential and let expand this distribution in free space, the expansion in each spatial direction follows

$$\sigma_{x,y,z}(t) = \sqrt{\sigma_{x,y,z}^2(0) + \sigma_v^2 t^2}, \tag{6.18}$$

which is, in contrast to the expansion of a BEC, an isotropic expansion. Therefore, the temperature can be measured by taking absorption images at different times after release from the trap along an arbitrary axis. A least-squares fit of the measured widths to Eq. 6.18 with parameters $\sigma(0)$ and σ_v gives the initial cloud size and the velocity spread, which via Eq. 6.16 immediately yields a temperature value.

As a rather technical point, in describing the sample extensions we usually do not use Gaussian σ widths, but the $1/e$ radii which we write as w_x, w_y, w_z. These are a factor $\sqrt{2}$ larger than the corresponding σ, and Eq. 6.18 is transformed to

$$w_{x,y,z}(t) = \sqrt{w_{x,y,z}(0) + 2\sigma_v^2 t^2}. \tag{6.19}$$

At the sub-μK temperatures common in our experiment, it is necessary to let expand the atom cloud for a very long time to clearly measure the expansion. Therefore, we keep the levitation field turned on during the expansion phase. Through the transversal force of the levitation field, the cloud is then spread strongly in the horizontal direction. For this reason, we use only the vertical extension, which is not influenced by the levitation field, to determine the temperature. The maximum expansion time is limited by the loss of signal due to the horizontal spread to typically no more than around 100 ms.

Chapter 7

Three-body recombination

As explained in Sec. 2.6, we have designed our atom trap to minimize inelastic losses from the trapped sample. However, the first lifetime measurement shown in Fig. 6.6, Sec. 6.4 exposes a significant decay in atom number that exceeds technical effects from the trapping setup (i.e. background gas collisions) and shows non-exponential behavior.

To verify that this is an interaction effect, we have measured the atom loss and temperature of the sample after previous RF evaporation and while exposed to different magnetic bias fields. We apply the first RF ramp to cool the atoms to significantly below the 1 μK limit of plain evaporation to 450 nK, in this series of measurements about $1.3 \cdot 10^6$ atoms are then present. After this preparation at the usual 75 G bias field, the bias field is quickly ramped to a variable value between 10 G and 100 G[1] and held constant for 10 s. Then, we ramp back to 75 G to have fixed conditions in the last stage. The optical potential is then switched off, the atoms expand for 50 ms in the levitation field, and we take one absorption image to determine both atom number and temperature.

Figure 7.1 shows the data in comparison to the known *s*-wave scattering length. We see clearly that strong losses in atom number are correlated to high scattering length, and in particular all Feshbach resonances appear as loss features. Also, losses are correlated to heating, which rules out evaporation. The strong dependence on the scattering length shows that we are observing some inelastic interaction process within the sample.

Our approach to trap and cool cesium in its absolute internal ground state rules out inelastic two-body collisions. The next most probable effect, then, is three-body recombination. In three-body recombination, two atoms form a molecule, while a third atom takes away the binding energy. The third atom needs to be present to satisfy momentum and energy conservation.

Three-body recombination is of general importance in many-body systems. It has been studied in many areas of physics, and attempts to theoretically describe the pro-

---

[1] Below 10 G, the levitation gradient distorts the trapping potential too strongly for consistent measurements (cf. Sec. 6.3).

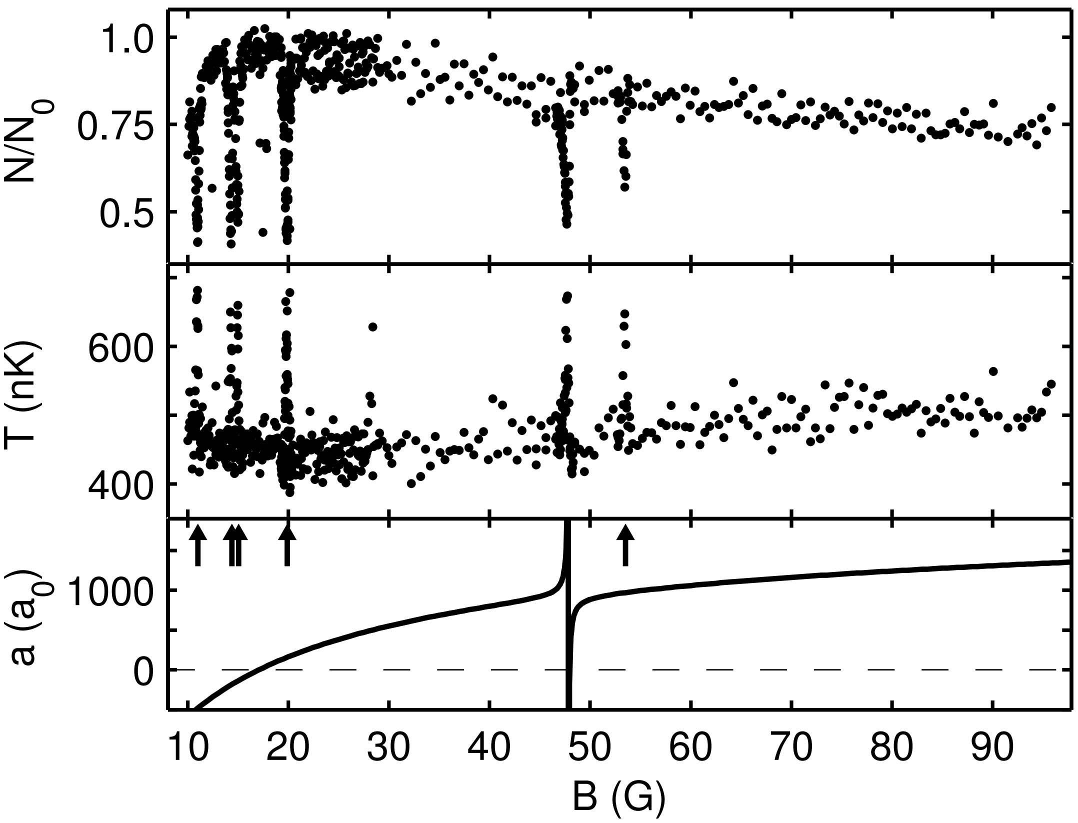

Figure 7.1: Remaining fraction of atoms N/N_0 (upper curve) and temperature T (middle) after 10 s in the CO_2-laser trap in a range of magnetic bias fields. Initially $N_0 = 1.3 \cdot 10^6$ atoms are prepared at 450 nK. For comparison, the lower plot shows the calculated scattering length a with additional Feshbach resonances indicated by arrows (see Sec. 2.4).

cess date back a long time. In dilute ultracold atomic gases, three-body recombination has previously been studied in few experiments only, the main challenge being to distinguish three-body losses from two-body losses. In magnetic traps, this is in general difficult, as dipolar relaxation is present as an inherent two-body loss mechanism. In the special case of magnetically trapped ^{87}Rb, experiments could nevertheless provide reliable data because of the anomalously weak two-body decay in this species [Bur97, Söd99]. In an optical trap, three-body loss in a Bose-Einstein condensate could be observed [SK98a]. Three-body recombination in bosonic systems with large s-wave scattering length a has been explored in experiments utilizing Feshbach resonances in ^{23}Na [Ste99] and ^{85}Rb [Rob00]. The results demonstrate the dramatic enhancement of loss processes near the resonances.

7.1 Theoretical predictions

Three-body recombination in ultracold atomic gases has been treated theoretically in a series of publications [Fed96, Nie99, Esr99, Bed00]. At very large scattering length, as in our experiment, the molecules created in recombination are predicted to be formed in the last bound state, which is a very weakly bound s level. Since three atoms need to be present for recombination, the event rate $\nu_{\mathrm{rec}} = \alpha_{\mathrm{rec}} n^3$ per unit volume and time scales with the third power of the atom density n. In the limit of ultralow interaction energies, the universal scaling law for the characteristic parameter α_{rec} is given as $\alpha_{\mathrm{rec}} = C\hbar a^4/m$ [Fed96], where m is the mass of the atom, and C a dimensionless factor. Predictions for C give values between 0 and ~70 [Fed96, Nie99, Esr99, Bed00], with oscillatory behavior between $C = 0$ and $C_{\max} = 67.9$ expected for strong variations of a on a Feshbach resonance [Bed00]. Previously available experimental data on three-body recombination for various species roughly agree with the general trend of a universal a^4 scaling, with evidence for deviations from this scaling law near a Feshbach resonance [Ste99].

In our experiment, we measure not three-body recombination events directly, but three-body losses. The three-body loss rate coefficient L_3 is related to α_{rec} via $L_3 = n_l \alpha_{\mathrm{rec}}$, where n_l denotes the number of atoms lost from the trap per recombination event. Therefore, the central relationship for comparing measurements to theory is

$$L_3 = n_l C \frac{\hbar}{m} a^4. \tag{7.1}$$

Usually, in discussing three-body recombination all atoms involved are assumed to be lost, setting $n_l = 3$. This results from the molecular binding energy ε being set free as kinetic energy in the recombination process. The molecule and the third atom receive $\varepsilon/3$ and $2\varepsilon/3$, respectively; since typically ε is large compared to the trapping potential depth, both are expelled from the trap. However, the binding energy of the weakly bound last energy level of the dimer is given by [Lan77][2]

$$\varepsilon = \frac{\hbar^2}{ma^2}, \tag{7.2}$$

and at very large scattering length values ε may be below the trap depth and the third atom cannot escape. If the potential of the atom trap does not confine the molecule, the dimer is lost and $n_l = 2$. If, however, the molecule is trapped and stays within the atom cloud, it may quickly quench its high vibrational excitation in an inelastic collision with a fourth trapped atom. The large amount of energy released in this situation expels the collision partners, making $n_l = 3$. In either case, the kinetic energy of the remaining atom is distributed in the ensemble, giving rise to recombination heating.

---

[2] A correction to this fundamental relation gives $\varepsilon = \hbar^2/\left(m(a-\bar{a})^2\right)$, with $\bar{a} = 95.5\, a_0$ for cesium [Gri93]. This correction is applied in later calculations.

7.2 Measurement procedure and data analysis

To obtain more quantitative results on recombination loss and heating, we have studied the time evolution of the atom number N and temperature T at various magnetic fields. As in the first measurement (Fig. 7.1), the atoms are pre-cooled via radio-frequency evaporation; for some measurements, we have additionally used the second RF ramp to cool $4 \cdot 10^5$ atoms to 200 nK. The hold time, which was fixed in the first measurement, is now varied over a range of several hundred seconds to obtain a decay curve and a heating curve. Figure 7.2 shows a typical measurement at $B = 56$ G.

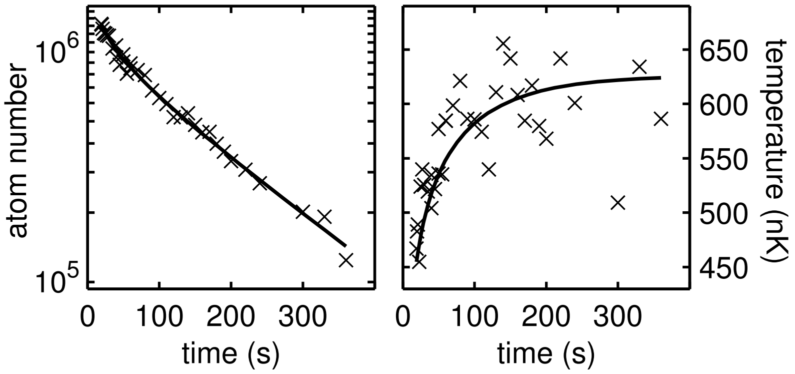

Figure 7.2: Atom number and temperature as a function of time in the trap at a bias field of 56 G. The solid lines show a numerical fit to the data. The corresponding three-body loss coefficient is $L_3 = 7(2) \cdot 10^{-25}$ cm^6/s.

To obtain the three-body loss coefficient L_3 from these measurements, we have to connect the measured quantities N and T to the loss rates treated in theory. Integrating the local three-body loss rate $L_3 n^3$ over the sample gives

$$\frac{\dot{N}}{N} = -L_3 \left\langle n^2 \right\rangle . \tag{7.3}$$

The average number density square in a harmonic potential can be calculated as

$$\left\langle n^2 \right\rangle = \frac{1}{\sqrt{27}} \left(\frac{m\bar{\omega}^2}{2\pi k_B T} \right)^3 N^2, \tag{7.4}$$

and inserting this into Eq. 7.3 yields

$$\frac{\dot{N}}{N} = -\gamma \frac{N^2}{T^3}, \qquad \gamma = L_3 \frac{1}{\sqrt{27}} \left(\frac{m\bar{\omega}^2}{2\pi k_B} \right)^3 . \tag{7.5}$$

With an additional loss term $-\alpha N$ for background gas collisions, we obtain a differential equation for the atom number,

$$\frac{dN}{dt} = -\alpha N - \gamma \frac{N^3}{T^3}. \tag{7.6}$$

Atom loss through three-body recombination leads to “anti-evaporation” heating. With its n^3 dependence, three-body recombination predominantly happens in the region of highest density in the trap center. The mean potential energy[3] of an atom undergoing a three-body process can be calculated by integrating over a thermal distribution with weights proportional to n^3, which yields $\frac{1}{2}k_BT$. As the ensemble average is $\frac{3}{2}k_BT$, for each lost atom an excess energy of $1k_BT$ remains in the sample. To account for recombination heating, we introduce an additional constant energy k_BT_h per lost atom. Relating the total heating energy $k_B(T + T_h)$ to the average energy $3k_BT$ of a trapped particle yields $\dot{T}/T = (\dot{N}/N)\, k_B(T + T_h)/(3k_BT)$, and we obtain an expression for the temperature evolution,

$$\frac{dT}{dt} = \gamma \frac{N^2}{T^3} \frac{(T + T_h)}{3}. \tag{7.7}$$

Equations 7.6 and 7.7 form a set of two coupled nonlinear differential equations for N and T, with parameters α, γ and T_h. Doing a least-squares fit of these two equations simultaneously to both the atom number and temperature measurements proves nontrivial, especially since the differential equations cannot be solved analytically. We use an iterative approach to find the best fit with following steps:

- choose values for α and γ,
- using these values, calculate a best fit of the numerical solution[4] of Eq. 7.7 to the temperature measurements, with T_h as the single fit parameter,
- calculate the error sum of squares e_N between the atom number measurements and the numerical solution of Eq. 7.6.

These steps are repeated while varying α and γ to minimize e_N using a nonlinear optimization algorithm[5]. Since the iteration includes a nested least-squares fit for T_h and several integration runs, the procedure is very time-consuming. To minimize the computing time, the initial guess for the parameters is obtained by fitting Eq. 7.6 to the atom number measurement alone with parameters α and γ assuming constant temperature. Then, the output of this is used to fit Eq. 7.7 to the temperature measurement with T_h as the only fit parameter.

The error limits for the fit parameters are based on χ^2 statistics. In multi-parameter fits, the 1-σ error for a fit parameter can be estimated by varying this parameter up and down, resp., to the points where χ^2 increases by one, while optimizing the other parameters [Bev92]. We cannot give statistically sound 1-σ error bars on the atom number and temperature measurements. Therefore, χ^2 is estimated to be equal to the number of degrees of freedom in the fit, which is the number of data points minus the number of fit parameters. The criterion for an increase of χ^2 by one therefore

---

[3] In the low-temperature limit, the recombination process does not depend on the kinetic energy.

[4] numerical integration performed with MATLAB 6.5 R13, function *ode15s*

[5] MATLAB 6.5 R13, optimization toolbox, function *lsqnonlin* [Col96].

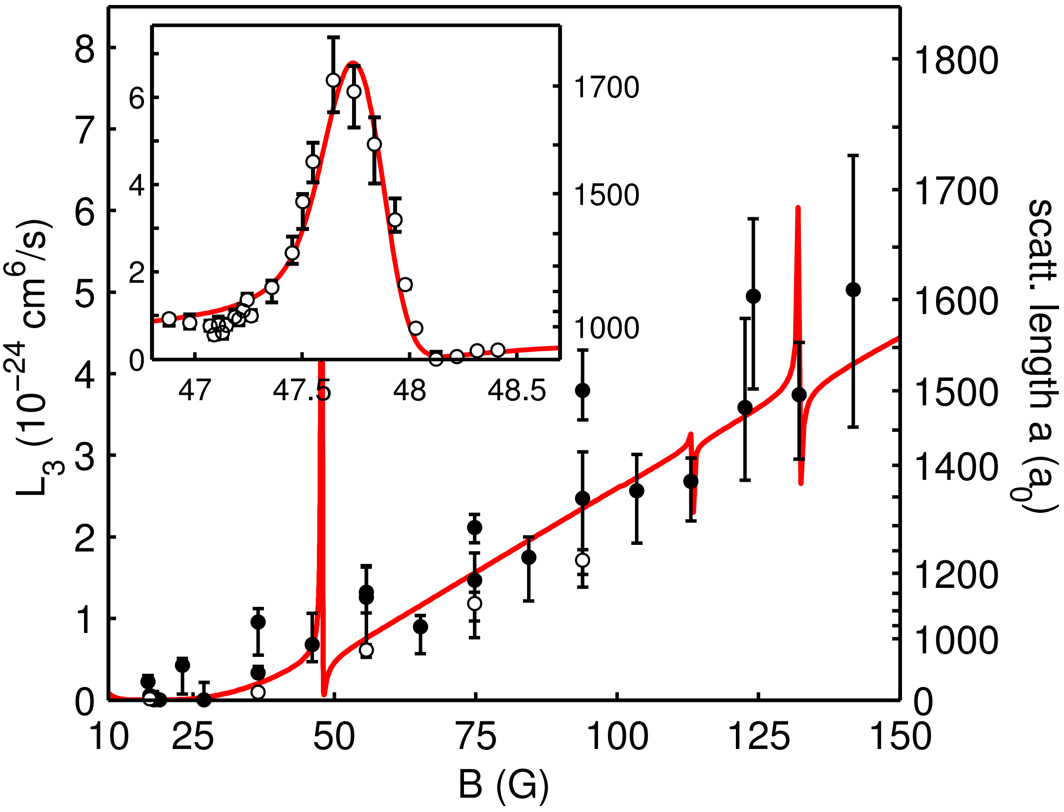

Figure 7.3: Measured values of L_3 as a function of the bias field B. Filled symbols represent measurements taken at an initial temperature of 200 nK, open symbols at 450 nK. The solid line shows the calculation according to Eq. 7.1 with $n_l C = 225$. The scale on the right-hand side displays the corresponding scattering length values. The inset shows the region around the 48 G resonance with a model fit (see text).

is equivalent to the increase of the error sum of squares by a fraction of (degrees of freedom)$^{-1}$. This procedures has been carried out for γ and T_h and gives the error bars in Figs. 7.3 and 7.5.

7.3 Recombination rates

The data obtained for L_3 as a function of the magnetic field is plotted in Fig. 7.3. The inset shows an expanded view of the data taken on the 48 G Feshbach resonance. The error bars represent the statistical errors derived from the fit as described above, which typically range around 20% at magnetic fields above the 48 G resonance. Below the resonance, where the recombination effect is very small due to the small scattering length, the errors quickly rise above 50%. The systematic uncertainty, however, is dominant: Due to the scaling of L_3 with $N^2\bar{\omega}^6$, small errors in these values amount to large differences in the result obtained for L_3. Taking the uncertainty in the trap frequency and an estimated 30% in atom number, the systematic error can be up to a factor of two.

In order to compare our data to theory, we do a least-squares fit of the expected scaling law (Eq. 7.1) to our measurements, using the calculated $a(B)$ (see Sec. 2.4). The single fit parameter is $n_l C$. The resulting curve is drawn as a solid line in Fig. 7.3. The data clearly confirm the universal a^4 scaling. In our experimental range, where a varies by less than a factor of two, we do not find any indication of resonant behavior[6] in C. The result from the fit is $n_l C = 225$, corresponding to $C = 75$ for $n_l = 3$ or $C = 112$ for $n_l = 2$. In comparison to theory, both values are somewhat above the upper limit of $C_{\max} \approx 70$, but in good agreement within our systematic error limit.

The scaling law for three-body recombination assumes an interaction cross-section for pair collisions of $\sigma = 8\pi a^2$ [Fed96]. This is only valid in the low-energy limit though; the general term in an ensemble of identical bosons is

$$\sigma = 8\pi \frac{a^2}{1 + k^2 a^2}, \tag{7.8}$$

where k is the collision wave number. We see that the relation between the scattering length and the wave number characterizes two limits of Eq. 7.8: If $ka \ll 1$, the expression simplifies to $\sigma = 8\pi a^2$, this is the low-energy case. If however, $ka \gg 1$, i.e. the collision energy is high, we get the unitarity limit $\sigma = 8\pi/k^2$ (see also Sec. 2.3).

In a thermal ensemble, we can calculate the inverse collision wave number as

$$k^{-1} = \left(\frac{4k_B T m}{\pi\hbar^2}\right)^{-1/2}. \tag{7.9}$$

The crossover between the limiting cases is now easily characterized by the comparison of this number to the scattering length. At 450 nK, $k^{-1} = 1500\ a_0$; at 200 nK, $k^{-1} = 2250\ a_0$. Correspondingly, for the data on the 48 G Feshbach resonance, which have been taken at 450 nK starting conditions and at very large scattering lengths, the unitarity limit cannot be neglected. The cross-section does not enter into the theoretical predictions in a straightforward way. Therefore, we simply introduce a cutoff in a to account for the finite temperature.

The cutoff is employed in the inset in Fig. 7.3, which shows the data on the Feshbach resonance. The cutoff value of 1800 a_0 results from a least-squares fit to the data. In order to completely model the shape of the resonance feature, we also have to take into account the width of the sample in the vertical B field gradient. The theory curve is convoluted with a Gaussian of full $1/e$ width 260 mG, which is given by the vertical

---

[6] C is predicted to undergo one full oscillation period between 0 and $C_{\max}$ when a varies by a factor of 22.7 [Bed00].

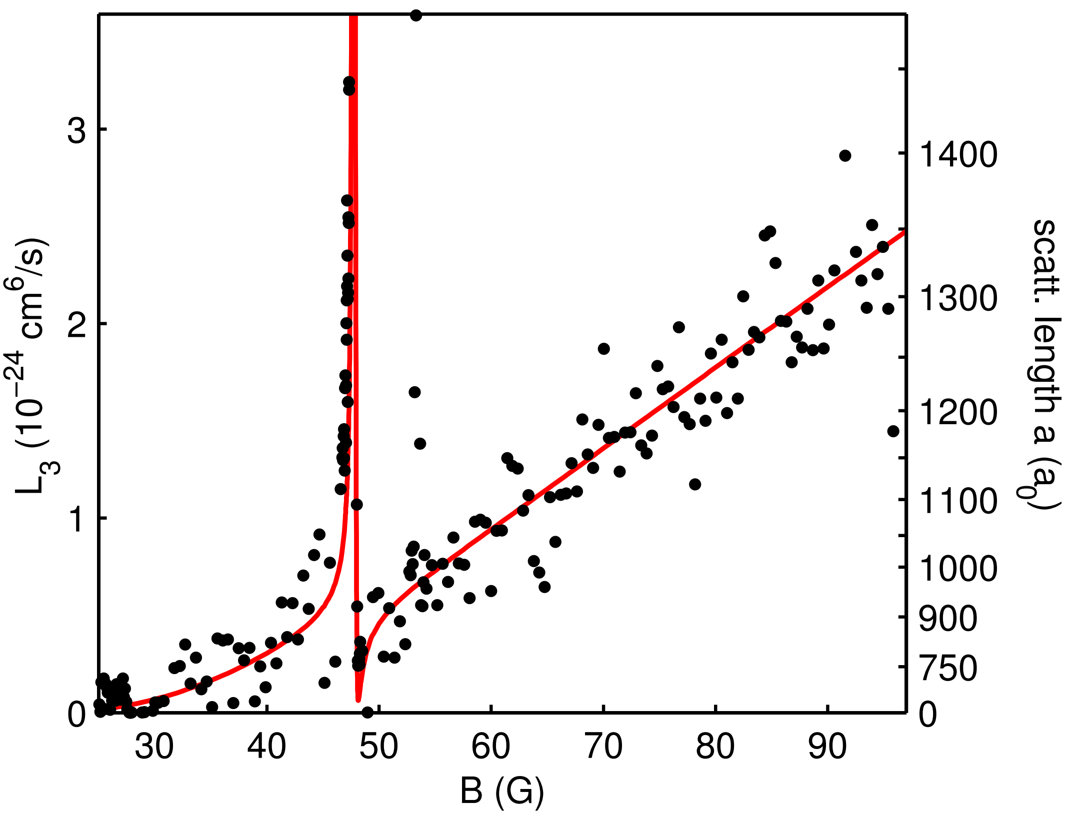

Figure 7.4: L_3 as a function of the bias field B for the measurement shown in Fig. 7.1. The solid line shows the calculation according to Eq. 7.1 with $n_l C = 165$. The scale on the right-hand side displays the corresponding scattering length values.

extension of the n^3 distribution of the trapped sample. Our B-field scale is slightly adjusted for an optimum match with theory by introducing a 40 mG shift, which is well within our calibration accuracy.

The confirmation of our model in comparison to the detailed decay and heating curves allows us now to re-evaluate the data taken for the first measurement shown in Fig. 7.1. Here, we only have one data point per magnetic field value. Therefore, our fit has too many parameters. We fix α to a value of 0.006 (corresponding to a background-gas limited $1/e$ lifetime of 170 s), which is a typical value obtained in the fits done before. However, α varies a bit over time due to small pressure variations in the system, with typical values between 170 s and 200 s. Even though the time scale in this measurement is fairly short (10 s), this introduces a systematic error.

The data are shown in Fig. 7.4. We see that the a^4 scaling is well confirmed within our measurement range. The value for $n_l C$ is at 165 somewhat lower than in the previous measurement, however the systematic uncertainty in this one-point fit does not allow any conclusions. Also, the data here are taken at 450 nK starting temperature and may be unitarity limited. We see this influence also in Fig. 7.3, where the few 450 nK data points (open symbols) lie rather below the main fit curve. However, within the systematic and statistical uncertainties of this measurement series, the values agree.

7.4 Recombination heating

Our results on recombination heating are displayed in Fig. 7.5. A trend towards smaller T_h at higher magnetic fields, corresponding to higher scattering lengths a, is visible. At large values of a close to the Feshbach resonance, the values are correspondingly very small. We compare the data to the scenario that the recombination heating arises just from the binding energy ε of the last bound state of the dimer. As the atom involved in the three-body recombination process receives $2\varepsilon/3$, the recombination heat per lost atom results to $k_B T_h = 2\varepsilon/(3n_l)$. Therefore, we assume $k_B T_h$ to be between $2\varepsilon/9$ ($n_l = 3$) and $\varepsilon/3$ ($n_l = 2$). This range is shown as a shaded area in Fig. 7.5. This simple model shows reasonable agreement with the experimental data. The heating measurements thus provide evidence of the formation of very weakly bound ultracold molecules.

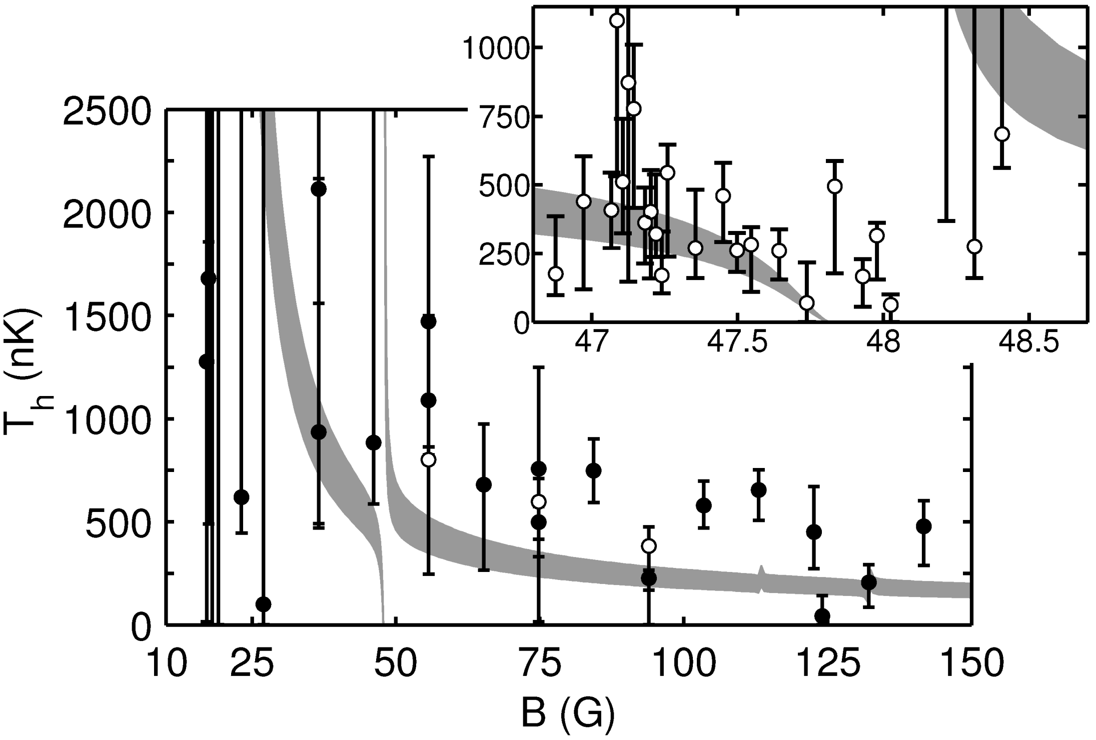

Figure 7.5: Recombination heat T_h as a function of the bias field B. Filled symbols represent measurements taken at an initial temperature of 200 nK, open symbols at 450 nK. The inset shows the region around the 48 G resonance. The shaded area shows the expected range based on the calculated binding energy of the last bound state of the Cs_2 molecule (see text).

This effect of recombination heating explains why the one-dimensional radio frequency evaporation is so inefficient. Usually, if in 1D evaporation the hottest atoms cannot escape immediately, they just re-distribute their energy among the sample and we have to wait until eventually collisions will create an atom with a high velocity component towards the evaporation surface. This only slows down the evaporation process, but does not heat. The same is true for the hydrodynamic regime. However, recombination heating converts molecular binding energy into kinetic energy and deposits $2\varepsilon/3$ into an atom, which can be much higher than the average energy of the sample. If this atom cannot escape immediately, it will via elastic collisions cause significant heating. In our case, in the last RF evaporation stage we get down to temperatures below 100 nK. The measured recombination heat T_h at 75 G is in the range of 500 nK, which is a lot higher than the average thermal kinetic energy but still easily trapped in the 10 μK potential if the atom does not immediately enter the region of the RF knife. Thus, especially at low temperatures $T \ll T_h$ the effect of recombination heating is severe.

Chapter 8

Bose-Einstein condensation

From the measurements on three-body recombination, we have learned that one-dimensional radio frequency evaporation as we have implemented it is not sufficiently efficient to reach quantum degeneracy with cesium. A new experimental tool not only provides very efficient evaporation, but on the way takes us on a “short cut” towards BEC.

8.1 The dimple trick

Several years ago, it was suggested and also demonstrated experimentally that adiabatically changing the shape of a potential can locally increase the phase-space density of a trapped atomic gas [Pin97]. Later, this effect was used to reversibly form a Bose-Einstein condensate in sodium by changing the peak phase-space density by a factor of more than 50 [SK98b]. In a work in our group, the same effect was used to strongly increase the phase-space density in a trapped cesium gas [Ham02a, Ham02b].

A change in the potential *strength* without modification of its *shape* cannot increase the phase-space density, any compression will be compensated by an increase in temperature and vice versa. Non-adiabatic changes will even decrease the phase-space density. The “trick” is doing a local modification of the potential. If we have a large trap loaded with cold atoms and locally introduce a small dip or “dimple” in the potential shape, the large sample will by elastic collisions load atoms into the dimple. Since the small sample trapped in the dimple is in thermal contact with the large reservoir of atoms, the temperature will be the same. However, in the stronger dimple potential the density, following the Boltzmann factor $\exp(U/k_B T)$, is higher, and thus the phase-space density is locally increased. A necessary condition is that the dimple is much smaller than the reservoir, because the reservoir has to take up the excess energy from the locally compressed sample in the dimple. If the dimple is too large, the reservoir will be heated and thus the increase in phase-space density diminished. Also, the dimple should be turned on adiabatically, otherwise the abrupt potential change will introduce heat into the system. A theoretical discussion of the “dimple trick” can

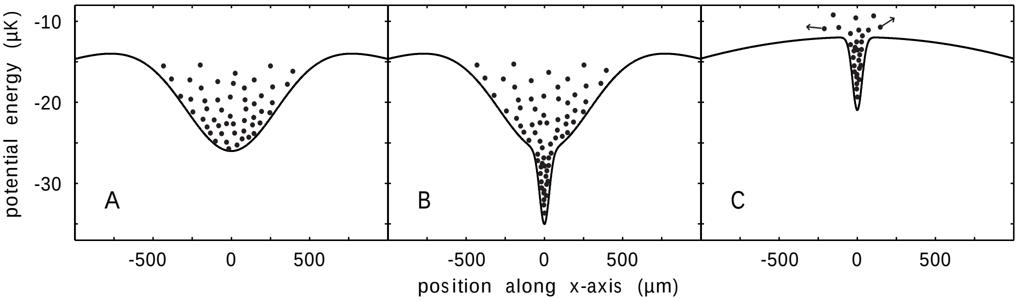

Figure 8.1: Illustration of the dimple principle. (A) Trapping potential of the reservoir. (B) Reservoir plus dimple. (C) Turning off the reservoir potential leaves only the compressed sample in the dimple.

be found in [Pin97] and [Wen00].

An example for this scheme is shown in Fig. 8.1. After the reservoir has been prepared, the dimple is adiabatically turned on and loaded from the reservoir by elastic collisions. If we now turn off the large potential, the reservoir atoms leave and we are left with a smaller, but significantly denser sample. Now, the dimple is the only trap and lowering the dimple potential allows for evaporative cooling.

The potential shapes shown in Fig. 8.1 are the actual calculated potentials of our trap.

8.2 The 1064-nm trap

We apply the dimple to our potential by adding an additional laser beam to the setup. From a 10 W Yb fiber laser (IPG Laser PYL-10) which is used in surface trapping experiments in our group [Ham02a], we split off about 500 mW. The light is sent through an AOM, coupled into a single mode optical fiber and thus transported into our lab. At the fiber output, it is expanded to ~8 mm diameter. By an $f = 300$ mm lens, the light is focused into the vacuum chamber to a beam waist of 30 µm. The beam encloses an angle of 30° with CO_2-laser 2 (see Fig. 8.2). A small fraction of the light is monitored on a photodiode, the signal of which is used to regulate the optical power via the AOM. This allows to control the dimple power from the maximum of 150 mW (which is limited by the AOM and fiber coupling efficiency) down to zero.

At a power of 50 mW, the dimple forms a cigar-shaped potential with a calculated depth of $k_B \cdot 9.2$ µK (see Sec. 4.2.2; detailed potential calculations can be found in [Mar03b]), a radial trap frequency of 254 Hz and an axial trap frequency of 2 Hz. Because of the very weak axial confinement, the dimple is even after removal of the reservoir always operated in conjunction with CO_2-laser 2, which increases the axial trap frequency to 6.2 Hz and has almost no influence on the radial trap frequency. The radial frequency has been measured at this power, the result of 257 Hz agrees very

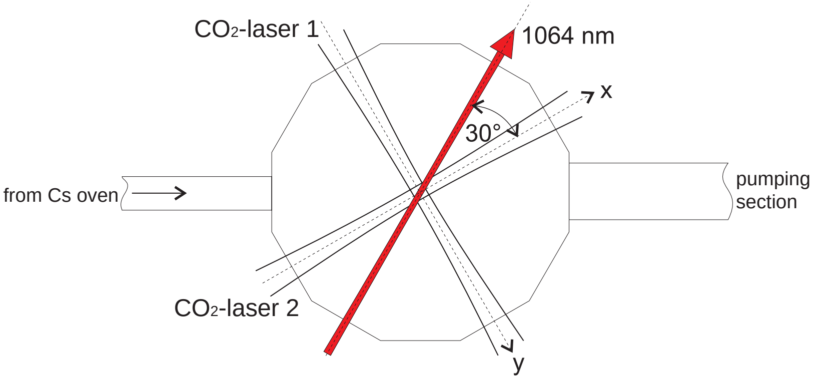

Figure 8.2: Configuration of the dipole potential laser beams (top view). The 12-sided shape in the center indicates the vacuum chamber.

nicely with the calculation. The trapping potential along the beam axis of the CO_2 laser can be seen in Fig. 8.1 (C).

Fig. 8.3 shows an image of the trapping potential in all spatial directions at a power of 5 mW. The radial trap frequency at this power is about 90 Hz, the axial frequency 6 Hz, the trap depth below 1 μK. Due to the strong effect of the magnetic anti-trapping force at the bias field of 23 G (see Sec. 6.3.2), any atom leaving the dimple into the CO_2-laser "tube" will be expelled from the trap center. Only atoms leaving almost exactly perpendicular to the CO_2-laser axis can re-enter the dimple and are able cause heating, however the solid angle for this case is very small. Thus, evaporation by reducing the dimple laser power is almost three-dimensional. Due to the levitation field, the dimensionality stays constant during the evaporation. In contrast to our case, typical magnetic trapping experiments suffer from gravitational sag, which effectively reduces the evaporation surface in the last stages [Ket96].

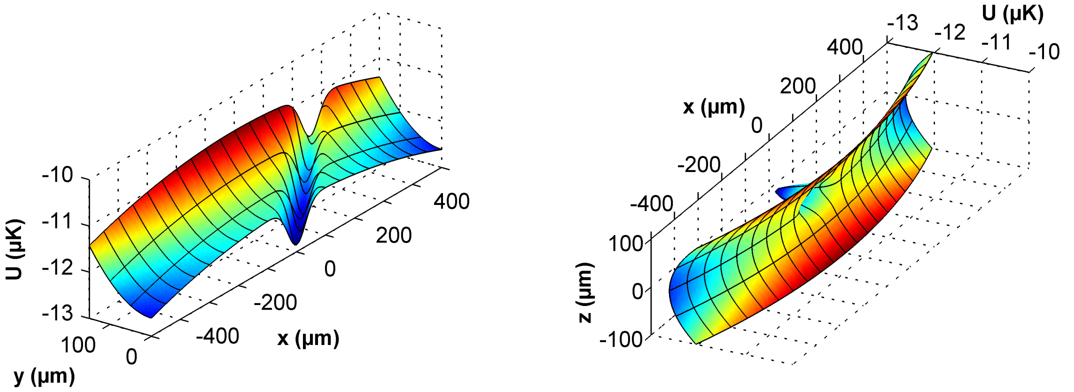

Figure 8.3: Potential of the dimple trap at $P_{\text{dimple}} = 5$ mW and $B_{\text{bias}} = 23$ G in the horizontal x-y plane at $z = 0$ (left) and in the vertical x-z plane at $y = 0$ (right).

8.3 Evaporative cooling towards BEC

The experiment sequence is illustrated in Fig. 8.4. The first image (A) displays the situation after the first 10 s of plain evaporation, with both CO_2 lasers turned on and without dimple. $2.5 \cdot 10^6$ atoms at a temperature of 1 μK form the reservoir at a peak density of $\hat{n} \simeq 2 \cdot 10^{11}$ cm^{-3} and a phase-space density of $D \simeq 6 \cdot 10^{-4}$. Then (B), the 1064-nm laser power is ramped up to 50 mW within 5 s to adiabatically load the dimple. Immediately afterwards, CO_2-laser 1 is turned off to remove the reservoir (C). We measure in the dimple about $3 \cdot 10^5$ atoms at an almost constant temperature of 1.1 μK, but with a very much increased peak density of $\hat{n} \simeq 8 \cdot 10^{12}$ cm^{-3}. Thus, the use of the "dimple trick" increases the phase-space density to $D \simeq 2.5 \cdot 10^{-2}$, an improvement by a factor of 40!

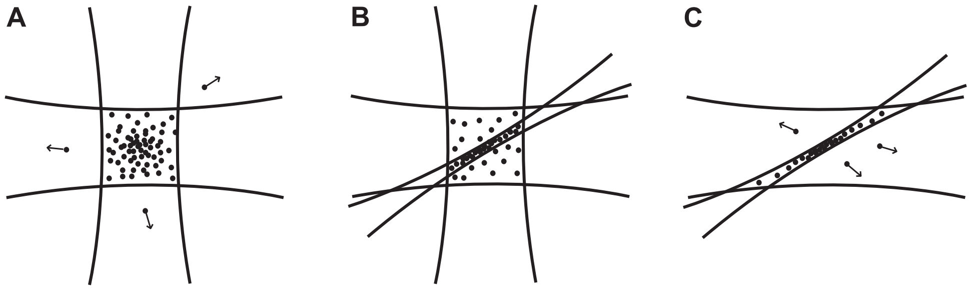

Figure 8.4: Three steps towards BEC of cesium: (A) The atomic reservoir at a magnetic bias field of 75 G (scattering length tuned to 1200 a_0). (B) Five seconds of collisional loading of the dimple at 23 G ($a = 300\ a_0$). (C) Forced evaporative cooling by ramping down the dimple power over 17 s, with the magnetic bias field kept at 23 G. The potential profiles shown in Fig. 8.1 reflect a cut through the trap center along the axis of the CO_2 laser that is not turned off, with steps (A)-(C) equivalent to those shown here.

Starting with the ramping up of the dimple laser power, the magnetic bias field is switched to a value of 23 G, corresponding to a scattering length $a = 300\ a_0$. This serves to reduce three-body recombination losses at the increased density in the dimple and to avoid getting too far into the hydrodynamic collision regime. At the same time, the scattering length is still high enough to keep elastic collisions up, which are needed for loading the dimple and subsequent evaporation. In the loaded dimple, the initial elastic scattering rate is $\sim$300 s^{-1}. We find that reaching the BEC transition is only possible in a narrow window of ±2 G around the experimentally found optimum of 23 G.

After the loading of the dimple, we wait 2 s for some plain evaporation to occur. At roughly constant phase-space density, the temperature is reduced to 800 nK while about 35% of the atoms leave the trap. Now, the power of the 1064-nm laser is slowly ramped down within 13 s. In the first 3 s, a linear ramp decreases the dimple power from 50 mW to 10 mW. In this ramp, the temperature decreases to 260 nK, while the

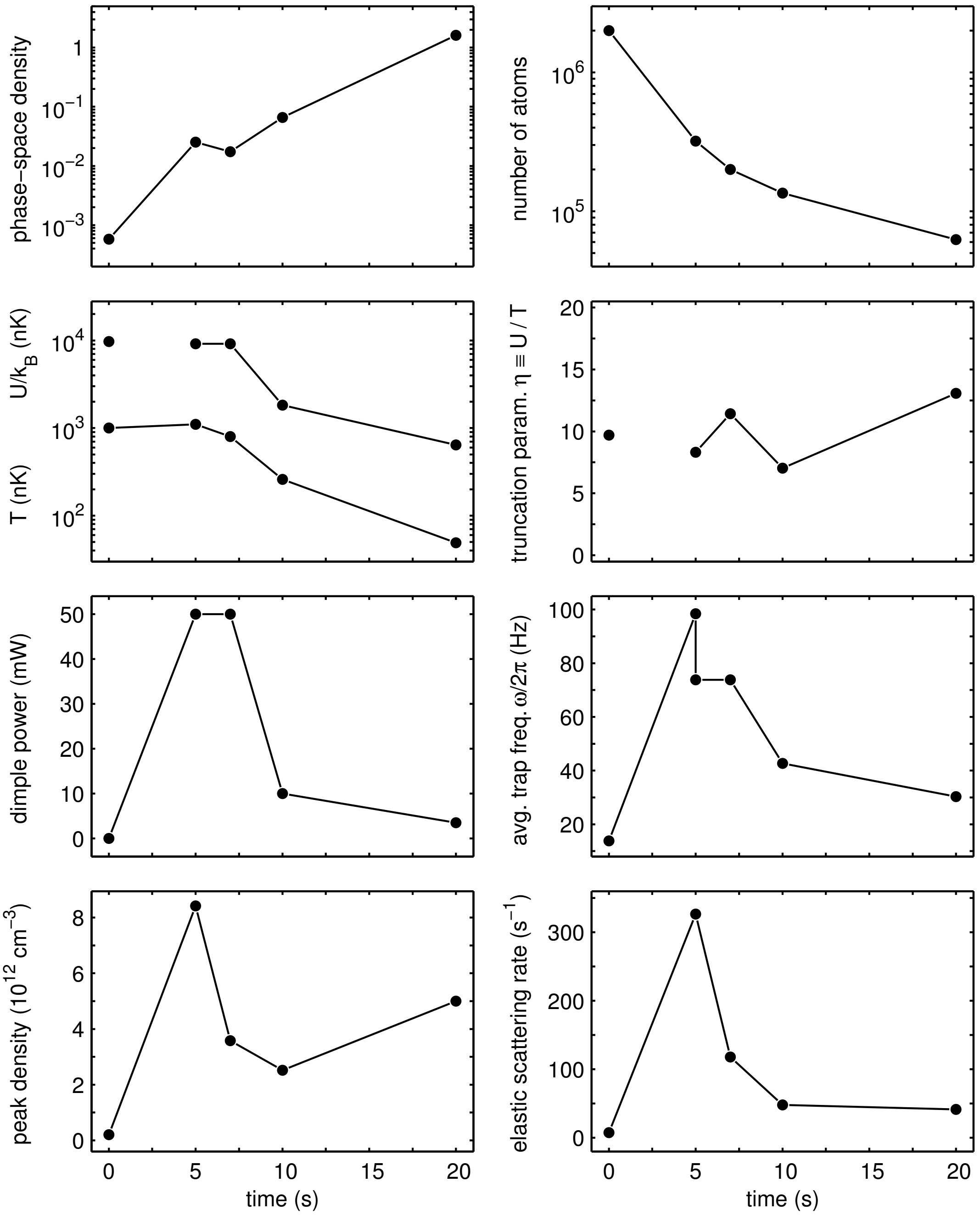

Figure 8.5: Sample parameters during the loading of the dimple and the subsequent forced evaporation. The starting point of the dimple loading ramp defines $t = 0$. At $t = 5$ s, one CO_2 laser is turned off, which shows as a sudden decrease in the trap frequency.

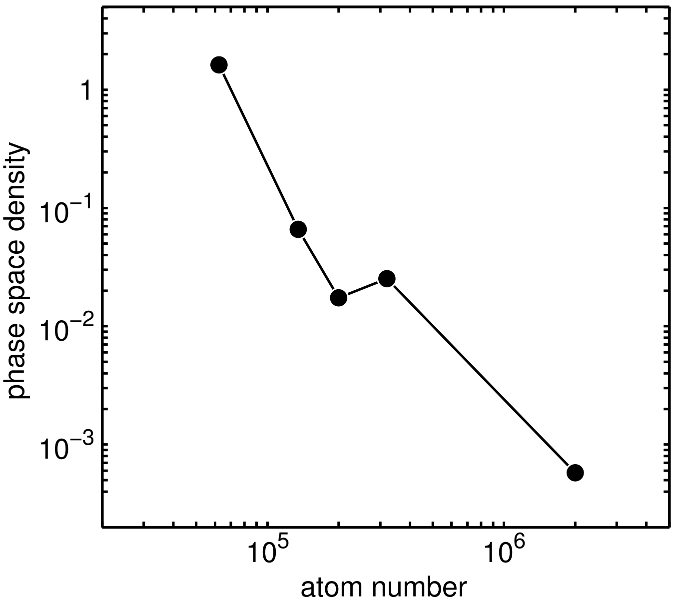

Figure 8.6: Results of dimple loading and subsequent forced evaporative cooling for an end power of 3.5 mW. The plot shows the increase in phase-space density in relation to the loss of atoms. Each connecting line between the measured atom number/phase-space density pairs corresponds to a segment of the evaporation ramp; the slope corresponds to the evaporation efficiency ϵ, the maximum value of which is 3.8 in the last segment (leftmost line).

atom number decreases by a further 30% to $1.4 \cdot 10^5$, raising the phase-space density to 0.07. The last ramp takes 10 s. If we set the end point of this ramp to a power of 3.5 mW, the remaining 65000 atoms have a temperature of 50 nK, and the calculated phase-space density is 1.6. Here we observe the phase transition to Bose-Einstein condensation.

Figure 8.5 shows some characteristic trap and sample parameters during evaporation. The data at the end of the dimple loading phase are a bit ambiguous: After 5 s, the second CO_2 laser is turned off, abruptly changing the trap frequency in the dimple and releasing the reservoir atoms. The 5 s values for density, scattering rate and phase-space density are calculated still using the higher trap frequency for the dimple in conjunction with both CO_2 lasers but neglecting the influence of the reservoir, they show the approximate status in the dimple at the end of the loading ramp. Unambiguous are the values at $t = 0$ and after $t = 7$ s. We see that the truncation parameter η, the ratio between the trap depth U and the temperature T, is roughly constant around 10. This allows for highly efficient evaporation. At elastic scattering rates above 100 s^{-1} and trap frequencies close to that value, the evaporation time scale is fast enough to not lose too many atoms to recombination losses.

In Fig. 8.6, the path towards BEC is shown starting with the standard $2 \cdot 10^6$ atoms at 1 μK after plain evaporation in the LevT. The first segment corresponds to the loading of the dimple, with a large gain in phase-space density. Then in plain evaporation some atoms are lost, and finally the two-step forced evaporation ramp leads to the phase transition. Note that the figure aspect ratio and horizontal scale are identical to the display of the RF evaporation efficiency shown in Fig. 6.9. The evaporation is very efficient, with $\epsilon = 3.8$ (for the definition of ϵ, see Eq. 6.11, Sec. 6.5) in the last segment.

In subsequent experiments, we have increased the maximum power of the dimple in the 5 s loading ramp to 90 mW instead of 50 mW. Instead of waiting for plain evaporation, the power is then immediately ramped down to 50 mW within 2 s. The following evaporation path is identical. This procedure yields about 10% more atoms at the critical temperature.

Figure 8.7 shows absorption images, Fig. 8.8 density profiles of the atom cloud after 50 ms of expansion at varied end powers of the last evaporation ramp. At 3.45 mW end power, we see a thermal cloud just at the critical temperature of 46 nK. At 2.2 mW, the condensate has started to form in the center, and finally at an end power of 1 mW, we have an almost pure condensate of 16000 atoms. This condensate has in the 1 mW dimple trap a Thomas-Fermi radius (Sec. 3.2.2) of 4.7 μm in the radial and 30 μm in the axial direction. The chemical potential is $\mu = k_B \cdot 10$ nK, the peak condensate density $\hat{n} = 1.4 \cdot 10^{13}$ cm^{-3}. We have measured the condensate lifetime in the trap to be approximately 15 s.

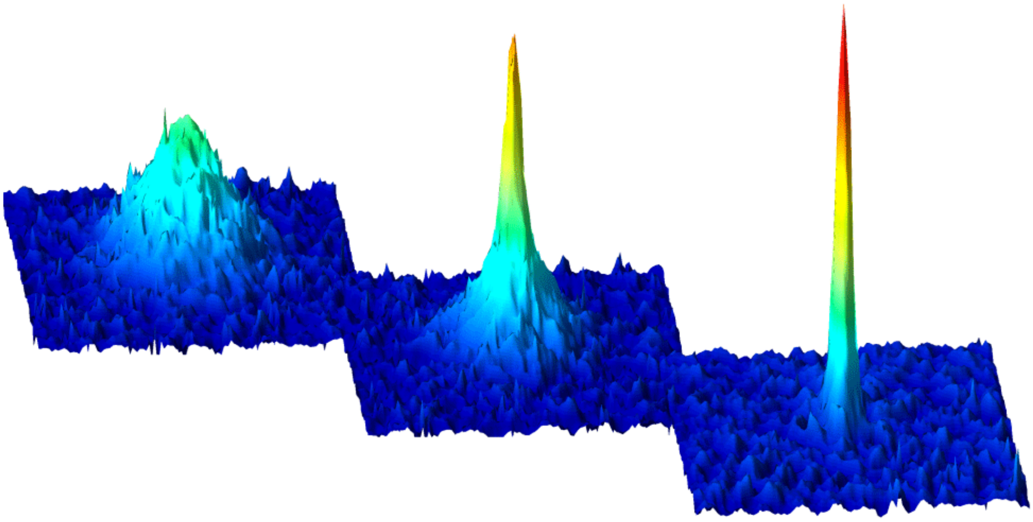

Figure 8.7: The Bose-Einstein condensate of cesium enters the stage! The density profiles shown in Fig. 8.8 are taken from these images. Left, dimple end power 3.45 mW; center, 2.2 mW; right, 1.0 mW.

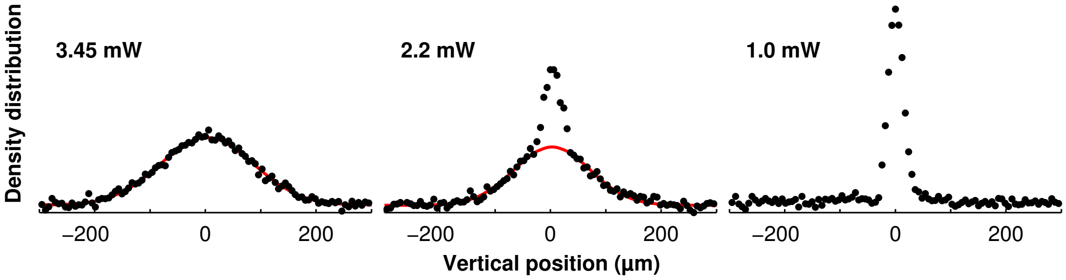

Figure 8.8: Vertical density profiles (integrated over a central 130 µm strip) of the atom cloud after 50 ms of expansion at varied end powers for the last evaporation ramp. The numbers give the dimple power, the solid line shows a Gaussian fit to the wings of the distribution from which a temperature is derived: at 3.45 mW, $T = 46$ nK; at 2.2 mW, $T = 30$ nK.

8.4 Exploring the tunability

In first experiments with the cesium condensate, we have demonstrated the different mean-field interaction regimes. With our tunable quantum gas, we can via the magnetic field easily switch to different values of the scattering length a and thus strongly vary the mean-field interaction in the condensate.

We create an almost pure BEC of 16000 atoms by ramping the dimple power down to 1 mW. At this power, the trap depth is 180 nK, the average trap frequency $\bar{\omega}/2\pi = 20.4$ Hz (radial $\omega_r/2\pi = 38$ Hz, axial $\omega_z/2\pi = 5.9$ Hz). The bias field is at this point still at 23 G, resulting in a scattering length of $a = 300\ a_0$. We want to study the strength of the mean-field interaction through the free expansion of the condensate, so we turn off the trap synchronously with the switching to a variable magnetic bias field. The levitation field is kept on to facilitate studying the condensate expansion on a long time scale[1]. The variable bias field is applied for a short time interval of 10 ms, which is sufficiently long for the mean-field dynamics to take place. For subsequent expansion at fixed conditions, the magnetic bias field is switched to 17 G. After a total expansion time of 50 ms, the vertical extension of the cloud and the total number of atoms are measured. The corresponding results (Fig. 8.9) show a marked dependence on the magnetic field with three distinct regions:

Below 17 G (region I), the scattering length is negative. We can calculate from the average trap frequency and the condensate atom number, that the minimum scattering length at which our ^{133}Cs BEC would be stable is $a_{\mathrm{cr}} \simeq -1.5\ a_0$ (Eq. 3.25). The calculation is strictly valid only for a spherical trap, however as the aspect ratio of our trap at this power is only ~6, the order of magnitude of the result should be right. Consequently, our BEC "implodes" as soon as we tune the scattering length beyond the zero-crossing. We see a large momentum spread due to the implosion dynamics

---

[1] Without the levitation field, the atoms fall out of the field of view of our CCD camera within 35 ms. The absolute maximum falling time of a released sample is limited by the position of the lower UHV viewport 15 mm below the trap to 55 ms.

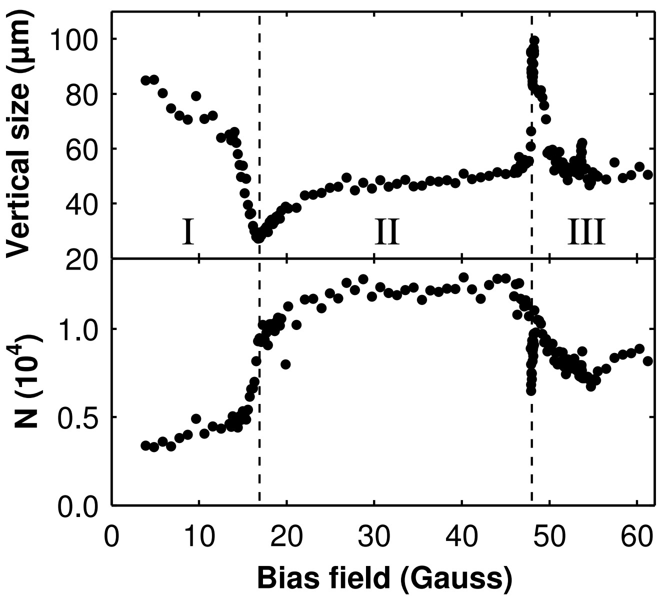

Figure 8.9: Expansion of the BEC and losses in atom number N after switching the bias field to a variable value for 10 ms and subsequent expansion at 17 G for 50 ms.

and a substantial loss of atoms.

Between 17 G and 48 G (region II), the scattering length is positive and varies smoothly from zero to about 1000 a_0. The expansion shows the minimum width at 17 G and a following increase. We know that in the Thomas-Fermi approximation the mean energy per particle scales with $(Na)^{2/5}$ [Eq. 3.24]. Since the sample is not in equilibrium within the trap potential in our case, no exact scaling of the expansion energy with a is available, however it is clear that the rising scattering length creates a strong mean-field effect, which is visible in the broadening of the momentum distribution.

For higher fields (region III), the behavior is dominated by the narrow Feshbach resonance at 48 G. On this resonance, the cloud expands very rapidly as the condensate explodes in response to the strong sudden increase of its internal energy. In addition, a sharp loss feature is observed, which may indicate the formation of molecules in the BEC [Don02]. At even higher fields, the data show an asymmetry and broadening of the resonance together with a loss of atoms, which we attribute to the finite ramp speed over the resonance [Cor00]. A small “explosion” feature is also visible on the very narrow 53 G g-wave Feshbach resonance.

8.5 Creating an ideal gas

In a further series of experiments, we have measured the mean-field self-interaction of the BEC on the zero-crossing of the scattering length at 17 G. As in the previous mea-

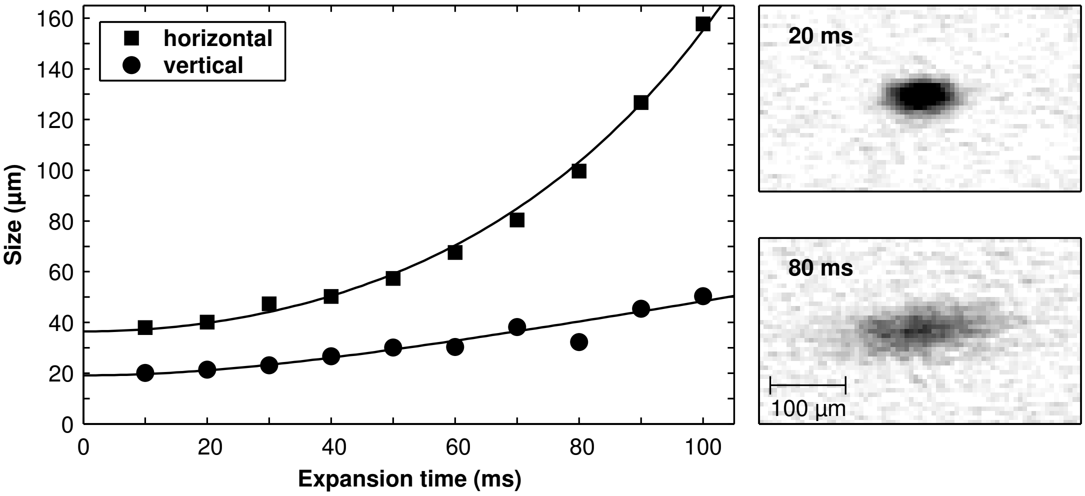

Figure 8.10: Expansion of the condensate at low scattering length. The data points at left show the $1/e$ half-widths of Gaussian fits to absorption images of the expanding cloud. The horizontal expansion is dominated by the levitation field's anti-trapping force (see text), a fit to the vertical expansion yields a mean kinetic energy of $\frac{1}{2}k_B \cdot 1200$ pK.

surement, a condensate of 16000 atoms is prepared in a 1 mW dimple trap. Figure 8.10 shows the measured expansion of the condensate released from the trap immediately after the magnetic field is switched to 17 G.

In the horizontal direction, the condensate expands strongly. This is due to the fact that we let the condensate expand in the levitation field. Integrating the horizontal force $F_\rho = m\alpha^2\rho$ (cf. Eq. 6.8, ρ is the radial coordinate, α a bias field dependent constant characterizing the outward curvature of the potential) yields the relation for the $1/e$ radius w_ρ

$$w_\rho(t) = w_{\rho,0}\cosh(\alpha t), \tag{8.1}$$

where $w_{\rho,0}$ denotes the original radial extension, assuming zero initial velocity. The upper line drawn in Fig. 8.10 shows the expansion calculated from Eq. 8.1, with $w_{\rho,0}$ as the only adjustable parameter. The observed expansion is fully explained by the magnetic forces and compatible with vanishing initial kinetic energy. In the vertical direction, there is no such effect and we measure a very slow expansion with an average kinetic energy as low as $\frac{1}{2}k_B \cdot 1200$ pK.

In equilibrium, the radial size σ_Φ of the wave function of an ideal Bose condensed gas is $\sigma_\Phi = a_{\mathrm{ho},r}$ (Sec. 3.2), which in our trap at 38 Hz radial trap frequency results in a value of 1.41 µm. Since the density is derived from the wave function as $n(\boldsymbol{r}) = |\Phi(\boldsymbol{r})|^2$, the size of the corresponding density distribution is $\sigma_r = \sigma_\Phi/\sqrt{2} = 1.0$ µm.

The ground state energy in a harmonic oscillator is given simply by $\hbar\omega/2$, which for our trap parameters yields a value for the expansion energy of $\sim\frac{1}{2}k_B \cdot 910$ pK. However, in our experiment the density distribution of the ideal gas is *not* in equilibrium. We create the condensate under strong repulsive interaction, leading to a spreading of the condensate. In the Thomas-Fermi approximation, the radius of the BEC created in the evaporation process at $a = 300\ a_0$ is $R_r = 4.67$ µm (Eq. 3.23). An approximation of the equivalent Gaussian radius is obtained by numerically calculating the standard deviation of the inverted parabola shape of the condensate, resulting to $\sigma_r = 0.447 R_r$. The size of the BEC in this approximation is $\sigma_r = 2.09$ µm.

Since in the absence of interactions the condensate energy results only from the momentum spread induced by the uncertainty relation via $\sigma_p \propto 1/\sigma_r$, and the kinetic energy follows $E = p^2/2m$, we get a scaling law $E \propto 1/\sigma_r^2$. Therefore, to obtain the expansion energy when the condensate is released from the trap, we simply scale the energy in the equilibrium case and calculate a value of $E \gtrsim \frac{1}{2} k_B \cdot 210$ pK. We see that the condensate still has much more energy than would be expected when the interactions are perfectly cancelled. We attribute this to residual mean-field effects from the finite time scale in switching the magnetic fields and imperfections in the synchronization between turning off the trap and turning off the interactions.

In a further experiment, we have tried to improve the magnetic field switching procedure. By optimizing the time at which the magnetic field is changed from the BEC creation value of 23 G to 17 G, by optimizing the exact final magnetic field value, and by maximizing the ramping speed, the average kinetic energy of the expanding condensate could be reduced to a minimum of $\frac{1}{2} k_B \cdot (220 \pm 100)$ pK. The expansion curve is shown in Fig. 8.11.

In this experiment, the dimple power is ramped down to a value of 0.6 mW, the condensate consists of 10000 atoms. The relevant trap frequencies are $\bar{\omega}/2\pi = 17.8$ Hz, $\omega_r/2\pi = 30.9$ Hz. The corresponding radial condensate size is $R_r = 4.82$ µm, thus we expect for a perfectly non-interacting gas an average kinetic energy of $\gtrsim \frac{1}{2} k_B \cdot 195$ pK. We see that we have within our measurement uncertainty perfectly turned off the mean

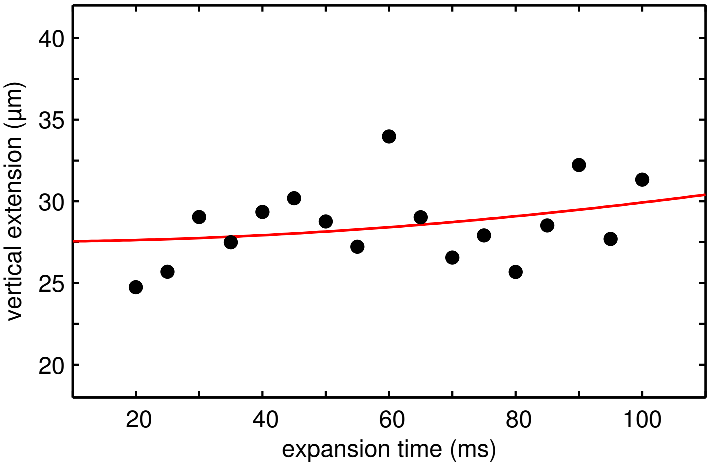

Figure 8.11: Expansion of the optimized "frozen" condensate. The solid line shows a fit to the data giving an average kinetic expansion energy of $\frac{1}{2} k_B \cdot 220$ pK.

field in this case. The ensemble corresponds quite well to what we call a “frozen” condensate, a system almost without internal energy.

To further reduce the condensate energy, we could load a larger condensate of around 50000 atoms back into the almost isotropic CO_2-laser trap at 14.5 Hz trap frequency at a scattering length of around 500 a_0. These values can all be easily reached in our setup, the Thomas-Fermi condensate radius would then be 14 µm. Turning off the interaction in this system would leave a residual kinetic energy of only $\sim\frac{1}{2}k_B \cdot 5$ pK. By changing the optical setup with the available lasers, we could realize a sufficiently deep potential at trap frequencies of the order of 1 Hz, further reducing the energy. This could be an ideal system for precision measurements at ultralow energies.

Chapter 9

Outlook

In the frame of this thesis, an experimental setup was built that has enabled for the first time the creation of a Bose-Einstein condensate of ^{133}Cs. The setup allows great flexibility in the experiments conducted with the condensate, which at the time of this writing has already been used to explore new areas of physics.

After the initial creation of the BEC and the measurements presented in this thesis and published in [Web03a], the experimental setup was improved in terms of stability. The Raman cooling lattice laser was changed to a new system with better beam quality in order to allow for better spatial localization of the output cloud. By careful readjustment of the whole system around the improved cooling laser and in-depth optimization of the evaporation ramp, the number of atoms in the condensate could be increased to up to 80000 (cf. [Web03c]).

The first experiment utilizing the condensate was to explore the molecule creation on a Feshbach resonance. By sweeping the magnetic field over the narrow resonance

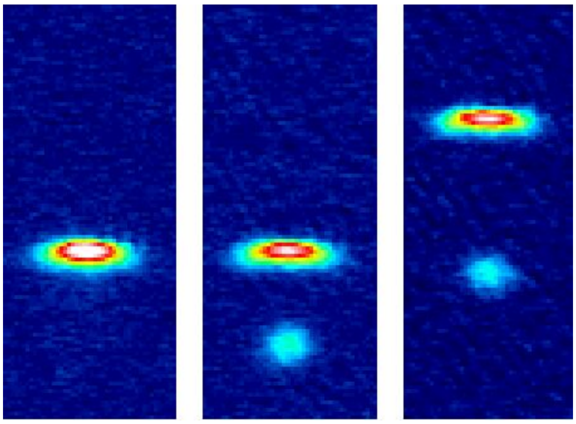

Figure 9.1: New experiments in the levitated trap. From left to right: (1) a pure condensate of 60000 atoms, (2) 5000 possibly quantum degenerate Cs_2 molecules falling out of the atomic BEC, (3) levitated molecules.

at 20 G, we have created an ultracold sample of Cs_2 molecules [Her03]. Through their different magnetic moment, the molecules are removed from the atomic BEC and can be separately imaged. Adjusting the levitation gradient for the molecules allows for a precise measurement of their magnetic moment, which is found to be in excellent agreement with theory. We measure extremely low expansion energies, consistent with the presence of a molecular BEC. Currently, we are exploring the possibility to measure coherence effects in the molecular cloud to find evidence for quantum degeneracy.

The molecules formed can in principle be trapped in our setup. A previous experiment shows evidence of trapping of the Cs_2 dimer in a CO_2-laser trap [Tak98], and our first experiments show that the magnetic levitation concept also works for the molecules. To reliably trap the molecules, the timing and field switching in the molecule creation procedure needs to be optimized in order to reduce the initial momentum kick induced by the mismatched levitation condition between atomic and molecular sample. This is currently in progress.

Besides the studies in the molecular sample, the unique tunability offered by cesium is of great interest in various respects. In the field of quantum gases, it may serve as the experimental key to explore new regimes beyond standard mean-field theory. When the scattering length is raised to a value of the order of the inter-particle spacing, which is possible close to Feshbach resonances, the system is no longer in the weakly interacting regime, and the usual theoretical descriptions fail.

It is possible to realize a system with reduced dimensionality via the tunable scattering length: In a strongly anisotropic trap, the scattering length can be raised to very large values of the order of the sample extension along the strongly confined axes. The contrary case, a “frozen” BEC at zero scattering length without internal energy, would represent an ideal source of cold atoms for applications in metrology. This is a perfect system for precision measurements, e.g. of the photon recoil [Gup02].

In the Mott insulator phase [Jak98, Gre02], the phase transition depends on the relation between the atom-atom interaction and the tunnel coupling. The tunable scattering length allows to reach the transition via changing the scattering length instead of the potential depth. This allows great flexibility in the control of the phase transition, offering intriguing possibilities in the realm of molecular quantum matter [Jak02].

Shortly before the completion of this thesis, a second Bose-Einstein condensate of cesium has been achieved in our group [Ryc03]. In this experiment in a gravito-optical surface trap (GOST), the geometry is effectively two-dimensional. As we have in the past, we expect to continue to benefit much from synergy effects between experiments in these complementary setups.

References

[And95] M. H. Anderson, J. R. Ensher, M. R. Matthews, C. E. Wieman, and E. A. Cornell, *Observation of Bose-Einstein Condensation in a Dilute Atomic Vapor*, Science **269**, 198 (1995).

[Arl98] J. Arlt, P. Bance, S. Hopkins, J. Martin, S. Webster, A. Wilson, K. Zetie, and C. J. Foot, *Suppression of collisional loss from a magnetic trap*, J. Phys. B **31**, L321 (1998).

[Arn97] M. Arndt, M. B. Dahan, D. Guéry-Odelin, M. W. Reynolds, and J. Dalibard, *Observation of a Zero-Energy Resonance in Cs-Cs Collisions*, Phys. Rev. Lett. **79**, 625 (1997).

[Bal99] S. Bali, K. M. O'Hara, M. E. Gehm, S. R. Granade, and J. E. Thomas, *Quantum-diffractive background gas collisions in atom-trap heating and loss*, Phys. Rev. A **60**, R29 (1999).

[Bed00] P. F. Bedaque, E. Braaten, and H.-W. Hammer, *Three-body recombination in Bose gases with large scattering length*, Phys. Rev. Lett. **85**, 908 (2000).

[Ber01] F. Bertinetto, P. Cordiale, G. Galzerano, and E. Bava, *Frequency Stabilization of DBR Diode Laser Against Cs Absorption Lines at 852 nm Using the Modulation Transfer Method*, IEEE Transactions on Instrumentation and Measurement **50**, 490 (2001).

[Bev92] P. R. Bevington and D. K. Robinson, *Data reduction and error analysis for the physical sciences*, McGraw-Hill, New York, 1992, 2nd ed.

[Bjo88] J. E. Bjorkholm, *Collision-limited lifetimes of atom traps*, Phys. Rev. A **38**, 1599 (1988).

[Bog47] N. Bogoliubov, *On the theory of superfluidity*, J. Phys. **11**, 23 (1947).

[Boi96] D. Boiron, A. Michaud, P. Lemonde, Y. Castin, and C. Salomon, *Laser cooling of cesium atoms in gray optical molasses down to 1.1 μK*, Phys. Rev. A **53**, R3734 (1996).

[Bon02] K. Bongs and K. Sengstock, *Introduction to Bose-Einstein Condensation*, in: M. Weidemüller and C. Zimmermann (Eds.), *Interactions in Ultracold Gases*, Wiley-VCH, Weinheim, 2002.

[Bos24] S. Bose, *Plancks Gesetz und Lichtquantenhypothese*, Z. Phys. **26**, 178 (1924).

[Bra95] C. C. Bradley, C. A. Sackett, J. J. Tollett, and R. G. Hulet, *Evidence of Bose-Einstein Condensation in an Atomic Gas with Attractive Interactions*, Phys. Rev. Lett. **75**, 1687 (1995), *ibid.* **79**, 1170 (1997).

[Bur97] E. A. Burt, R. W. Ghrist, C. J. Myatt, M. J. Holland, E. A. Cornell, and C. E. Wieman, *Coherence, Correlations, and Collisions: What One Learns about Bose-Einstein Condensates from Their Decay*, Phys. Rev. Lett. **79**, 337 (1997).

[Cas98] Y. Castin, J. I. Cirac, and M. Lewenstein, *Reabsorption of Light by Trapped Atoms*, Phys. Rev. Lett. **80**, 5305 (1998).

[Chi00] C. Chin, V. Vuletic, A. J. Kerman, and S. Chu, *High Resolution Feshbach Spectroscopy of Cesium*, Phys. Rev. Lett. **85**, 2717 (2000).

[Chi01a] C. Chin, *Cooling, Collisions and Coherence of Cold Cesium Atoms in a Trap*, Ph.D. thesis, Stanford University (2001).

[Chi01b] C. Chin, V. Leiber, V. Vuletić, A. J. Kerman, and S. Chu, *Measurement of an electron's electric dipole moment using Cs atoms trapped in optical lattices*, Phys. Rev. A **63**, 033401 (2001).

[Chi03a] C. Chin, private communication (2003).

[Chi03b] C. Chin, A. J. Kerman, V. Vuletic, and S. Chu, *Sensitive Detection of Cold Cesium Molecules Formed on Feshbach Resonances*, Phys. Rev. Lett. **90**, 033201 (2003).

[Chu85] S. Chu, L. Hollberg, J. E. Bjorkholm, A. Cable, and A. Ashkin, *Three-Dimensional Viscous Confinement and Cooling of Atoms by Resonance Radiation Pressure*, Phys. Rev. Lett. **55**, 48 (1985).

[Chu86] S. Chu, J. E. Bjorkholm, A. Ashkin, and A. Cable, *Experimental Observation of Optically Trapped Atoms*, Phys. Rev. Lett. **57**, 314 (1986).

[Col96] T. F. Coleman and Y. Li, *An Interior, Trust Region Approach for Nonlinear Minimization Subject to Bounds*, SIAM Journal on Optimization **6**, 418 (1996).

[Cor98] K. L. Corwin, Z.-T. Lu, C. F. Hand, R. J. Epstein, and C. E. Wieman, *Frequency-stabilized diode laser with Zeeman shift in an atomic vapor*, Appl. Opt. **37**, 3295 (1998).

[Cor99] E. A. Cornell, J. R. Ensher, and C. E. Wieman, *Experiments in dilute atomic Bose-Einstein condensation,* in: M. Inguscio, S. Stringari, and C. E. Wieman (Eds.), *Proceedings of the International School of Physics - Enrico Fermi*, 15, IOS Press, 1999, arXiv:cond-mat/9903109.

[Cor00] S. L. Cornish, N. R. Claussen, J. L. Roberts, E. A. Cornell, and C. E. Wieman, *Stable ^{85}Rb Bose-Einstein Condensates with Widely Tunable Interactions*, Phys. Rev. Lett. **85**, 1795 (2000).

[Cor02] E. A. Cornell and C. E. Wieman, *Nobel Lecture: Bose-Einstein condensation in a dilute gas, the first 70 years and some recent experiments*, Rev. Mod. Phys. **74**, 875 (2002).

[Dal99a] F. Dalfovo, S. Giorgini, L. P. Pitaevskii, and S. Stringari, *Theory of Bose-Einstein condensation in trapped gases*, Rev. Mod. Phys. **71**, 463 (1999), arXiv:cond-mat/9806038.

[Dal99b] J. Dalibard, *Collisional dynamics of ultra-cold atomic gases*, in: M. Inguscio, S. Stringari, and C. E. Wieman (Eds.), *Proceedings of the International School of Physics - Enrico Fermi*, 321, IOS Press, 1999.

[Dav95] K. B. Davis, M.-O. Mewes, M. R. Andrews, N. J. van Druten, D. S. Durfee, D. M. Kurn, and W. Ketterle, *Bose-Einstein Condensation in a Gas of Sodium Atoms*, Phys. Rev. Lett. **75**, 3969 (1995).

[Don02] E. A. Donley, N. R. Claussen, S. T. Thompson, and C. E. Wieman, *Atom-molecule coherence in a Bose-Einstein condensate,* Nature **417**, 529 (2002).

[Ein25] A. Einstein, *Quantentheorie des einatomigen idealen Gases. Zweite Abhandlung*, Sitzungber. Preuss. Akad. Wiss. **1925**, 3 (1925).

[Eng97] H. Engler, *Aufbau eines “Zeeman-Abbremsers” und Inbetriebnahme einer magnetooptischen Falle für Lithium-Atome*, Diploma thesis, Universität Heidelberg and Max-Planck-Institut für Kernphysik (1997).

[Eng00a] H. Engler, *A quasi-electrostatic trap for neutral atoms,* Ph.D. thesis, Ruprecht-Karls-Universität Heidelberg (2000).

[Eng00b] H. Engler, T. Weber, M. Mudrich, R. Grimm, and M. Weidemüller, *Very long storage times and evaporative cooling of cesium atoms in a quasielectrostatic dipole trap*, Phys. Rev. A **62**, 031402(R) (2000), doi:10.1103/PhysRevA.62.031402.

[Esr99] B. D. Esry, C. H. Greene, and J. P. Burke, Jr., *Recombination of three atoms in the ultracold limit*, Phys. Rev. Lett. **83**, 1751 (1999).

[Fed96] P. O. Fedichev, M. W. Reynolds, and G. V. Shlyapnikov, *Three-Body Recombination of Ultracold Atoms to a Weakly Bound s Level*, Phys. Rev. Lett. **77**, 2921 (1996).

[Fri98] D. G. Fried, T. C. Killian, L. Willmann, D. Landhuis, S. C. Moss, D. Kleppner, and T. J. Greytak, *Bose-Einstein Condensation of Atomic Hydrogen*, Phys. Rev. Lett. **81**, 3811 (1998).

[Geh98] M. E. Gehm, K. M. O'Hara, T. A. Savard, and J. E. Thomas, *Dynamics of noise-induced heating in atom traps*, Phys. Rev. A **58**, 3914 (1998).

[Ger99] M. Gertsvolf and M. Rosenbluh, *Injection Locking of a Diode Laser Locked to a Zeeman Frequency Stabilized Laser Oscillator*, Opt. Comm. **170**, 269 (1999).

[GO98a] D. Guéry-Odelin, J. Söding, P. Desbiolles, and J. Dalibard, *Is Bose-Einstein condensation of atomic cesium possible?*, Europhys. Lett. **44**, 26 (1998).

[GO98b] D. Guéry-Odelin, J. Söding, P. Desbiolles, and J. Dalibard, *Strong evaporative cooling of a trapped cesium gas*, Optics Express **2** (1998).

[Gre02] M. Greiner, O. Mandel, T. Esslinger, T. W. Hänsch, and I. Bloch, *Quantum phase transition from a superfluid to a Mott insulator in a gas of ultracold atoms*, Nature **415**, 39 (2002).

[Gri93] G. F. Gribakin and V. V. Flambaum, *Calculation of the scattering length in atomic collisions using the semiclassical approximation*, Phys. Rev. A **48**, 546 (1993).

[Gri00] R. Grimm, M. Weidemüller, and Y. Ovchinnikov, *Optical dipole traps for neutral atoms*, Adv. At. Mol. Opt. Phys. **42**, 95 (2000), arXiv:physics/9902072.

[Gro61] E. P. Gross, *Structure of a Quantized Vortex in Boson Systems*, Il Nuovo Cimento **20**, 454 (1961).

[Gry93] G. Grynberg, B. Lounis, P. Verkerk, J. Courtois, and C. Salomon, *Quantized motion of cold cesium atoms in two- and three-dimensional optical potentials*, Phys. Rev. Lett. **70**, 2249 (1993).

[Gup02] S. Gupta, K. Dieckmann, Z. Hadzibabic, and D. E. Pritchard, *Contrast Interferometry using Bose-Einstein Condensates to Measure h/m and alpha*, Phys. Rev. Lett. **89**, 140401 (2002).

[Hak00] H. Haken and H. C. Wolf, *Atom- und Quantenphysik*, Springer-Verlag, Berlin, Heidelberg, New York, 2000, 7th ed.

[Ham02a] M. Hammes, *Optical Surface Microtraps based on Evanescent Waves*, Ph.D. thesis, Universität Innsbruck (2002).

[Ham02b] M. Hammes, D. Rychtarik, H.-C. Nägerl, and R. Grimm, *Cold-atom gas at very high densities in an optical surface microtrap*, Phys. Rev. A **66**, 051401(R) (2002), doi:10.1103/PhysRevA.66.051401.

[Han00] D.-J. Han, S. Wolf, S. Oliver, C. McCormick, M. T. DePue, and D. S. Weiss, *3D Raman Sideband Cooling of Cesium Atoms at High Density*, Phys. Rev. Lett. **85**, 724 (2000).

[Han01] D. J. Han, M. T. DePue, and D. Weiss, *Loading and compressing Cs atoms in a very far-off-resonant light trap*, Phys. Rev. A **63**, 023405 (2001).

[Hec59] C. E. Hecht, *The Possible Superfluid Behaviour of Hydrogen Atom Gases and Liquids*, Physica **25**, 1159 (1959).

[Her03] J. Herbig, T. Kraemer, M. Mark, T. Weber, C. Chin, H.-C. Nägerl, and R. Grimm, *Preparation of a Pure Molecular Quantum Gas*, Science **301**, 1510 (2003), published online 21 Aug 2003 (doi:10.1126/science.1088876).

[Hop00] S. A. Hopkins, S. Webster, J. Arlt, P. Bance, S. Cornish, O. Maragò, and C. J. Foot, *Measurement of elastic cross section for cold cesium collisions*, Phys. Rev. A **61**, 032707 (2000).

[Ino98] S. Inouye, M. R. Andrews, J. Stenger, H.-J. Miesner, D. M. Stamper-Kurn, and W. Ketterle, *Observation of Feshbach resonances in a Bose-Einstein condensate*, Nature **392**, 151 (1998).

[Jak98] D. Jaksch, C. Bruder, J. I. Cirac, C. W. Gardiner, and P. Zoller, *Cold Bosonic Atoms in Optical Lattices*, Phys. Rev. Lett. **81**, 3108 (1998).

[Jak02] D. Jaksch, V. Venturi, J. I. Cirac, C. J. Williams, and P. Zoller, *Creation of a Molecular Condensate by Dynamically Melting a Mott Insulator*, Phys. Rev. Lett. **89**, 040402 (2002).

[Jul03] P. S. Julienne, E. Tiesinga, and C. J. Williams (2003), calculations using the model of [Leo00]. Private communication.

[Kas95] A. Kastberg, W. D. Phillips, S. L. Rolston, R. J. C. Spreeuw, and P. S. Jessen, *Adiabatic Cooling of Cesium to 700 nK in an Optical Lattice*, Phys. Rev. Lett. **74**, 1542 (1995).

[Ker00] A. J. Kerman, V. Vuletić, C. Chin, and S. Chu, *Beyond Optical Molasses: 3D Raman Sideband Cooling of Atomic Cesium to High Phase-Space Density*, Phys. Rev. Lett. **84**, 439 (2000).

[Ker01] A. J. Kerman, C. Chin, V. Vuletić, S. Chu, P. J. Leo, C. J. Williams, and P. S. Julienne, *Determination of Cs-Cs interaction parameters using Feshbach spectroscopy*, C. R. Acad. Sci. Paris IV **2**, 633 (2001).

[Ket96] W. Ketterle and N. J. van Druten, *Evaporative Cooling of Trapped Atoms*, Adv. At. Mol. Opt. Phys. **37**, 181 (1996).

[Ket99] W. Ketterle, D. S. Durfee, and D. M. Stamper-Kurn, *Making, probing and understanding Bose-Einstein condensates*, in: M. Inguscio, S. Stringari, and C. E. Wieman (Eds.), *Proceedings of the International School of Physics - Enrico Fermi*, 67, IOS Press, 1999, arXiv:cond-mat/9904034.

[Kok98] S. J. J. M. F. Kokkelmans, B. J. Verhaar, and K. Gibble, *Prospects for Bose-Einstein Condensation in Cesium*, Phys. Rev. Lett. **81**, 951 (1998).

[Lan77] L. D. Landau and E. M. Lifshitz, *Quantum Mechanics: Non-Relativistic Theory*, Pergamon Press, Oxford, 1977, 3rd ed.

[Leo98] P. J. Leo, E. Tiesinga, P. S. Julienne, D. K. Walter, S. Kadlecek, and T. G. Walker, *Elastic and Inelastic Collisions of Cold Spin-Polarized* ^{133}*Cs Atoms*, Phys. Rev. Lett. **81**, 1389 (1998).

[Leo00] P. J. Leo, C. J. Williams, and P. S. Julienne, *Collision Properties of Ultracold* ^{133}*Cs Atoms*, Phys. Rev. Lett. **85**, 2721 (2000).

[Lid97] D. R. Lide (Ed.), *Handbook of Chemistry and Physics*, CRC Press, 1997, 78th ed.

[Los03] Los Alamos National Laboratory, Chemistry Division, *Periodic Table of the Elements*, `http://pearl1.lanl.gov/periodic/elements/55.html` (2003).

[Ma03] Z.-Y. Ma, A. M. Thomas, C. J. Foot, and S. L. Cornish, *The evaporative cooling of a gas of caesium atoms in the hydrodynamic regime*, J. Phys. B: At. Mol. Opt. Phys. **36**, 3533 (2003).

[Man88] F. Mandl, *Statistical Physics*, Wiley, 1988, 2nd ed.

[Man99] I. Manek, *Gravito-optical Surface Trap for Cesium Atoms*, Ph.D. thesis, Ruprecht-Karls-Universität Heidelberg (1999).

[Mar02] A. Marte, T. Volz, J. Schuster, S. Dürr, G. Rempe, E. G. M. van Kempen, and B. J. Verhaar, *Feshbach Resonances in Rubidium 87: Precision Measurements and Analysis*, Phys. Rev. Lett. **89**, 283202 (2002).

[Mar03a] H. Marion, F. P. D. Santos, M. Abgrall, S. Zhang, Y. Sortais, S. Bize, I. Maksimovic, D. Calonico, J. Grünert, C. Mandache, P. Lemonde, G. Santarelli, P. Laurent, A. Clairon, and C. Salomon, *Search for Variations of Fundamental Constants using Atomic Fountain Clocks*, Phys. Rev. Lett. **90**, 150801 (2003).

[Mar03b] M. Mark, *Bose-Einstein-Kondensation von Cäsium*, Diploma thesis, Universität Innsbruck (2003).

[Met99] H. J. Metcalf and P. van der Straten, *Laser cooling and trapping*, Springer-Verlag, New York, 1999.

[Mie96] F. H. Mies, C. J. Williams, P. S. Julienne, and M. Krauss, *Estimating Bounds on Collisional Relaxation Rates of Spin-Polarized ^{87}Rb Atoms at Ultracold Temperatures*, J. Res. Natl. Inst. Stand. Tech. **101**, 521 (1996).

[Mil93] J. D. Miller, R. A. Cline, and D. J. Heinzen, *Far-off-resonance optical trapping of atoms*, Phys. Rev. A **47**, R4567 (1993).

[Mod01] G. Modugno, G. Ferrari, G. Roati, R. J. Brecha, A. Simoni, and M. Inguscio, *Bose-Einstein Condensation of Potassium Atoms by Sympathetic Cooling*, Science **294**, 1320 (2001).

[Mon93] C. R. Monroe, E. A. Cornell, C. A. Sackett, C. J. Myatt, and C. E. Wieman, *Measurement of Cs-Cs Elastic Scattering at* $T = 30\mu K$, Phys. Rev. Lett. **70**, 414 (1993).

[Mos99] U. Moslener, *Weiterentwicklung der gravitooptischen Oberflächenfalle (GOST)*, Diploma thesis, Universität Heidelberg and Max-Planck-Institut für Kernphysik (1999).

[Nie99] E. Nielsen and J. H. Macek, *Low-energy recombination of identical bosons by three-body collisions*, Phys. Rev. Lett. **83**, 1566 (1999).

[O'H89] J. F. O'Hanlon, *A User's Guide to Vacuum Technology*, Wiley, 1989, 2nd ed.

[O'H99] K. M. O'Hara, S. R. Granade, M. E. Gehm, T. A. Savard, S. Bali, C. Freed, and J. E. Thomas, *Ultrastable* CO_2 *Laser Trapping of Lithium Fermions*, Phys. Rev. Lett. **82**, 4204 (1999).

[Per98] H. Perrin, A. Kuhn, I. Bouchoule, and C. Salomon, *Sideband cooling of neutral atoms in a far-detuned optical lattice*, Europhys. Lett. **42**, 395 (1998).

[Pet02] C. J. Pethick and H. Smith, *Bose-Einstein Condensation in Dilute Gases*, Cambridge University Press, 2002.

[Phi82] W. Phillips and H. Metcalf, *Laser Decelaration of an Atomic Beam*, Phys. Rev. Lett. **48**, 596 (1982).

[Pin97] P. W. H. Pinkse, A. Mosk, M. Weidemüller, M. W. Reynolds, T. W. Hijmans, and J. T. M. Walraven, *Adiabatically Changing the Phase-Space Density of a Trapped Bose Gas*, Phys. Rev. Lett. **78**, 990 (1997).

[Pit61] L. P. Pitaevskii, *Vortex lines in an imperfect Bose gas*, Sov. Phys. JETP **13**, 451 (1961).

[Pro85] J. Prodan, A. Migdall, W. Phillips, H. Metcalf, and J. Dalibard, *Stopping Atoms with Laser Light*, Phys. Rev. Lett. **54**, 992 (1985).

[Raa87] E. L. Raab, M. Prentiss, A. Cable, S. Chu, and D. E. Pritchard, *Trapping of Neutral Sodium Atoms with Radiation Pressure*, Phys. Rev. Lett. **59**, 2631 (1987).

[Raj79] R. K. Raj, D. Bloch, J. J. Sydner, G. Camy, and M. Ducloy, *High-Frequency Optically Heterodyned Saturation Spectroscopy Via Resonant Degenerate Four-Wave Mixing*, Phys. Rev. Lett. **32**, 145 (1979).

[Rob00] J. L. Roberts, N. R. Claussen, S. L. Cornish, and C. E. Wieman, *Magnetic Field Dependence of Ultracold Inelastic Collisions near a Feshbach Resonance*, Phys. Rev. Lett. **85**, 728 (2000).

[Rob01] A. Robert, O. Sirjean, A. Browaeys, J. Poupard, S. Nowak, D. Boiron, C. I. Westbrook, and A. Aspect, *A Bose-Einstein Condensate of Metastable Atoms*, Science **292**, 461 (2001).

[Rup95] P. A. Ruprecht, M. J. Holland, K. Burnett, and M. Edwards, *Time-dependent solution of the nonlinear Schrödinger equation for Bose-condensed trapped neutral atoms*, Phys. Rev. A **51**, 4704 (1995).

[Ryc03] D. Rychtarik, B. Engeser, H.-C. Nägerl, and R. Grimm, *Two-dimensional Bose-Einstein condensate in an optical surface trap*, arXiv:cond-mat/0309536 (2003), submitted for publication.

[Sak94] J. J. Sakurai, *Modern Quantum Mechanics*, Addison-Wesley, 1994, revised ed.

[Sav97] T. A. Savard, K. M. O'Hara, and J. E. Thomas, *Laser-noise-induced heating in far-off resonance optical traps*, Phys. Rev. A **56**, R1095 (1997).

[Sch99] U. Schünemann, H. Engler, R. Grimm, M. Weidemüller, and M. Zielonkowski, *Simple scheme for tunable frequency offset locking of two lasers*, Rev. Sci. Instrum. **70**, 242 (1999), doi:10.1063/1.1149573.

[Sie86] A. E. Siegmann, *Lasers*, University Science Books, Mill Valley, 1986.

[SK98a] D. M. Stamper-Kurn, M. R. Andrews, A. P. Chikkatur, S. Inouye, H.-J. Miesner, J. Stenger, and W. Ketterle, *Optical Confinement of a Bose-Einstein Condensate*, Phys. Rev. Lett. **80**, 2027 (1998).

[SK98b] D. M. Stamper-Kurn, H.-J. Miesner, A. P. Chikkatur, S. Inouye, J. Stenger, and W. Ketterle, *Reversible Formation of a Bose-Einstein Condensate*, Phys. Rev. Lett. **81**, 2194 (1998).

[Sna98] M. J. Snadden, J. M. McGuirk, P. Bouyer, K. G. Haritos, and M. A. Kasevich, *Measurement of the Earth's Gravity Gradient with an Atom Interferometer-Based Gravity Gradiometer*, Phys. Rev. Lett. **81**, 971 (1998).

[Söd98] J. Söding, D. Guéry-Odelin, P. Desbiolles, G. Ferrari, and J. Dalibard, *Giant Spin Relaxation of an Ultracold Cesium Gas*, Phys. Rev. Lett. **80**, 1869 (1998).

[Söd99] J. Söding, D. Guéry-Odelin, P. Desbiolles, F. Chevy, H. Inamori, and J. Dalibard, *Three-body decay of a rubidium Bose-Einstein condensate*, Appl. Phys. B **69**, 257 (1999).

[Ste99] J. Stenger, S. Inouye, M. R. Andrews, H.-J. Miesner, D. M. Stamper-Kurn, and W. Ketterle, *Strongly Enhanced Inelastic Collisions in a Bose-Einstein Condensate near Feshbach Resonances*, Phys. Rev. Lett. **82**, 2422 (1999).

[Ste02] D. A. Steck, *Cesium D Line Data*, `http://steck.us/alkalidata` , revision 1.5 (2002).

[Tak95] T. Takekoshi, J. R. Yeh, and R. J. Knize, *Quasi-electrostatic trap for neutral atoms*, Opt. Commun. **114**, 421 (1995).

[Tak98] T. Takekoshi, B. M. Patterson, and R. J. Knize, *Observation of Optically Trapped Cold Cesium Molecules*, Phys. Rev. Lett. **81**, 5105 (1998).

[Tak03] Y. Takasu, K. Maki, K. Komori, T. Takano, K. Honda, M. Kumakura, T. Yabuzaki, and Y. Takahashi, *Spin-Singlet Bose-Einstein Condensation of Two-Electron Atoms*, Phys. Rev. Lett. **91**, 040404 (2003).

[Tha01] G. Thalhammer, *Frequenzstabilisierung von Diodenlasern bei 850, 854 und 866 nm mit Linienbreiten im Kilohertz-Bereich*, Diploma thesis, Universität Innsbruck (2001).

[Tho03] A. M. Thomas, S. Hopkins, S. L. Cornish, and C. J. Foot, *Strong evaporative cooling towards Bose-Einstein condensation of a magnetically trapped caesium gas*, J. Opt. B: Quantum Semiclass. Opt. **5**, S107 (2003).

[Tie92] E. Tiesinga, A. Moerdijk, B. J. Verhaar, and H. T. C. Stoof, *Conditions for Bose-Einstein condensation in magnetically trapped atomic cesium*, Phys. Rev. A **46**, R1167 (1992).

[Tie93] E. Tiesinga, B. J. Verhaar, and H. T. C. Stoof, *Threshold and resonance phenomena in ultracold ground-state collisions*, Phys. Rev. A **47**, 4114 (1993).

[Tre01] P. Treutlein, K. Y. Chung, and S. Chu, *High-brightness atom source for atomic fountains*, Phys. Rev. A **63**, 051401 (2001).

[Vul99] V. Vuletić, A. J. Kerman, C. Chin, and S. Chu, *Observation of Low-Field Feshbach Resonances in Collisions of Cesium Atoms*, Phys. Rev. Lett. **82**, 1406 (1999).

[Web00] T. Weber, *Langzeitspeicherung verschiedener atomarer Spezies in einer quasi-elektrostatischen Dipolfalle*, Diploma thesis, Ruprecht-Karls-Universität Heidelberg (2000).

[Web03a] T. Weber, J. Herbig, M. Mark, H.-C. Nägerl, and R. Grimm, *Bose-Einstein Condensation of Cesium*, Science **299**, 232 (2003), published online 5 Dec 2002 (doi:10.1126/science.1079699).

[Web03b] T. Weber, J. Herbig, M. Mark, H.-C. Nägerl, and R. Grimm, *Three-body recombination at large scattering lengths in an ultracold atomic gas*, Phys. Rev. Lett. **91**, 123201 (2003), doi:10.1103/PhysRevLett.91.123201.

[Web03c] T. Weber, J. Herbig, M. Mark, T. Kraemer, C. Chin, H.-C. Nägerl, and R. Grimm, *Experiments with a Bose-Einstein condensate of cesium atoms*, in: *Proceedings of the XVI. International Conference on Laser Spectroscopy (ICOLS 2003)*, World Scientific, 2003.

[Wei02] D. S. Weiss, private communication (2002).

[Wen00] M. Wenin, *Adiabatische Phasenraumdichteänderung in einem zeitabhängigen Potential*, Diploma thesis, Universität Innsbruck (2000).

[Win84] W. Wing, *On Neutral Particle Trapping in Quasielectrostatic Electromagnetic Fields*, Prog. Quant. Elect. **8**, 181 (1984).

[Win02] K. Winkler, *Aufbau einer magnetischen Transportapparatur für ultrakalte Atome*, Diploma thesis, Universität Innsbruck (2002).

[Woo97] C. S. Wood, S. C. Bennett, D. Cho, B. P. Masterson, J. L. Roberts, C. E. Tanner, and C. E. Wieman, *Measurement of Parity Nonconservation and an Anapole Moment in Cesium*, Science **275**, 1759 (1997).

Dankeschön

Rudi, für die hervorragende Betreuung. Er hat mir bei diesem neuen Projekt viel Vertrauen entgegengebracht und jede denkbare Unterstützung geleistet.

HCN, ohne dessen tatkräftige Mithilfe wir nie so schnell so weit gekommen wären, und trotz dessen tatkräftiger Mithilfe meine Snowboardkenntnisse immer noch mangelhaft sind.

Jens, der praktisch von Anfang an alle Höhen und Tiefen der Levitation mit mir zusammen erlitten hat und mit dem die langen Laborstunden erst erträglich waren. Mit ihm und seiner WG verbinde ich viele lustige Abende.

Michael, der in der spannendsten Zeit voll eingestiegen ist und der mit viel Einsatz und Neugier alle Klippen gemeistert hat. Er hat trotz allem Streß und der ach so deutschen Kollegen nie seinen Humor verloren.

Tobias, der Markus H. als Büronachbarn nicht ersetzen kann, aber ein würdiger Nachfolger ist – auch als Bergfex vom Dienst. Er wird zusammen mit Michael die Kunst der Levitation weiter pflegen.

Markus H. und David P., den Buben der ersten Stunde, mit deren GOST zusammen wir ins ferne Österreich gezogen sind, und die von Anfang an für ein unterhaltsames Umfeld gesorgt haben.

Den Kollegen Selim, Alexander, Matthias, Mattias, Markus B., Gregor, Cheng, Michael H., Klaus, George, Bastian, Johannes, Gerhard, für eine fantastische Arbeitsatmosphäre, zahlreiche sinnarme Mittagsdiskussionen und etliche nette Abende.

Den Blatt'schen Buben und Mädels, ohne die weder bei der Arbeit noch privat der Einstieg ins schöne Tirol so angenehm gewesen wäre.

Toni, der sich bei unserer Vakuumkammer selbst übertroffen hat.

Andreas, Manuel und Stefan für technische Unterstützung aller Art.

Christine, Frau Köhle und Frau Moser für die Logistik, ohne die gar nix läuft.

Den Ex-Heidelbergern, die zu treffen jede Reise wert ist.

Meiner Familie im Saarland, durch die es für mich so etwas wie eine Heimat gibt.

Meinen Geschwistern Eva und Florian, auf die ich sehr stolz bin.

Meinen Eltern, die immer für mich da waren.

Julia, die mich glücklich macht.